

**Investigations on terahertz imaging based on coherent  
Fourier-space spectrum detection**

Dissertation

Zur Erlangung des Doktorgrades  
der Naturwissenschaften

vorgelegt beim Fachbereich Physik  
der Johann Wolfgang Goethe -Universität  
in Frankfurt am Main

von

Hui Yuan

geboren in Tieling, Liaoning, China

Frankfurt 2023

(D 30)

vom Fachbereich 13 der

Johann Wolfgang Goethe - Universität als Dissertation angenommen.

Dekan : Prof. Dr. Harald Appelshäuser

Gutachter : Prof. Dr. Hartmut Roskos, Prof. Dr. Gintaras Valušis und Prof. Dr.  
Xicheng Zhang

Datum der Disputation : vsl. 08. September 2022

*Für meine Eltern*

---

## **Acknowledgements**

Hui Yuan was supported by the China Scholarship Council (File No.:201606030113) and DFG project RO 770/48-1.

# Summary

Terahertz (THz) radiation lies between the micro and far-infrared range in the electromagnetic spectrum. Compared with microwave and millimeter waves, it has a larger signal bandwidth and extremely narrow antenna beam. Thus, it is easier to achieve high-resolution for imaging and detection applications. The unique properties, such as penetration for majority non-polar materials, non-ionizing characteristic and the spectral fingerprint of materials, makes THz imaging an appealing artifice in the military, biomedical, astronomical communications, and other areas. However, THz radiation's current low power level and detection sensitivity block THz imaging system from including fewer optical elements than the visible or infrared range. This leads to imaging resolution, contrast, and imaging field of view degenerate and makes the aberration more serious. THz imaging based on the space Fourier spectrum detection is developed in this thesis to achieve high-quality imaging. The main concept of Fourier imaging is by recording the field distribution in the Fourier plane (focal plane) of the imaging system; the information of the target is obtained. The numerical processing method is needed to extract the amplitude and phase information of the imaged target. With additional process, three-dimensional (3D) information can be obtained based on the phase information. The novel recording and reconstructing ways of the Fourier imaging system enables it to have a higher resolution, better contrast, and broader field of view than conventional imaging systems such as microscopy and plane to plane telescopic imaging system.

The work presented in this thesis consists of two imaging systems, one is working at 300 GHz based on the fundamental heterodyne detection of the THz radiation, the other is operated at 600 GHz by utilizing the sub-harmonic heterodyne detection technique. The realization and test of the heterodyne detection are based on the THz antenna-coupled field-effect transistor (**TeraFET**) detector developed by Dr. Alvydas Lisauskas. Both systems use two synchronized electronic multiplier chains to radiate the THz waves. One radiation works as the local oscillator (LO), the other works as illumination with a slight frequency shift, the radiations are mixed on the detector scanning in the Fourier plane to record the complex Fourier spectrum of the imaged target. The LO has the same frequency range as the illuminating radiation for fundamental heterodyne detection

---

but half the frequency range for the sub-harmonic heterodyne detection. The 2-mm resolution, 60-dB contrast, and 5.5-cm diameter imaging area at 300 GHz and the of 500- $\mu\text{m}$  resolution, 40-dB contrast, and 3.5-cm diameter imaging area at 600 GHz are achieved (the 300-GHz illuminating radiation has the approximate power of 600  $\mu\text{W}$ , the 600-GHz illuminating radiation has the approximate power of 60  $\mu\text{W}$ ).

The thesis consists of 6 parts. After the introduction, the second chapter expands on the topic of Fourier optics from a theoretical point of view and the simulations of the Fourier imaging system. First, the theory of the electromagnetic field propagation in free space and through an optical system are investigated to elicit the Fourier transform function of the imaging system. The simulation is used for theoretical considerations and the implementation of a Fourier optic script that allows for numerical investigations on reconstruction. The preliminary imaging field of view and resolution are also demonstrated. The third chapter describes the Fourier imaging system at 300 GHz based on the fundamental heterodyne detection, including the experimental setup, the 2D, and 3D imaging results. The following fourth chapter reports the integration of the TeraFET detector with two substrate lenses (one is a Si lens on the back-side Si substrate, the other is a wax/PTFE lens on the front side containing the bonding wires) for sub-harmonic heterodyne detection at 600 GHz. The characteristic of the wax/PTFE lens at THz range is presented. After that, the compared imaging results between the detector with and without the wax/PTFE lens are shown. The fifth chapter extends the demonstration on the lateral and depth resolution of the Fourier imaging system in detail and uses the experimental results at 600 GHz to validate the analytical predictions. The comparison of the resolution between the Fourier imaging system and the conventional microscopy system proves that the Fourier imaging system has better imaging quality under the same system configuration. The last chapter in this thesis concludes on the findings of the THz Fourier imaging and gives an outlook for the enhancement of the Fourier imaging system at THz range.

# Zusammenfassung

Das elektromagnetische Spektrum ist der Frequenzbereich der elektromagnetischen Strahlung, die jeweiligen Wellenlängen und Photonenenergien. Es umfasst den Frequenzbereich von unter 1 Hz bis über  $10^{25}$  Hz, was Wellenlängen von Tausenden von Kilometern bis zu einem Bruchteil der Größe eines Atomkerns entspricht. Man unterteilt das Spektrum in verschiedene Bänder, die als Radiowellen, Mikrowellen, Infrarotstrahlen, sichtbares Licht, Ultraviolett-, Röntgen- und Gammastrahlen bekannt sind, und zwar vom niederfrequenten (langwelligen) Ende bis zum hochfrequenten (kurzwelligen) Ende. Jedes Band hat seine einzigartigen Eigenschaften, z.B. wie es erzeugt wird, wie es mit Materie wechselwirkt und seine praktischen Anwendungen. Das sichtbare Spektrum war wohl der erste Frequenzbereich, der in der Geschichte der Erforschung des elektromagnetischen Spektrums untersucht wurde, da es mit dem bloßen Auge des Menschen direkt beobachtet werden kann. Mit der Entwicklung der Technologie wurde die Strahlung jenseits des sichtbaren Spektrums kontinuierlich erforscht und für verschiedene Anwendungen genutzt. So ist z.B. die Röntgenbildgebung für medizinische und Sicherheitszwecke von großer Bedeutung, infrarotbasierte Nachtsichtkameras sind für die polizeiliche Überwachung, das Militär und die Naturwissenschaften kommerziell erhältlich, auch Strahlung im Radar-Frequenzband wird mit moderner Technologie für Wetterbeobachtung, Topographieuntersuchungen oder militärische Nutzung abgebildet.

Terahertz (THz)-Strahlung liegt im elektromagnetischen Spektrum zwischen dem Mikro- und Ferninfrarotbereich. Die Strahlung bei THz-Frequenzen wurde viele Jahre lang als "THz-Lücke" behandelt, weil die Erkennung schwierig war. Da jedoch die Detektionstechnik in den letzten Jahren mit immer höherer Empfindlichkeit bei verschiedenen Frequenzen entwickelt wurde, wurde die THz-Strahlung der Beobachtung durch den Menschen und verschiedenen Anwendungen näher gebracht. Die THz-Strahlung befindet sich zwischen dem elektronischen und optischen Frequenzbereich und hat Eigenschaften aus beiden Frequenzbereichen: Aus dem ersten, dass man die Kohärenz der Strahlung leicht kontrollieren und ausnutzen kann und dass viele Materialien (halb-)transparent sind, aus dem zweiten, dass quasi-optische Strahlpropagationstechniken eingesetzt werden können. Außerdem hat es eine größere Signalbandbreite und einen extrem schmalen Antennenstrahl im Ver-

---

gleich zu Mikrowellen und Millimeterwellen. Dadurch ist es einfacher, eine hochauflösende Bildgebung zu erreichen. Die einzigartigen Eigenschaften, wie z.B. durchdringende und nicht-ionisierende Eigenschaften, machen die THz-Bildgebung zu einer attraktiven Anwendung in der militärischen, biomedizinischen, astronomischen Kommunikation und anderen Bereichen. Die derzeit geringe Leistung und Nachweisempfindlichkeit der THz-Strahlung schränkt das THz-Bildgebungssystem jedoch so ein, dass es viel weniger optische Elemente enthält als der sichtbare oder infrarote Bereich. Dies führt zu einer Degeneration der Bildauflösung, des Kontrasts und des Sichtfelds und macht die Aberration noch gravierender. Die THz-Bildgebung auf der Grundlage der Raum-Fourier-Spektrum-Detektion wird in dieser Arbeit entwickelt, um dieses Problem zu lösen und eine qualitativ hochwertige Bildgebung zu erreichen. Das Hauptkonzept der Fourier-Abbildung besteht in der Aufzeichnung der Feldverteilung in der Fourier-Ebene (Brennebene) des Abbildungssystems; die Information des Zielobjekts wird gewonnen. Die numerische Verarbeitungsmethode wird benötigt, um die Amplituden- und Phaseninformation des abgebildeten Ziels zu extrahieren. Nach dem weiteren Prozess kann auf der Basis der Phaseninformation dreidimensionale Information gewonnen werden. Die neuartige Aufnahme- und Rekonstruktionsmethode des Fourier-Abbildungssystems ermöglicht eine höhere Auflösung, einen besseren Kontrast und ein breiteres Sichtfeld als herkömmliche Abbildungssysteme wie Mikroskopie und Teleskope.

Diese Arbeit demonstriert das Konzept, die Simulation, die Durchführung und die Auflösung der Fourier-Bildgebung bei Sub-THz-Frequenzen. Die Simulationen, die auf dem Wellenausbreitungsintegral basieren, werden durchgeführt, um ein elektrisches Feld, das ein Eingangsobjekt beleuchtet, und seine Ausbreitung zur Fokusebene zu untersuchen. Numerische Studien helfen auch bei der Vorhersage von Eigenschaften, Merkmalen und potenziellen Ergebnissen einer experimentellen Messung. Simulationen geben eine Vorstellung davon, welche Objekte welche charakteristischen Intensitäts- und Phasenmuster erzeugen. Numerische Berechnungen helfen auch bei der Vorhersage der Auswirkungen von verrauschten Intensitäts- und Phasenmustern auf die Rückberechnung. Verschiedene Objekte führen zu unterschiedlichen Fourier-Spektren mit den hervorgehobenen Raumfrequenzen aus den Merkmalen des Objekts. Nach der Einführung wird im zweiten Kapitel das Thema Fourier-Optik aus theoretischer Sicht und die Simulationen des Fourier-Abbildungssystems vertieft. Zunächst wird die Theorie der Ausbreitung des elektromagnetischen Feldes im freien Raum und durch ein optisches System untersucht, um die Fourier-Transformationsfunktion des abbildenden Systems zu erhalten. Die Simulation wird für theoretische Überlegungen und die Implementierung eines optischen Fourier-Skripts verwendet, das numerische Untersuchungen zur Rekonstruktion ermöglicht. Das

---

vorläufige Abbildungssichtfeld und die Auflösung werden ebenfalls demonstriert. Im dritten Kapitel wird das Fourier-Abbildungssystem bei 300 GHz beschrieben, einschließlich des experimentellen Aufbaus, der auf der fundamentalen Heterodyn-Detektion, den 2D- und 3D-Abbildungsergebnissen basiert. Das folgende vierte Kapitel berichtet über die Integration des TeraFET-Detektors mit zwei Substratlinsen (eine ist eine Si-Linse auf dem rückseitigen Si-Substrat, die andere ist die Paraffin-Wachs-Linse auf der Vorderseite, die die Bonddrähte enthält) für die subharmonische Heterodyn-Detektion bei 600 GHz. Die Charakteristik der Paraffin-Wachs-Linse im THz-Bereich wird vorgestellt. Danach werden die verglichenen Bildergebnisse zwischen dem Detektor mit und ohne Paraffin-Wachs-Linse gezeigt. Das fünfte Kapitel erweitert die Demonstration zur lateralen und Tiefenauflösung des Fourier-Abbildungssystems im Detail und verwendet die experimentellen Ergebnisse bei 600 GHz zur Validierung der analytischen Vorhersagen. Der Vergleich der Auflösung zwischen dem Fourier-Abbildungssystem und dem konventionellen Mikroskopiesystem beweist, dass das Fourier-Abbildungssystem bei gleicher Systemkonfiguration eine bessere Abbildungsqualität aufweist. Das letzte Kapitel dieser Arbeit schließt mit den Ergebnissen der THz-Fourier-Bildgebung und gibt einen Ausblick auf die Verbesserung des Fourier-Bildgebungssystems im THz-Bereich.

Die in dieser Arbeit vorgestellte Fourier-Bildgebung besteht aus zwei bildgebenden Systemen, von denen eines bei 300 GHz arbeitet, basierend auf der fundamentalen heterodyn Detektion der THz-Strahlung, das andere wird bei 600 GHz betrieben, indem die subharmonische Detektionstechnik verwendet wird. Die Realisierung und der Test des Heterodyn-Nachweises basieren auf dem von Dr. Alvydas Lisauskas entwickelten THz-Antennen-gekoppelten Feldeffekttransistor-Detektor (TeraFET). TeraFETs sind als empfindliche Detektoren bekannt und werden meist mit modulierten (mechanischen oder elektronischen) Dauerstrichquellen und einem Lock-in-Verstärker verwendet. Daher ist die Verwendung von TeraFETs zur Echtzeitmessung von Einzelpulsen und zur heterodyn Detektion weitgehend unerforscht. Hier verwenden beide Heterodyn-Systeme zwei synchronisierte elektronische Multiplikatorketten zur Abstrahlung der THz-Wellen. Eine Strahlung arbeitet als lokaler Oszillator, die andere als Beleuchtung mit einer leichten Frequenzverschiebung, die Strahlungen werden auf dem Detektor gemischt, der in der Fourier-Ebene abtastet, um die komplexe Fourier-Spektrumsverteilung zu erfassen. Der LO hat den gleichen Frequenzbereich wie die Beleuchtungsstrahlung für die fundamentale Heterodyn-Detektion, aber den halben Frequenzbereich für die subharmonische Heterodyn-Detektion. Die Heterodyn-Detektion ermöglicht die Messung der komplexen Amplitude (Intensität und Phase). Basierend auf der Phaseninformation kann die Rekonstruktion der 3D-Strukturen mit dem Fourier-Bildgebungssystem durchgeführt werden.

---

Experimentelle Ergebnisse zeigen, dass eine Auflösung von 2 mm, ein Kontrast von 60 dB und ein Abbildungsbereich von 5,5 cm Durchmesser bei 300 GHz und eine Auflösung von 500  $\mu\text{m}$ , ein Kontrast von 30 dB und ein Abbildungsbereich von 4 cm Durchmesser bei 300 GHz erreicht werden (die 300-GHz-Beleuchtungsstrahlung hat die ungefähre Leistung von 1 mW, die 600-GHz-Beleuchtungsstrahlung hat die ungefähre Leistung von 56  $\mu\text{W}$ ).

Im Gegensatz zum konventionellen Bildgebungssystem hat die Fourier-Bildgebung eine höhere Auflösung. Dies kann darauf zurückgeführt werden, dass das Fourier-Abbildungssystem die Fähigkeit besitzt, den Objektabstand zu verkürzen (je kürzer der Objektabstand ist, desto bessere Auflösung wird erreicht). Das konventionelle Abbildungssystem muss im realen Abbildungsregime arbeiten (der Objektabstand des Abbildungssystems ist größer als die Brennweite des Systems), während das Fourier-Abbildungssystem das Objekt in den virtuellen Abbildungsobjektbereich bringen kann (wobei der Objektabstand kleiner als die Brennweite des Systems ist). Die entsprechenden experimentellen Ergebnisse demonstrieren die Theorien. Darüber hinaus bietet das Fourier-Abbildungssystem eine neue Möglichkeit der 3D-Abbildung bei THz-Frequenzen mit einer guten Tiefenauflösung.

Die vorliegende Arbeit ist wie folgt strukturiert. Es gab viele Ansätze bei der Realisierung der THz-Bildgebung für verschiedene Anwendungen mit unterschiedlichen Quellen, Detektoren und Techniken mit Vor- und Nachteilen für jede Methode. Diese Arbeit stellt die Fourier-Abbildungsmethode im THz-Bereich vor. Die THz-Fourier-Abbildung wird durch die Verwendung fundamentaler und subharmonischer Heterodyn-Detektoren realisiert, um das Fourier-Spektrum aufzuzeichnen und das Bild durch numerische Berechnungen wieder aufzubauen. Die numerische Rekonstruktion ermöglicht es dem System, die Objektebene präzise zu fokussieren und die Tiefenauflösung durch Anwendung der Schärfeextraktion zu finden. Die laterale Auflösung ist derzeit durch den Scanbereich/Blende des Systems begrenzt. Um die Auflösung des abgebildeten Objekts zu erhöhen, müssen zukünftige Experimente die Reichweite im k-Raum erhöhen. Dies kann entweder durch eine Erhöhung des Verfahrwegs der Translationen, aufgrund der höheren Empfindlichkeit des Detektors oder durch eine Verringerung der Fokusslänge erreicht werden. Wie bereits erwähnt, ändern kohärente Reflexionen die Phase in der Fourierebene und haben daher einen hohen Einfluss auf die Qualität der Rekonstruktion, insbesondere bei zwei Substratlinsen auf beiden Seiten des Detektors. Um die kohärente Länge zu verkürzen, aber das Phasenverhalten des Fourier-Spektrums nicht zu zerstören, müssen schwach absorbierende optische Elemente eingesetzt werden. Dies wird zur Reduzierung stehender Wellen in nachfolgenden Experimenten beitragen. Um das Auflösungsvermögen der Messung in der Fourier-Ebene zu nutzen, muss das Sichtfeld im Fourier-Aufbau verbreit-

---

ert und der THz-Strahl gefiltert werden, so dass das Objekt mit einer homogenen statt einer gaußschen Intensitätsverteilung beleuchtet wird. Mit dem jetzigen Aufbau lässt sich nicht abschätzen, wie genau die Phasenkrümmung gemessen wurde und damit wie tiefenempfindlich die Messungen sind. Die zukünftigen Arbeiten können sich auf die Phasenrückgewinnung zur Eliminierung des Phasenrauschens konzentrieren, wodurch das System eine bessere laterale und Tiefenauflösung, einen schärferen Kontrast und einen größeren Dynamikbereich erreichen kann. Alles in allem realisierte diese Studie das hochauflösende, großflächige Sichtfeld und das 3D-Fourier-Bildgebungssystem. Darüber hinaus wurde das Potenzial der THz-Quellen und des TeraFET-Detektors für Anwendungen in der Bildgebung ausgeschöpft, so dass das System selbst potenziell für verschiedene Anwendungen der zerstörungsfreien Prüfung, der Qualitätsüberwachung und der 3D-Bildgebung im THz-Bereich eingesetzt werden kann.



# Contents

<b>Author's contributions</b>	<b>xvii</b>
<b>Author's planed publication in the pipeline</b>	<b>xxi</b>
<b>1 Introduction</b>	<b>1</b>
<b>2 Fourier imaging</b>	<b>5</b>
2.1 Optical Diffraction analysis in Fourier optics . . . . .	5
2.1.1 Hugens-Fresnel principle . . . . .	6
2.1.2 Kirchhoff diffraction integral formula . . . . .	8
2.1.3 Fresnel diffraction . . . . .	10
2.1.4 Fraunhofer diffraction . . . . .	11
2.1.5 Thin lens Fourier transform . . . . .	12
2.1.6 Fraunhofer diffraction in a finite distance . . . . .	14
2.1.7 Fourier transform in diffraction computing . . . . .	16
2.2 Principle of Fourier imaging . . . . .	17
2.2.1 Model of Fourier imaging . . . . .	17
2.2.2 Advantages of Fourier imaging . . . . .	20
2.3 Simulation of Terahertz Fourier imaging . . . . .	25
2.3.1 Simulation of THz Fourier imaging setup with simple samples . .	26
2.3.2 Field of View of Fourier imaging setup . . . . .	35
2.3.3 The primary analysis of Fourier imaging resolution . . . . .	38
2.4 Discussion and conclusions . . . . .	39
<b>3 Fourier imaging at 300 GHz</b>	<b>41</b>
3.1 Experimental setup of 300-GHz Fourier imaging system . . . . .	41
3.1.1 Principle of heterodyne detection . . . . .	41
3.1.2 300-GHz Fourier imaging setup based on heterodyne detection . .	42
3.1.3 Image reconstruction . . . . .	45

3.2	Imaging results of 300-GHz Fourier imaging system . . . . .	46
3.2.1	Imaging results of different sample . . . . .	46
3.2.2	Imaging results for different image distances . . . . .	48
3.2.3	Imaging results of obstacle objects . . . . .	52
3.3	Discussion and comparation . . . . .	52
<b>4</b>	<b>Fourier imaging based on sub-harmonic heterodyne detection at 600 GHz</b>	<b>55</b>
4.1	Fourier imaging based on sub-harmonic heterodyne detection . . . . .	55
4.1.1	Sub-harmonic heterodyne detection . . . . .	55
4.1.2	Characteristics of sub-harmonic detection at THz range . . . . .	58
4.1.3	Integration of sub-harmonic detection in THz Fourier imaging . . . . .	63
4.1.4	Characteristics of paraffin wax at THz band . . . . .	66
4.1.5	Processing of wax/PTFE lens on TeraFET detectors . . . . .	71
4.1.6	Characteristics of wax/PTFE lens on TeraFET detectors . . . . .	74
4.2	Dynamic range enhancement of wax/PTFE lens integration . . . . .	77
4.3	Resolution enhancement of wax/PTFE lens integration . . . . .	77
4.4	Fourier imaging results at 600 GHz . . . . .	79
<b>5</b>	<b>Resolution Comparison of Fourier imaging system and microscopy system</b>	<b>81</b>
5.1	Lateral resolution of Fourier imaging setup . . . . .	81
5.1.1	Lateral resolution of Fourier imaging setup in principle . . . . .	82
5.1.2	Lateral resolution of experimental results . . . . .	86
5.2	Depth resolution of Fourier imaging setup . . . . .	90
5.2.1	Depth resolution of Fourier imaging setup in principle . . . . .	90
5.2.2	Validation of depth resolution . . . . .	91
5.2.3	Depth resolution of experimental results . . . . .	92
5.3	Resolution of conventional microscopic imaging system . . . . .	95
5.4	Comparison of the resolution of Fourier imaging system and conventional microscopic imaging system . . . . .	98
5.4.1	Theoretical comparison . . . . .	98
5.4.2	Experimental results comparison . . . . .	99
5.5	Conclusion . . . . .	101
<b>6</b>	<b>Conclusion and Outlook</b>	<b>103</b>
6.1	Conclusion . . . . .	103

6.2 Outlook . . . . .	104
<b>Appendices</b>	<b>111</b>
<b>A Complementary Figures</b>	<b>113</b>
A.1 Fourier spectrum . . . . .	113
A.2 Power of 300 GHz and 600 GHz radiation . . . . .	118
<b>B Imaging resolution simulation</b>	<b>119</b>
B.1 Lateral resolution simulation . . . . .	119
B.2 Depth resolution simulation . . . . .	128
<b>Bibliography</b>	<b>131</b>



# Author's contributions

Parts of this work are published in three journals ([1] to [3]), under reviewed by two journals ([4] and [5]), presented at ten conferences ([6] to [15]) and accepted by one upcoming workshop ([16]):

- [1] H. Yuan, D. Voß, A. Lisauskas, D. Mundy, and H. G. Roskos, “3D Fourier imaging based on 2D heterodyne detection at THz frequencies,” *APL Photonics*, vol. 4, no. 10, p. 106 108, 2019. DOI: 10.1063/1.5116553.
- [2] M. Wan, H. Yuan, J. J. Healy, and J. T. Sheridan, “Terahertz confocal imaging: Polarization and sectioning characteristics,” *Optics and Lasers in Engineering*, vol. 134, p. 106 182, 2020, ISSN: 0143-8166. DOI: <https://doi.org/10.1016/j.optlaseng.2020.106182>.
- [3] G. Valušis, A. Lisauskas, H. Yuan, W. Knap, and H. G. Roskos, “Roadmap of terahertz imaging 2021,” *Sensors*, vol. 21, no. 12, 2021, ISSN: 1424-8220. DOI: 10.3390/s21124092. [Online]. Available: <https://www.mdpi.com/1424-8220/21/12/4092>.
- [4] H. Yuan, A. Lisauskas, M. Zhang, Q. ul-Islam, D. Erni, and H. G. Roskos, “A Wax/PTFE Substrate Lens Enables Effective Front-side Illumination of TeraFET Detectors,” *Opt. Lett.*, *under review*, 2022.
- [5] H. Yuan, A. Lisauskas, and H. G. Roskos, “600-GHz Fourier Imaging Based on the 2<sup>nd</sup> Sub-harmonic Heterodyne Detection of TeraFET Detectors,” *APL Photonics*, *under review*, 2022.

- [6] H. Yuan, M. Wan, A. Lisauskas, J. T. Sheridan, and H. G. Roskos, “300-GHz in-line holography with high dynamic range,” in *Holography: Advances and Modern Trends VI*, A. Fimia, M. Hrabovský, and J. T. Sheridan, Eds., International Society for Optics and Photonics, vol. 11030, SPIE, 2019, pp. 162–168. DOI: 10.1117/12.2520954.
- [7] H. Yuan, M. Wan, A. Lisauskas, J. T. Sheridan, and H. G. Roskos, “300-GHz holography with heterodyne detection,” in *Digital Holography and Three-Dimensional Imaging 2019*, Optical Society of America, 2019, Th3A.21. DOI: 10.1364/DH.2019.Th3A.21.
- [8] H. Yuan, D. Voß, M. Wan, A. Lisauskas, H. G. Roskos, and J. T. Sheridan, “Terahertz Imaging Based on Coherent Detection of the Fourier-Space Spectrum,” in *2019 44th International Conference on Infrared, Millimeter, and Terahertz Waves (IRMMW-THz)*, 2019, pp. 1–2. DOI: 10.1109/IRMMW-THz.2019.8873753.
- [9] H. Yuan, D. Voß, A. Lisauskas, F. Li, and H. G. Roskos, “Fourier imaging with CW terahertz waves,” in *Terahertz Emitters, Receivers, and Applications X*, M. Razeghi, A. N. Baranov, and M. S. Vitiello, Eds., International Society for Optics and Photonics, vol. 11124, SPIE, 2019, pp. 141–146. DOI: 10.1117/12.2528661.
- [10] H. Yuan, A. Lisauskas, M. Zhang, A. Rennings, D. Erni, and H. G. Roskos, “Dynamic-range Enhancement of Heterodyne THz Imaging by the Use of a Soft Paraffin-wax Substrate Lens on the Detector,” in *2019 Photonics Electromagnetics Research Symposium - Fall (PIERS - Fall)*, 2019, pp. 2607–2611. DOI: 10.1109/PIERS-Fall148861.2019.9021735.
- [11] M. Wan, H. Yuan, D. Čibiraitė, D. Cassidy, A. Lisauskas, J. J. Healy, H. G. Roskos, V. Krozer, and J. T. Sheridan, “Terahertz quantitative metrology using 300 GHz in-line digital holography,” in *Holography: Advances and Modern Trends VI*, A. Fimia, M. Hrabovský, and J. T. Sheridan, Eds., International

- 
- Society for Optics and Photonics, vol. 11030, SPIE, 2019, pp. 155–161. DOI: 10.1117/12.2520787.
- [12] M. Wan, H. Yuan, D. Čibiraitė, J. J. Healy, H. G. Roskos, and J. T. Sheridan, “Terahertz Spectrum Detection Based on Interferometry,” in *Digital Holography and Three-Dimensional Imaging 2019*, Optical Society of America, 2019, Th3A.40. DOI: 10.1364/DH.2019.Th3A.40.
- [13] M. Wan, D. Čibiraitė, B. Li, H. Yuan, V. Krozer, H. Roskos, D. Wang, and J. T. Sheridan, “Polarization and sectioning characteristic of THz confocal microscopy,” in *2019 44th International Conference on Infrared, Millimeter, and Terahertz Waves (IRMMW-THz)*, 2019, pp. 1–2. DOI: 10.1109/IRMMW-THz.2019.8874261.
- [14] H. Yuan, A. Lisauskas, M. Wan, J. T. Sheridan, and H. G. Roskos, “Resolution enhancement of THz imaging based on Fourier-space spectrum detection,” in *Terahertz, RF, Millimeter, and Submillimeter-Wave Technology and Applications XIII*, L. P. Sadwick and T. Yang, Eds., International Society for Optics and Photonics, vol. 11279, SPIE, 2020, pp. 159–166. DOI: 10.1117/12.2546541.
- [15] Q. Islam, F. Meng, H. Yuan, and H. G. Roskos, “THz emission from semiconductors using excitation by a tilted pulse front,” in *Terahertz, RF, Millimeter, and Submillimeter-Wave Technology and Applications XIII*, L. P. Sadwick and T. Yang, Eds., International Society for Optics and Photonics, vol. 11279, SPIE, 2020, pp. 122–127. DOI: 10.1117/12.2547307.
- [16] H. Yuan, A. Lisauskas, and H. G. Roskos, “Dual substrate lenses on terafet detector enable fourier imaging based on sub-harmonic detection at 600 ghz,” in *2021 46th International Conference on Infrared, Millimeter and Terahertz Waves (IRMMW-THz)*, 2021, pp. 1–2. DOI: 10.1109/IRMMW-THz50926.2021.9566984.
- [17] H. Yuan, A. Lisauskas, M. Zhang, Q. ul-Islam, D. Erni, and H. G. Roskos, “Fourier Imaging Based on Sub-harmonic Detection at 600 GHz,” in *2022*

*Fifth International Workshop on Mobile Terahertz Systems (IWMTS), accepted, 2022.*

# Author's planned publication in the pipeline

Related work are prepared for the papers in the pipeline:

- [1] First author: H. Yuan, "An optical isolator based on a metamaterial polarization filter for the suppression of back-reflections in THz measurement system," 2022.
- [2] First author: M.J. Xiang, co-author: H. Yuan, "Phase retrieval for THz Fourier imaging with physics-informed deep learning," 2022.
- [3] First author: H. Yuan, "Design and implementation of double-resonant sub-THz detectors for efficient sub-harmonic mixing," 2022.



# 1 Introduction

The electromagnetic spectrum is the continuum of electromagnetic radiation frequencies, their respective wavelengths and photon energies. It covers the range of frequency values which vary from about 1 Hz to above  $10^{25}$  Hz, corresponding to wavelengths from thousands of kilometers down to a fraction of the size of an atomic nucleus. According to the studies, the wavelength spectrum is divided into different bands, generally known as radio waves, microwaves, infrared, visible light, ultraviolet, X-rays, and gamma rays; from the low frequency (long wavelength) band to the high-frequency (short wavelength) band. Each band has its unique characteristics, such as the way it is produced, how it interacts with matter and its practical applications. Visible spectrum is the first frequency range being investigated in the electromagnetic spectrum research history as it can be directly observed by the naked eye of the human being. With the development of technology, the radiation beyond the visible spectrum has been continuously explored and further undertaken to be used in different applications. For example, X-ray imaging is of major importance for medical and security purposes - infrared based night vision cameras are commercially available for police surveillance, military and natural science; also, radiation in the radar frequency band is imaged with modern technology for weather screening, topography investigations or military use.

The spectrum range between the electronic and optical frequency regimes, occupies the frequency from 0.1 THz to 10 THz (wavelength from 30  $\mu\text{m}$  to 3 mm, temperature from 4.8 K to 487 K, photon energy from 0.4 meV to 41 meV), is called Terahertz (THz) radiation. For many years these frequencies were treated as the "THz-gap" because of the detection challenges. However, during recent years the development of detection techniques has reached a new level of sensitivity. Inheriting the characteristics of electronic

frequencies, the THz radiation is easy to be controlled, exploited the coherence and (semi-) transparency for many materials, from the optical feature aspect, the quasi-optical beam propagation techniques can be employed. All of these, thereby bring the THz radiation to the eyesight of the mankind and open the potential for various practical applications in areas of stand-off explosive detection [1], medical imaging [2], non-destructive real-time imaging [3], biological and auto vehicle applications [4, 5], etc.. Recently, THz waves is also under discussion as the main target frequency band for future communications (6G, 7G).

The two basic and crucial elements for the THz technology is the source and detector. The emerged THz generation techniques in last decades including Gyrotrons [6], free electron lasers (FELs) [7], backward wave oscillators (BWOs) [8], resonant tunnelling diodes (RTD) [9, 10], Gunn [11] or transferred electron devices (TED) [12–14], impact avalanche transit time (IMPATT) diodes, tunnel injection transit time (TUNNETT) diodes, frequency multiplier as the widely used electronic sources, Quantum cascade lasers, gas lasers and terahertz optoelectronic sources as the common THz photonic sources. Fig. 1.1 displays the output power range of the sources. BWOs can be electrically tuned over a bandwidth of more than 50% of their operational frequencies, and can generate up to 50 mW of power at 300 GHz going down to a few mW at 1 THz [15]. Gunn devices could generate 0.2-5  $\mu$ W power at 400-560 GHz frequency range. MMIC technology can generate high output power above 100 GHz [16]. TUNNETT diodes with operational frequency as high as 355 GHz with 140  $\mu$  W output power have been reported [17].

For detection technique, Golay cells, pyroelectric detectors, thermoelectric detectors or thermopiles, and bolometers are the most widely used thermal detectors, in addition, the merging semiconductor based transistors work well for heterodyne detecting configuration. The typical responsivity of Golay cells at 1 THz with 10 Hz modulation frequency is around  $10^5$  V/W with the NEP of around  $10^{-10}$  WHz<sup>-1/2</sup>, the NEP of pyroelectric detectors are  $5 \times 10^{-10}$  WHz<sup>-1/2</sup> at 1 MHz modulation frequency and  $\lambda = 10$   $\mu$ m wavelength range, room temperature bolometers with normal metal absorbers is in the NEP range of  $5 \times 10^{-10}$  WHz<sup>-1/2</sup> with responsivity of 100 V/W and 1 s response time, under liquid nitrogen cooled condition, the NEP can be as low as  $2.5 \times 10^{-12}$  WHz<sup>-1/2</sup> with

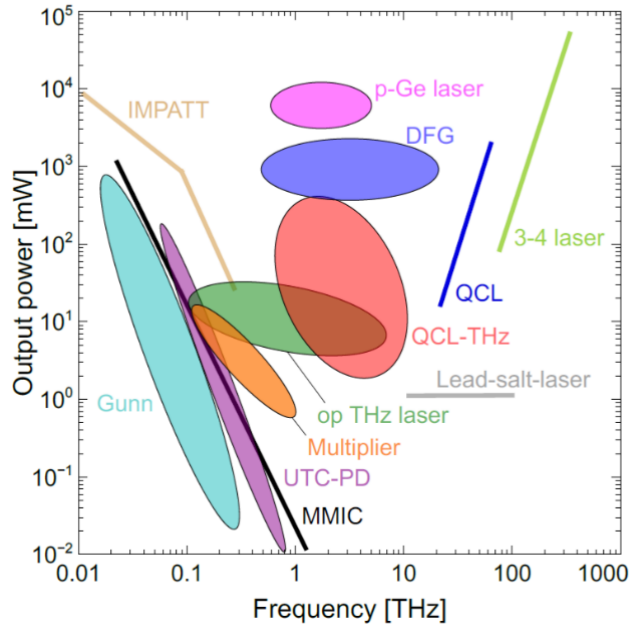


Figure 1.1: Typical output power of various THz sources as a function of frequency. MMIC stands for microwave monolithic integrated circuit, TUNNET stands for tunnel injection transit time, IMPATT stands for impact ionisation avalanche transit-time diode, DFG stands for difference frequency generation, Gunn stands for Gunn diodes, UTC-PD stands for uni-travelling-carrier photodiode, Multiplier for frequency multiplier, op THz laser stands for optical pumped THz laser and QCL for quantum cascade laser [18–20].

responsivity of 4000 V/W and 200 ns response time. The NEP of semiconductor detector is around  $40 \times 10^{-12} \text{ WHz}^{-1/2}$  at 300 GHz with room temperature.

This thesis will expand the demonstration on THz imaging technology which most widely adopted in various applications based on the developed THz radiating and detection techniques. Regarding detection modalities, the THz imaging can be divided into coherent and in-coherent approaches. The in-coherent modality with only amplitude detection is more direct and compact compared to the coherent imaging, and thus has been intensively investigated. Coherent imaging relies on interference [21], heterodyne measurements [22, 23] or time-resolved detection of THz pulses to record not only the intensity, but also the phase information. It is usually more demanding in its implementation, and has not been explored in THz range as extensively as in the optical range, because of severe power limitations and the lack of sensitive and fast detectors, especially

detector arrays for THz waves. At least with regard to detectors and arrays thereof, recent years have seen important advances in silicon CMOS technology, which benefit coherent imaging investigations [24–27]. The lack of the phase information limits conventional incoherent imaging to the recording of two-dimensional (2D) images. In order to achieve 3D information, more advanced techniques such as multidirectional imaging (tomography) or the application of light-field techniques [28] are required.

With considerable progress achieved in the field of THz radiation detection, 3D imaging with THz radiation has been developed with different techniques [29–32]. However, most of the conventional THz imaging methods are incompetent in covering a large field of view and recording large space three-dimensional images. This work is mainly aiming at investigating a large field, high-resolution, 3D imaging system working at THz frequencies. The Fourier imaging method, which is an indirect imaging technique, recording the complex Fourier-space spectrum of the object/scene by numerical calculation is adopted. The Fourier-space spectrum is recorded by heterodyne detection in the focal plane of the imaging system. In the focal plane, the energy area is the smallest of the system, giving the possibility of integrating the small-pixel-number detector in the THz regime in the system. Here the fundamental heterodyne detection (FHD) and the sub-harmonic heterodyne detection (SHHD) are demonstrated. Both approaches mix the output of two electronic multiplier chain THz radiations, the FHD mixes around the same frequencies radiations while the sub-harmonic mixes the detection frequency and the unit fraction of the frequency reference radiations. Furthermore, the Fourier THz imaging broadens the application area of known sources as well as detectors.

## 2 Fourier imaging

Fourier imaging is an indirect imaging technique which records the complex Fourier-space spectrum of the object/scene and reconstructs the image by numerical calculation [33–36]. As depicted in Fig. 2.1 (a), in the focal plane of the imaging system, the complex-valued electromagnetic field is the Fourier-space spectrum of the object illuminated by a collimated beam. Rather than direct observing the objects by intensity distribution in the image plane as conventional imaging methods, the complex Fourier-space spectrum is recorded, from which the observed scenery is derived by numerical inverse Fourier transform. Fig. 2.1 (b) shows the relationship of the Fourier-space spectrum and the imaged object by taking a picture as simulation example. The focal plane of the optical system therefore is named as Fourier plane. In Fourier plane, the beam cross section is smallest along the entire beam path, thus the detector array can have the smallest size which fits the THz detection situation. In the following chapter, the basics of optical diffraction is presented and formulas are derived to theoretically investigate Fourier optics. The implementation of the formulas is considered in more detail, before a closer look is taken on the role of the intensity and phase. The chapter finishes with further simulation results focusing on experimental boundary conditions.

### 2.1 Optical Diffraction analysis in Fourier optics

The phenomenon known as diffraction is a fundamental phenomenon in the propagation of light waves, plays a role of utmost importance in the branches of physics and engineering [37]. It is an inevitable result of the superposition of light waves. The principle of superposition is one of the basic principles of wave optics and the theoretical basis for solving

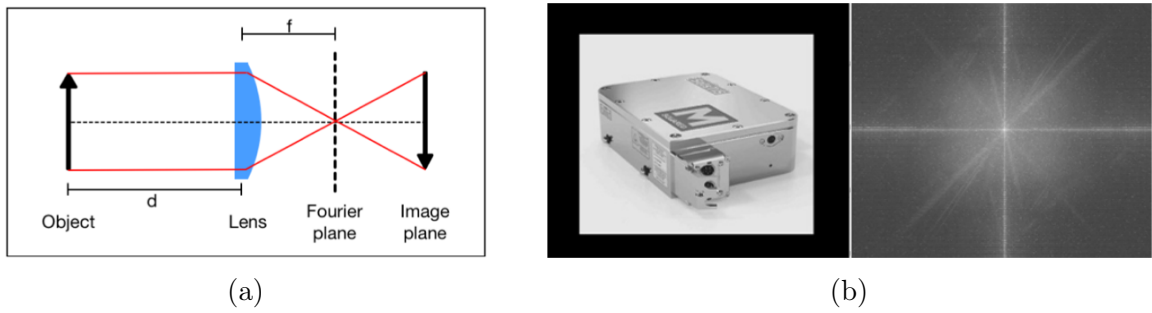


Figure 2.1: (a) Sketch of Fourier imaging and (b) simulation of the relationship between the recorded data (right panel) and the imaged target (left panel).

diffraction problems. The theoretical analysis of the superposition of the light waves can be deduced as the Fourier transform in mathematics. Fourier imaging is therefore generated based on this concept. In this chapter, some of the foundations of scalar diffraction theory analysis based on Fourier theorem in different situations will be developed. To fully understand the properties of optical imaging and data processing systems, it is essential that diffraction and the limitations it imposes on system performance be appreciated. A variety of references to more comprehensive treatments of diffraction theory will be found in the material that follows. After which the thin lens effect in Fourier optics is also demonstrated to serve for the later Fourier imaging analysis.

### 2.1.1 Hugens-Fresnel principle

In 1690, Huygens published the book "Treatise on Light", in which the hypothesis "Each surface element on the wave front can be regarded as a secondary disturbance center, which can generate spherical wavelets", and "in the latter moment, the position of the wave front is the envelope of all these wavelets. " were put forward [38, 39], Fig. 2.2 shows the spherical and plane wave propagations. However, this hypothesis is based on the assumption. Although the inevitability of the diffraction phenomenon can be explained, it is not possible to quantitatively calculate the law of light propagation in free space after the diffracting object. Therefore, the irradiance distribution of the diffraction pattern on the observation surface cannot be determined. Fresnel made an important supplementation to Huygens principle, and proposed Huygens-Fresnel principle. It is expressed as: "Any

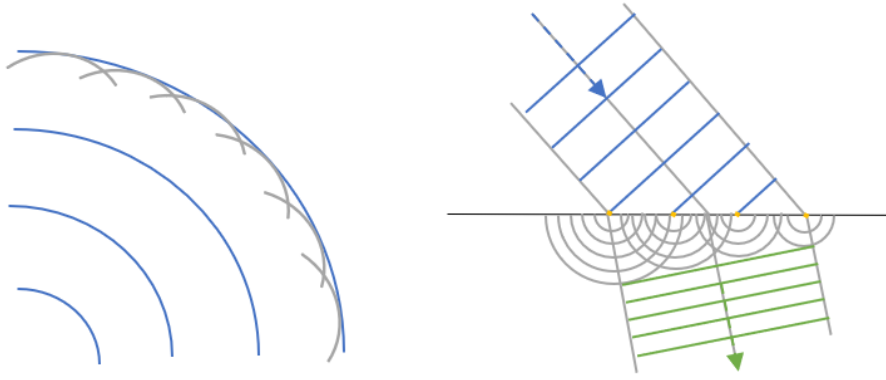


Figure 2.2: Huygens description of spherical and plane wave propagations.

surface element on the wave-front that is not blocked can be regarded as a wavelet source. The wave-front wavelet that emits the same frequency as the incident wave, and the optical vibration at any subsequent point is the result of the superposition of all the wavelets." Essentially, It is the product of the combination of Huygens' wavelet hypothesis and the principle of interference superposition. As shown in Fig. 2.3, S is a monochromatic point light source, the radiating intensity is  $A'$ , the complex field on the incident screen therefore is  $E_0 = A' e(jkr_0)/r_0$ . According to Huygens-Fresnel principle, the quantitative calculation of Eq. 2.1 can be used to describe the correlation of the field distribution between any two surfaces (such as the diffracting diaphragm surface  $\Sigma$  and the observation surface  $\Pi$ ) during the propagation.

$$E(P) = K E_0 \iint D(\chi) \frac{e^{jkr'}}{r'} d\xi d\eta, \quad (2.1)$$

where  $K$  is the complex coefficient, and  $E(P)$  is the complex field at point  $P$ .  $D(\chi)$  is the "direction factor", which represents the relationship between the strength of the wavelets in different directions. Fresnel had assumed that the value of  $D(\chi)$  was between 0 and 1,  $D(0) = 1$  and  $D(\pi/2) = 0$  to avoid the retrogressive waves. The formula is based on assumptions, and both the complex coefficient  $K$  and the direction factor  $D(\chi)$  in the formula are uncertain.



of  $\Sigma$ ,  $\Sigma_1$ , and a spherical surface  $\Sigma_2$  with P as the center and a radius R tending to infinity, i.e.  $S = \Sigma + \Sigma_1 + \Sigma_2$ , the integral of electric field at P can be expressed as

$$E(P) = \frac{1}{4\pi} \iint_{\Sigma + \Sigma_1 + \Sigma_2} \left[ \frac{\partial E}{\partial n} \frac{e^{jkr}}{r} - E \frac{\partial}{\partial n} \left( \frac{e^{jkr}}{r} \right) \right] d\xi d\eta. \quad (2.2)$$

In order to determine the electric fields  $E$  and  $\partial E/\partial n$ , Kirchhoff made the following assumptions: i) In area of  $\Sigma$ ,  $E$  and  $\partial E/\partial n$  are determined by the nature of the incident wave rather than affected by  $\Sigma_1$  at all. ii) On the right side of the  $\Sigma_1$ ,  $E$  and  $\partial E/\partial n$  are always equal to 0, and has no relationship with  $\Sigma$  at all. These two assumptions are named as Kirchhoff boundary conditions. Combining Sommerfeld radiation conditions, Eq. 2.2 can be simplified as

$$E(P) = \frac{1}{j\lambda} \iint_{\Sigma} A' \frac{e^{jkr_0}}{r_0} \frac{e^{jkr}}{r} \frac{\cos \alpha_1 + \cos \alpha_2}{2} d\xi d\eta, \quad (2.3)$$

where  $D(\alpha) = (\cos \alpha_1 + \cos \alpha_2)/2$  is the direction factor, and the definitions of the direction angles  $\alpha_1$  and  $\alpha_2$  are shown in Fig. 2.4. If the complex constant  $K = 1/j\lambda$  is set, the Fresnel diffraction integrals of equations 2.3 and 2.2 have exactly the same manifestation.

The Kirchhoff diffraction integral is based on a solid mathematical foundation. It gives a specific form and physical meaning of the parameters and corrects some Fresnel's assumptions about the properties of wavelets. However, obvious inconsistencies are still in the boundary conditions. Therefore, Sommerfeld modified the form of the Green's function  $G$  in this theory, simplified and generalized the Kirchhoff diffraction formula. It can be shown as Fig. 2.5. In Cartesian coordinates, the plane  $\Sigma$  ( $\xi, \eta$ ) where diffraction aperture exists is  $d$  distance away from the observation plane  $\Pi$  ( $x, y$ ).  $\Sigma$  and  $\Pi$  are parallel to each other. The field distribution propagated to  $\Sigma$  plane is  $B(\xi, \eta)$ . With a transmission coefficient  $T(\xi, \eta)$  of a diffracting object, the transmitted wave can be expressed as  $A(\xi, \eta) = B(\xi, \eta)T(\xi, \eta)$ . Taking it into formula 2.3 and substituting

$D(\alpha) = 1$  under paraxial approximation, the diffraction pattern will be

$$E(x, y) = \frac{1}{j\lambda} \iint A(\xi, \eta) \frac{e^{jkr}}{r} d\xi d\eta. \quad (2.4)$$

This formula expresses the diffraction theory more concisely and clearly.

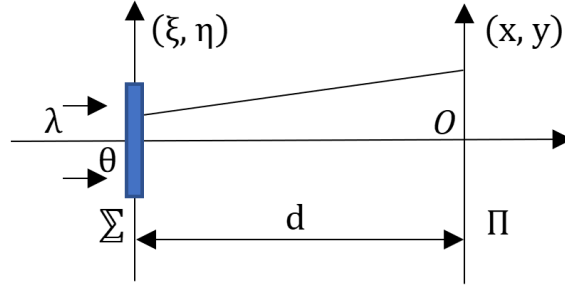


Figure 2.5: The model of diffraction.

### 2.1.3 Fresnel diffraction

In optics, the Fresnel diffraction is an approximation of the Kirchhoff–Fresnel diffraction [41, 42]. It is used to calculate the diffraction pattern created by waves passing through an aperture or around an object, when viewed from relatively close to the object. In contrast, the diffraction pattern in the far field region is given by the Fraunhofer diffraction equation.

The diffracting device shown in Fig. 2.6 takes the origin of coordinates as the center point  $\theta$ .  $M(\xi, \eta)$  is the point on the diffraction aperture  $\Sigma$ , and  $P(x, y)$  is the point on the observation plane  $\Pi$ .  $\Sigma$  and  $\Pi$  are parallel to each other with an interval of  $d$ . The propagation distance  $r$  from  $M$  to  $P$  is  $r = \sqrt{(x - \xi)^2 + (y - \eta)^2 + d^2}$ . When  $d \gg \max(\xi, \eta, x, y)$ ,  $r$  can be binomial expanded as

$$r = d + \frac{((x - \xi)^2 + (y - \eta)^2)}{2d} - \frac{[(x - \xi)^2 + (y - \eta)^2]^2}{8d^3} + \dots \quad (2.5)$$

Based on the paraxial axis approximation (i.e.  $d \gg \max(\xi, \eta, x, y)$ ), the denominator  $r$  of the integral Eq. 2.4 can be substitute by  $d$  since higher order components in Eq. 2.5 are negligible for amplitude. However, for phase delay  $kr$  in Eq. 2.4, the third and higher

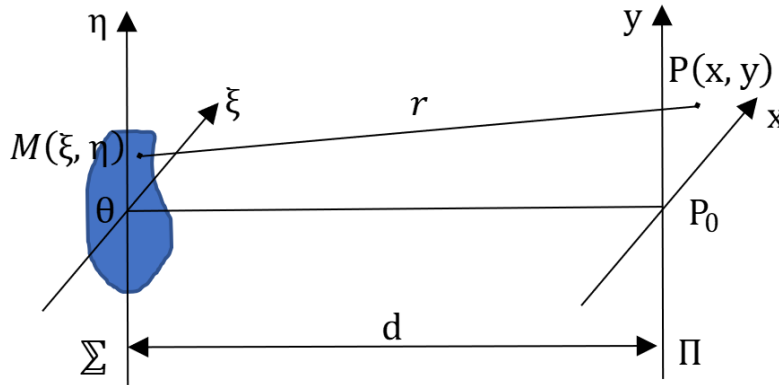


Figure 2.6: Model of Fresnel diffraction.

terms in  $r$  expansion is required to be less than  $\pi/2$  to meet the error limit, which means

$$\frac{2\pi}{\lambda} \frac{[(x - \xi)^2 + (y - \eta)^2]^2}{8d^3} \leq \frac{\pi}{2} \text{ or } d^3 \geq \frac{1}{2\lambda} [(x - \xi)^2 + (y - \eta)^2]^2. \quad (2.6)$$

With this condition,  $r$  in the exponential factor can be replaced by the first two terms of Eq. 2.5. This is called Fresnel approximation. Under Fresnel approximation, the Kirchhoff diffraction integral formula can be further simplified as

$$E(x, y) = \frac{1}{j\lambda d} e^{jk(d + \frac{x^2 + y^2}{2d})} \iint A(\xi, \eta) e^{j\frac{k}{2d}(\xi^2 + \eta^2)} e^{-j\frac{k}{d}(x\xi + y\eta)} d\xi d\eta. \quad (2.7)$$

This formula is called "Fresnel diffraction integral", and the observation area satisfying this formula is called "Fresnel diffraction area".

#### 2.1.4 Fraunhofer diffraction

In optics, the Fraunhofer diffraction equation is used to model the diffraction of waves when the diffraction pattern is viewed at a long distance from the diffracting object, and also when it is viewed at the focal plane of an imaging lens [43]. If the size of the diffraction aperture does not change in Fresnel diffraction pattern, and the distance  $z$  between the diffraction aperture and the observation plane is further increased, the diffraction pattern will be enlarged accordingly. Despite this, when the distance  $z$  of the observation surface exceeds a certain value, the phase error introduced by the square term of the diffraction

aperture will be less than  $\pi/2$ , which is

$$\frac{2\pi}{\lambda} \frac{\xi^2 + \eta^2}{2d} \leq \frac{\pi}{2}. \quad (2.8)$$

In this case, the  $(\xi^2 + \eta^2)/2d$  item in the second term of Eq. 2.7 can be omitted, and further approximation of  $r$  in the complex exponent term in Eq. 2.5 is

$$r = d + \frac{((x - \xi)^2 + (y - \eta)^2)}{2d} - \frac{x\xi + y\eta}{d}. \quad (2.9)$$

This approximation is called the Fraunhofer approximation. Under Fraunhofer approximation, the Kirchhoff diffraction integral formula is further simplified as

$$E(x, y) = \frac{1}{j\lambda d} e^{jk(d + \frac{x^2 + y^2}{2d})} \iint A(\xi, \eta) e^{-j\frac{k}{d}(x\xi + y\eta)} d\xi d\eta. \quad (2.10)$$

### 2.1.5 Thin lens Fourier transform

From the perspective of wave optics [33], the role of the lens is nothing more than a phase converter, which bends the light by introducing phase delay. The magnitude of the phase delay is proportional to the optical thickness of the lens. In other words, the lens can be used as a pure non-directional modulating element. The optical thickness corresponding to a phase delay of an integer multiple of  $2\pi$  in the lens can be bypassed in calculation since the waves have a period of  $2\pi$ , i.e. the geometric optical translation of the light when passing through this part of the lens can be ignored. Such a lens is called a thin lens. Referring to Fig. 2.7a, the lens locates in plane  $(\xi, \eta)$ . The maximum thickness of the lens is  $\Delta_0$ . The thickness at point  $(\xi, \eta)$  is  $\Delta(\xi, \eta)$ , which is called the thickness function of the lens. When light passes through from the entrance pupil plane  $U_1$  to the exit pupil plane  $U_1'$ , the total phase delay is

$$\phi(\xi, \eta) = kn\Delta(\xi, \eta) + k[\Delta_0 - \Delta(\xi, \eta)], \quad (2.11)$$

where  $n$  is the refractive index of the lens material. Therefore, the effect of the lens on the incident light wave can be described by a phase transformation factor, expressed as

$$T_l(\xi, \eta) = e^{j\phi(\xi, \eta)} = e^{jk\Delta_0} e^{jk(n-1)\Delta(\xi, \eta)}. \quad (2.12)$$

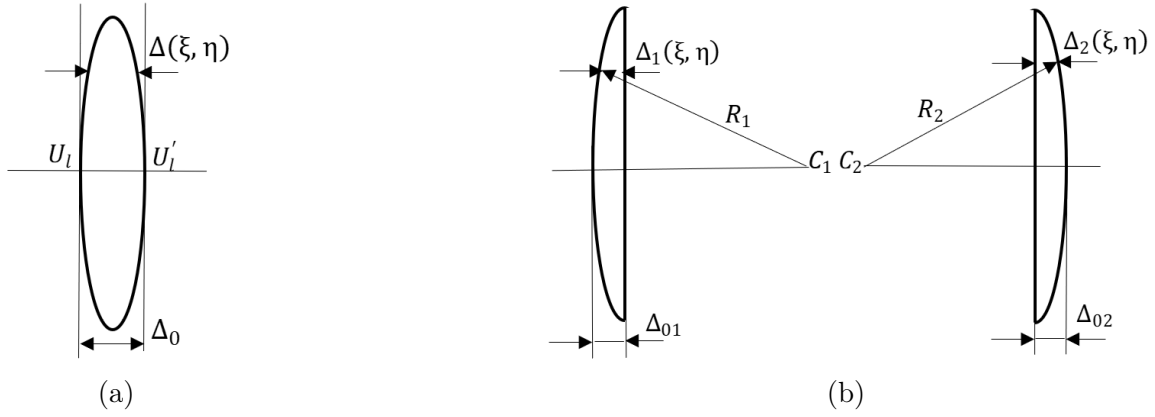


Figure 2.7: Model of thin lens (a) the whole lens and (b) the half lenses.

As long as the field distribution of light  $u_l(\xi, \eta)$  on the entrance pupil plane of the lens is known, the field distribution  $u'_l(\xi, \eta)$  on the exit pupil plane of the thin lens can be obtained immediately from the viewpoint of phase modulation, which is

$$u'_l(\xi, \eta) = u_l(\xi, \eta)T_l(\xi, \eta). \quad (2.13)$$

In order to find  $\Delta(\xi, \eta)$ , the method shown in Fig. 2.7b splits the lens into two halves are utilized. It specifies that when the light propagates from left to right, the radius of curvature of the convex spherical surface is positive, the radius of the concave sphere curvature is negative (in Fig. 2.7b,  $R_1 > 0$  and  $R_2 < 0$ ). It is easy to find applying the geometric relationship, one can get

$$\Delta(\xi, \eta) = \Delta_1(\xi, \eta) + \Delta_2(\xi, \eta) = \Delta_0 - R_1 \left(1 - \sqrt{1 - \frac{\xi^2 + \eta^2}{R_1^2}}\right) + R_2 \left(1 - \sqrt{1 - \frac{\xi^2 + \eta^2}{R_2^2}}\right). \quad (2.14)$$

For a thin lens, the paraxial approximation holds for

$$\sqrt{1 - \frac{\xi^2 + \eta^2}{R^2}} \approx 1 - \frac{\xi^2 + \eta^2}{2R^2}. \quad (2.15)$$

The thickness function thus can be simplified as

$$\Delta(\xi, \eta) = \Delta_0 - \frac{\xi^2 + \eta^2}{2} \left( \frac{1}{R_1} - \frac{1}{R_2} \right). \quad (2.16)$$

Bringing Eq. 2.16 in Eq. 2.12 and applying the focal length formula ( $1/f = (n - 1)(1/R_1 - 1/R_2)$ ) of the lens, the phase transformation factor of the lens can be obtained immediately as

$$T_l(\xi, \eta) = e^{jk\Delta_0} e^{-j\frac{k}{2f}(\xi^2 + \eta^2)}. \quad (2.17)$$

Although Eq. 2.17 is derived for convex lenses, the signing rules used make this result fitting for other types of lenses. The first factor in the formula represents a uniform phase delay. The second factor represents the Fresnel approximation of spherical waves. When the focal length  $f$  is positive, it is a converging spherical wave.  $T_l(\xi, \eta)$  represents the phase transformation factor of the convex lens. When  $f$  is negative, it corresponds to a diverging spherical wave.  $T_l(\xi, \eta)$  is hence the phase transformation factor of the concave lens. In addition, although the phase transformation effect represented by Eq. 2.17 depends on a large extent on the establishment of the paraxial approximation, this conclusion remains true as long as the lens has undergone strict aberration correction.

The phase transformation effect of the lens is determined by the intrinsic nature of the lens, regardless of the incident light, whether it is a plane wave, spherical wave or a complex wave. As long as the aforementioned conditions, paraxial approximate or strict phase difference correction is fulfilled, the lens can achieve phase transformation of the incident light wave in the form of Eq.2.17.

### 2.1.6 Fraunhofer diffraction in a finite distance

According to Eq. 2.10, accurate Fraunhofer diffraction can be observed only on the plane with the distance  $d = \infty$ . In order to observe the Fraunhofer diffraction at a limited

distance in the laboratory, the phase transformation property of a convex lens can be used. The appropriate field distribution in the back focal plane of the lens is equivalent to the Fraunhofer diffraction of the object. For simplicity, only the case of plane wave illumination is described here. Other illuminating fashions can also be analyzed in the same way. The sketch is shown in Fig. 2.8. Two cases with diffracting object in front of and after the focusing lens  $L$  are specified. The diffracting object has a complex transmitting coefficient of  $T(\xi, \eta)$ . It is placed on the plane  $\Sigma$  and illuminated by a monochromatic plane wave with unit amplitude of  $B(\xi, \eta) = 1$ . With the phase conversion factor  $T_l(\xi, \eta)$  of  $L$ , the complex light wave propagated from the diffracting aperture  $\Sigma$  (Fig. 2.8a) or the last surface of  $L$  (Fig. 2.8b) can be written immediately as

$$A'(\xi, \eta) = B(\xi, \eta)T_l(\xi, \eta)T(\xi, \eta) = A(\xi, \eta)E_{l0}e^{-j\frac{k}{2f}(\xi^2+\eta^2)}. \quad (2.18)$$

The propagation of the waves from plane  $\Sigma$  to plane  $\Pi$  is Fresnel diffraction. Thus

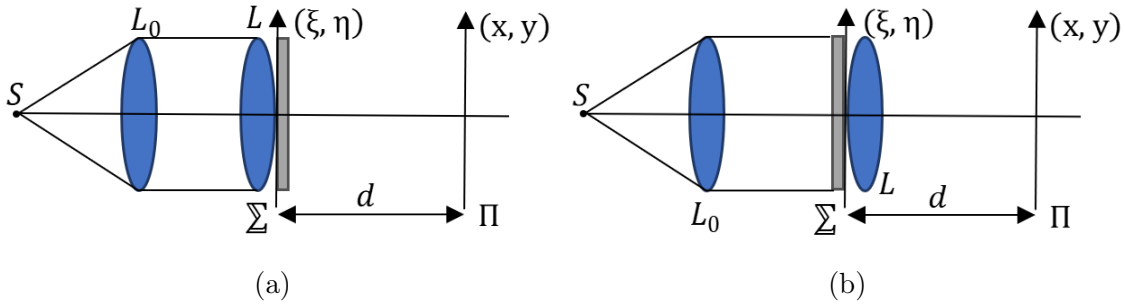


Figure 2.8: Plane wave illumination diffraction device. (a) Diffracting object is located behind the lens, (b) diffracting object is located before the lens.

using  $A'(\xi, \eta)$  instead of  $A(\xi, \eta)$  in Eq. 2.7, one can obtain the field distribution on  $\Pi$  plane by

$$E(x, y) = \frac{1}{jd\lambda} e^{jk(d + \frac{x^2+y^2}{2d})} \iint A'(\xi, \eta) e^{j\frac{k}{2d}(\xi^2+\eta^2)} e^{-j\frac{k}{d}(x\xi+y\eta)} d\xi d\eta. \quad (2.19)$$

If  $d = f$ , Eq. 2.19 can be simplified as

$$E(x, y) = \frac{E_{l0}}{jd\lambda} e^{jk(d + \frac{x^2+y^2}{2d})} \iint A(\xi, \eta) e^{-j\frac{k}{d}(x\xi+y\eta)} d\xi d\eta. \quad (2.20)$$

One can find that Eq. 2.20 and Fraunhofer diffraction integral Eq. 2.10 have exactly the same form, which shows that with the convex lens such as that shown in Fig. 2.8a, the Fraunhofer diffraction can be observed in finite distance (on the back focal plane of the convex lens). This has very important values in practical application.

### 2.1.7 Fourier transform in diffraction computing

Both Fresnel diffraction (Eq. 2.7) and Fraunhofer diffraction (Eq. 2.10) has the linear complex exponential factor  $e^{-j\frac{k}{d}(x\xi+y\eta)} = e^{-j2\pi(\frac{x}{\lambda d}\xi + \frac{y}{\lambda d}\eta)}$ . Holding  $f_\xi = x/(\lambda d)$ ,  $f_\eta = y/(\lambda d)$ , the above exponential factor can be expressed as  $e^{-j2\pi(f_\xi\xi + f_\eta\eta)}$ . In wave optics, it can represent a three-dimensional simple harmonic plane wave with a spatial frequency of  $(f_\xi, f_\eta)$ , and has the same form as the two-dimensional Fourier transform kernel in Fourier analysis. The integral in Eq. 2.20 therefore can be expressed as

$$a(f_\xi, f_\eta) = \iint A(\xi, \eta) e^{-j2\pi(f_\xi\xi + f_\eta\eta)} d\xi d\eta. \quad (2.21)$$

This is the two-dimensional Fourier transform of the transmitted wave  $A(\xi, \eta)$  after passing through a diffracting object, which means the Fraunhofer diffraction of  $A(\xi, \eta)$  is equal to the product of the two-dimensional Fourier transform  $a(f_\xi, f_\eta)$  by a complex constant  $g(x, y)$

$$E(x, y) = g(x, y)a(f_\xi, f_\eta), \quad (2.22)$$

where  $g(x, y) = \frac{E_{l0}}{jd\lambda} e^{jk(d + \frac{x^2+y^2}{2d})}$ .

## 2.2 Principle of Fourier imaging

Based on the demonstration of diffraction in Section 2.1 of this chapter, one can find that the Fraunhofer diffraction  $E(x, y)$  is equal to the product of the Fourier transform  $t(f_\xi, f_\eta)$  of the complex aperture transmitted coefficient  $T(\xi, \eta)$  and a complex constant. In other words, using the convex lens, a two-dimensional Fourier transform of the object distribution can be achieved in the back focal plane. This opens up a new way to accomplish the Fourier transform by optical methods, which differs from the digital fast Fourier transform (FFT). It is analog two-dimensional parallel processing. The speed is fast as the speed of light. It is therefore called an optical analog Fourier transform, or simply an optical Fourier transform. In the later chapter of this research, the Fraunhofer diffraction pattern will also be called Fourier-space spectrum. An optical imaging system is used to record, filter, and process the spatial field distribution of the Fourier-space spectrum, thereby achieving a special functional imaging method which is called the Fourier imaging technology. This research will mainly focus on recording the Fourier-space spectrum coherently and reconstructing the observed information by numerical calculation.

### 2.2.1 Model of Fourier imaging

As Section 2.1.6 demonstrated, in the focal plane of a convex lens, one can observe the Fraunhofer diffraction of the waves modulated by the imaged object directly in front of the convex lens or just after the lens. However, in a practical experiment or 3D imaging applications, it still has some difficulties to ideally comply the process. To have a larger imaging range, observation of the object to be imaged away from the convex lens needs to be considered. As Fig. 2.9 shows, the complex transmission coefficient of the object is defined as  $T(\xi, \eta)$ . It is located in a plane with a distance of  $d_0$  in front of the lens and illuminated by a monochromatic plane wave with unit amplitude. Let us define the Fourier-space spectrum of an object as  $t(f_\xi, f_\eta)$ , the complex amplitude of the radiation projected onto the entrance pupil of the lens after going through the object as  $T'(\xi, \eta)$ , and its Fourier spectrum as  $t'(f_\xi, f_\eta)$ . The complex field distribution on the back focal plane of the lens is  $E(x, y)$ . Assuming that the aperture of the lens is large enough,

thus it will not limit the high-frequency components of  $t(f_\xi, f_\eta)$ . Based on the Fresnel diffraction and Fourier transform formulas we have

$$t'(f_\xi, f_\eta) = e^{jkd_0} e^{-j\pi\lambda d_0(f_\xi^2 + f_\eta^2)} t(f_\xi, f_\eta), \quad (2.23)$$

where  $t(f_\xi, f_\eta) = \mathfrak{F}[T(\xi, \eta)]$ ,  $\mathfrak{F}$  denotes Fourier transform.

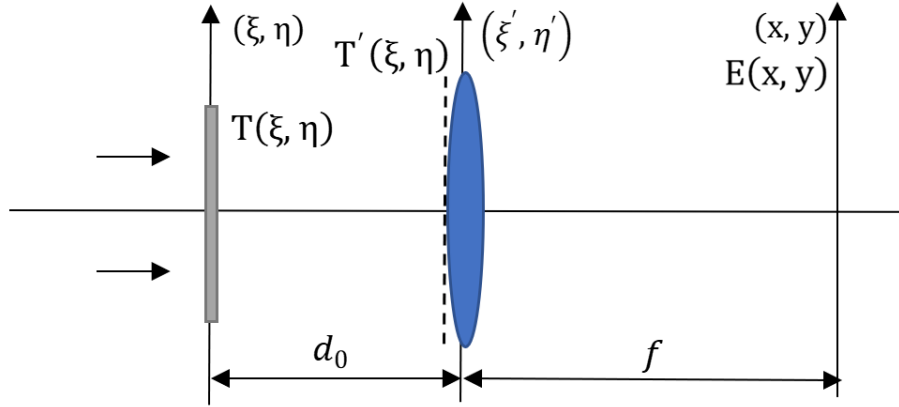


Figure 2.9: Fourier transform beam path with object in front of lens.

According to the analysis in Section 2.1.6 and 2.1.7, the complex field distribution  $E(x, y)$  on the back focal plane  $\Pi$  of the lens is equal to the Fraunhofer diffraction of the object on the entrance plane of the lens. From Eq. 2.22 one will find

$$E(x, y) = \frac{E_0}{jd\lambda} e^{jk(f + \frac{x^2 + y^2}{2f})} \iint T'(\xi', \eta') e^{-j2\pi(f_\xi \xi' + f_\eta \eta')} d\xi' d\eta', \quad (2.24)$$

where  $f_\xi = x/(\lambda f)$ ,  $f_\eta = y/(\lambda f)$ . Bringing Eq. 2.23 into 2.24 one will get

$$E(x, y) = \frac{E_0}{jd\lambda} e^{jk(d_0 + f)} e^{j\frac{k}{2f}(1 - \frac{d_0}{f})(x^2 + y^2)} \iint T(\xi, \eta) e^{-j2\pi(f_\xi \xi + f_\eta \eta)} d\xi d\eta. \quad (2.25)$$

Suppose that  $g(x, y) = \frac{E_0}{jd\lambda} e^{jk(d_0 + f)} e^{j\frac{k}{2f}(1 - \frac{d_0}{f})(x^2 + y^2)}$ , Eq. 2.25 can be rewritten as

$$E(x, y) = \frac{E_0}{jd\lambda} \exp[jk(d + f)] \exp[j\frac{k}{2f}(1 - \frac{d}{f})(x^2 + y^2)] t(f_\xi, f_\eta), \quad (2.26)$$

$$E(x, y) = g(x, y)t(f_\xi, f_\eta), \quad (2.27)$$

where  $g(x, y)$  consists of a complex constant and a paraboloidal phase item related to  $(x^2 + y^2)$ , so the light field distribution  $E(x, y)$  on the back focal plane  $\Pi$  of the lens is not equal to the exact Fourier transform of the amplitude transmission coefficient  $T(\xi, \eta)$ . It has the same amplitude distribution as the Fourier transform, but the phase is the sum of the Fourier transform spectrum phase and the two-dimensional paraboloidal phase.

According to the second item in the phase part of  $g(x, y)$ , the distance information is mathematically encoded in the phase distribution in the focal plane of the imaging system ("lens"). Thus recording the phase info in the focal plane enables the system 3D imaging capability. The distance-encoding in the phase information is illustrated in Fig. 2.10, which displays the phase profile of a circular aperture centered on the optical axis. Fig. 2.10(b) presents the phase term  $\frac{k}{2f}(1 - \frac{d_0}{f})(x^2 + y^2)$  for different object locations. For an object placed at the front focal plane ( $d_0 = f$ ), one obtains a flat phase contribution. Away from the focal plane, the phase has a paraboloidal shape, with a sign and magnitude of the curvature unambiguously dependent on  $d_0$ . This phase contribution is to be added to that determined by the object itself which in our case is the circular aperture (with the phase profile of Fig. 2.10(a)). Fig. 2.10(c) shows the total phase in the Fourier plane for the five distances of the aperture of Fig. 2.10(b). Comparing the resultant phase contours, one will find the influence of the distance. For more complex objects, it is usually not straightforward to visually identify the distance information in a phase image without the help of suitable computer-based analysis.

As illustrated above, the Fourier space spectrum theory can be integrated into the THz regime to remove the barriers in the path of bringing THz technology into practical applications. The model of the Fourier imaging in this research will be built to position the detector in the focal plane (coordinates:  $x, y$ ) of the optical system, where the beam cross-section is smallest along the entire beam path. As with other coherent imaging techniques such as phase-shift interference imaging, holography, in-line holography as well as off-axis holography, near-field holography and time-reversal holographic imaging

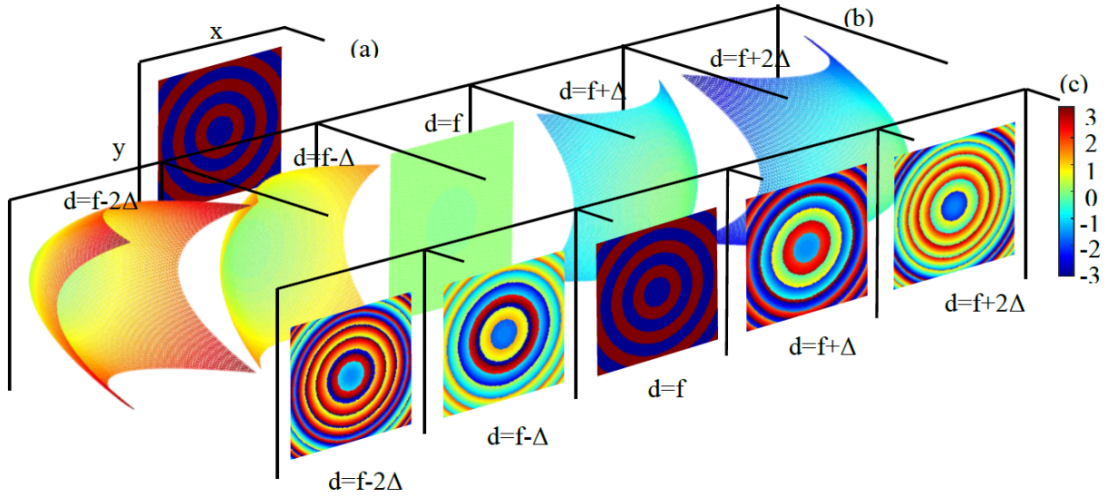


Figure 2.10: Phase simulation of Fourier imaging. (a) The phase profile of a circular aperture. (b) Distance-related phase contribution for various positions of the aperture. The paraboloidal phase surface is concave (convex) if the aperture is placed more (less) than a distance  $d$  in front of the lens. (c) Total phase in the focal plane (Fourier plane) of the lens.

of hidden objects, the image is then calculated numerically from the recorded data. The field-of-view is determined by the pixel pitch with which the field has been recorded, and not by the size of the detector array as in conventional imaging (with conventional imaging, we mean here and in the following the recording of the spatial distribution of the radiation intensity in the image plane of the lens for a given object distance).

## 2.2.2 Advantages of Fourier imaging

### Large field-of-view

In imaging setups, diffraction limit affects THz radiation stronger than visible radiation due to the much longer wavelength of the THz radiation, which also results in the cameras at THz spectral regime will never have comparable high pixel density with cameras at the visible spectral range and leads to a reduced field-of-view which can be obtained directly, i.e., without scanning with the help of movable optical elements in the camera system. Thus, the establishment of a Fourier imaging setup in THz frequencies enables a feasible placement of detectors, only if the detectors meet the sub-Nyquist sampling rate, which

will solve the problems of lacking of megapixel cameras at this regime. Fig. 2.11 displays the simulation results of the Fourier system and the traditional setup with the same parameters, in contrary to the field-of-view cut-off in an ordinary system, image results show, even if the detection area in the plane is limit, the reconstruction image from the Fourier spectrum can still cover the whole area of the imaging target.

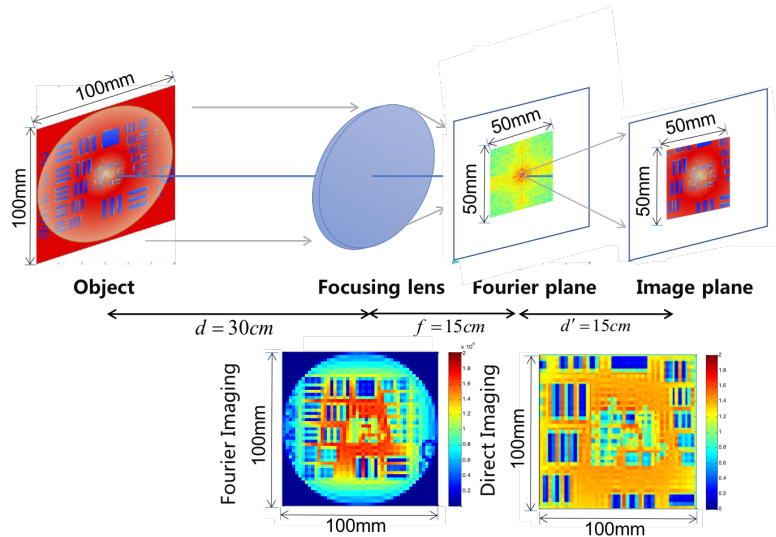


Figure 2.11: Generic Fourier imaging approach. Top: Schematic of a basic imaging set-up for the example of a  $2f$  geometry. The object (here a 1951 USAF resolution test chart) is located at a distance  $2f$  in front of the imaging lens. Also shown is the real part of the spatial Fourier spectrum of the object in the focal plane of the imaging lens and the intensity image in the image plane at a distance  $2f$  behind the lens. Bottom left: Example of numerical image reconstruction with a detector array covering  $50 \times 50 \text{ mm}^2$ . With a pixel pitch of  $0.1 \text{ mm}$ , the whole test chart is covered. Bottom right: Conventional imaging: The lens aperture only allows one to cover the central region of the test chart.

### 3D imaging and error suppression

Being a coherent image recording technique, Fourier imaging has a close conceptual relationship with other phase-resolving techniques such as phase-shift interference imaging [44, 45], holography [46], in-line holography [47–49], off-axis holography [50–53], near-field holography [54] and time-reversal holographic imaging of hidden objects [55]. There exists, however, an important difference to these techniques. All of these capture the

phase information by interfering with the beam arriving from the illuminated scene with a reference beam. This approach has two disadvantages. First, it induces errors because the reference beam is not ideally collimated as usually assumed in the calculations. Second and more important, it tends to suffer from a limited lateral spatial resolution because the (usually) weak signals of the high spatial frequency components are easily buried in the noise. Single-pixel heterodyne detection, which we apply in our Fourier imaging technique, in contrast, has an amplification aspect to it, as it mixes the weak signal with a strong reference beam, concentrated on the detector to generate an enhanced signal at the intermediate frequency for data processing. This leads to a diffraction-limited spatial resolution as shown in [47].

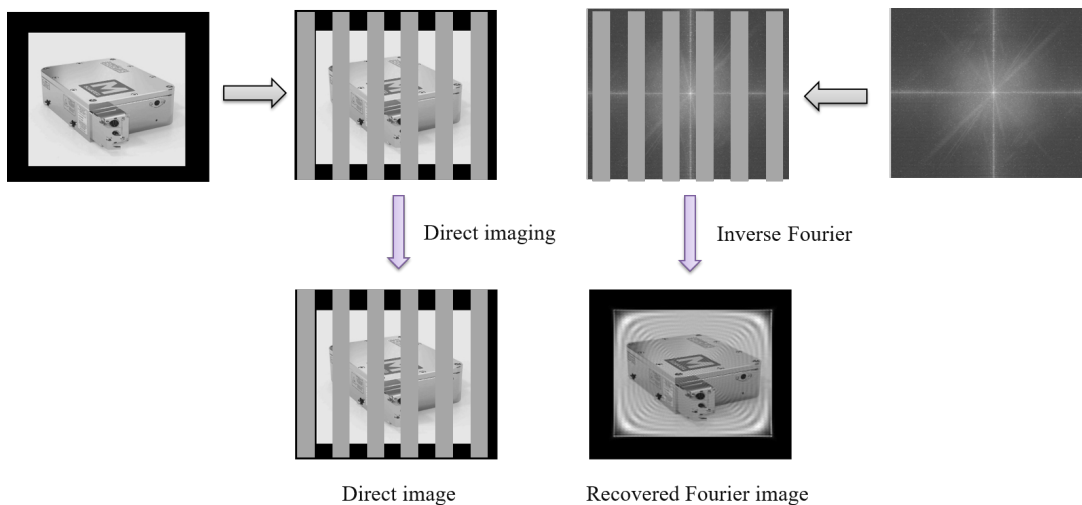
Fourier imaging also offers the possibility of 3D imaging. As stated above (Fig. 2.10), 3D imaging means here to exploit the fact that the distance of any object point from the lens is encoded in the phase-front curvature of the light arriving at the focal plane. With this distance information, it is possible to numerically focus on any plane in front of the imaging lens and to determine how the object looks like in this plane (provided THz radiation from these object points has arrived in the detection plane).

Fourier imaging also allows to correct the image data for lens-induced aberrations (deviations from the ideal thin-lens behavior). The computer calculations used for object reconstruction allow compensating known aberrations induced by the optical system.

### **Compresses sensing capability**

Another aspect which speaks for Fourier imaging as a modality to be applied more in the THz frequency regime is that, conceptually, it lends itself to the application of compressed sensing techniques [56–58] because much of the information of the Fourier spectrum is sparse [57, 59]. The advantage of this technique is that it can detect an object obscured by another object in the beam path with single frame recorded data if enough scattered light from the targets arrives at the detection plane, which has never been reported in the presented literature of 3D imaging, such as phase-shift interference imaging, holography, in-line holography as well as off-axis holography, near-field holography [60, 61] and time-reversal holographic imaging of hidden objects [62].

Furthermore, because of the sparsity of the recorded data, part of the detection information loss or low detection sampling rate will still have the a large field of view, and all the information in the range rather than image information loss as shown in conventional imaging method shown in Fig. 2.12. For single-pixel scanning detection system often adopted in THz regime, this technique will reduce the imaging time, for camera detection system, it can cut down pixel size requirements, which makes real-time imaging with high quality is possible in THz range.



5

Figure 2.12: Imaging field of view comparison between Fourier imaging and conventional direct imaging.

### Numerical focusing makes the system more compact and enhances the resolution

In Fourier optics, there is a typical 4-f imaging system as shown in Fig. 2.13, the first lens focuses the beam into the Fourier space frequency domain, in the focal plane 2D analog filter can be applied, then the second focal lens transfers the Fourier spectrum back to the space domain for detection. In theory, both the focusing lens should be thin lenses, but in reality, it is impossible, thus the aberrations exist in the imaging system. While using computer calculation to substitute the second focal lens to act as the numerical optical system virtually, one can compensate the aberrations induced by the first focal

lens. The virtual system can be complex to achieve the function with multi-piece of lenses but without radiation.

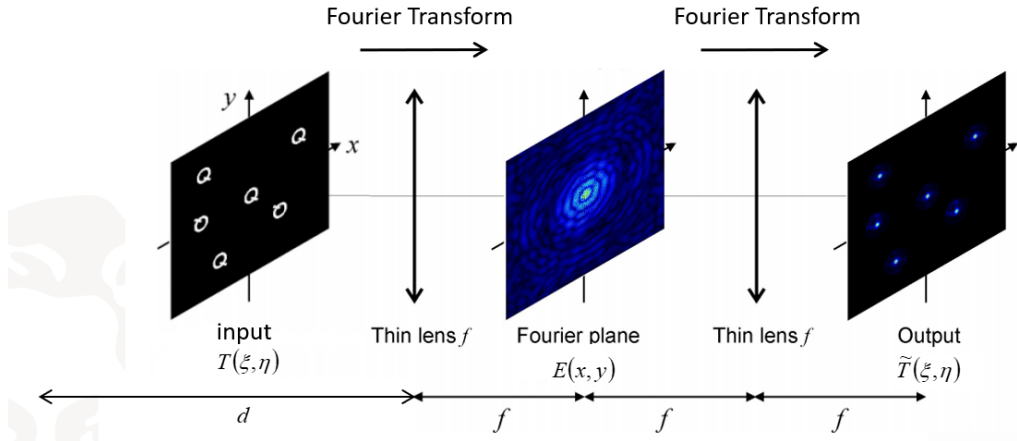


Figure 2.13: Typical 4-f imaging system.

Moreover, thanks to the computer numerical calculation of decoding of the Fourier spectrum, the paraboloidal phase part in Eq. 2.25 can be removed numerically, the object distance, therefore, can be extended/ shortened to any value rather than equal to the focal length of the first focal lens in the 4-f system. Compared to conventional imaging approaches where the imaging target must be placed more than the focal length away of the focusing system to get the real image of the scene to be captured, Fourier imaging enables the lateral resolution enhancement by allowing the placement of the imaging target to break the location limit, positioned more close to the focusing system. The higher resolution can be attributed to less higher space frequency components loss during the shorter signal propagation.

### THz camera integration potential

Finally – with a view towards future Fourier imaging with focal plane arrays operated in heterodyne mode, one should note that Fourier imaging bears other advantages that are exceptionally well suited to mitigate the challenges of imaging at terahertz (THz) frequencies. These arise because the diffraction limit of the lateral spatial resolution affects the practically attainable pixel numbers useful in THz imaging severely, and much more strongly than imaging in the visible (VIS), which is a consequence of the much longer

wavelength of the THz radiation (1 THz corresponds to a wavelength  $\lambda$  of 300  $\mu\text{m}$  in free space). As the diffraction-limited area of the focal spot for a given focal length of a lens scales with  $\lambda^2$ , the pixel area of a THz detector has to be by a factor of  $10^5$  larger than that of a pixel for VIS light. As the price of semiconductor-based detectors scales with the chip area, a focal-plane array of a THz camera will never have the multi-megapixel size of modern VIS cameras. The effective pixel number may reach  $10^5$  perhaps and will be significantly smaller for sub-THz frequencies. With conventional imaging (recording the intensity profile in the image plane of the lens), one will then not be able to cover a large field-of-view with good spatial resolution directly; one will be forced to scan the scene with the help of movable optical elements. At the least, the scanning adds complexity and costs, and increases the recording time. In contrast, Fourier imaging benefits from the facts that the effective beam area is smallest in the Fourier plane and that the size of the field-of-view of the scene is only determined by the pixel pitch with which the field is recorded there. If one has only a small detector array ("small" meaning here to have a comparatively low number of pixels in the array), then one can still monitor a comparatively large field-of-view, as is illustrated in Fig. 2.11. This comes at the price of a limited spatial resolution, which is determined by the size of the array (i.e., by how much of the spatial Fourier spectrum one can cover with the detector array). Often in practical applications, it is more important to obtain a fast overview of a scene to decide whether an image with a better resolution is desired. This can then be achieved by translating the detector array in the focal plane to record higher Fourier components in reciprocal space.

## 2.3 Simulation of Terahertz Fourier imaging

Imaging at terahertz (THz) frequencies offers interesting features for technical applications. Among these are the transparency of many materials which provides the ability to look into and through objects such as packages and technical materials, the existence of spectral fingerprints for the identification of substances, and the weak scattering by dust, smoke and mist, which makes THz radiation interesting for imaging under challenging ambient conditions in a radarlike fashion [63], but with better spatial resolution. The

latter could be promising e.g. for robotics and autonomous vehicles. Many of these envisaged applications would operate in the deep sub-THz frequency regime (approximately 0.1-0.6 THz), where the large wavelength of the radiation makes it difficult and expensive to build detector arrays which exhibit a sufficient number of detectors needed for high frame rates together with good image quality, as defined by a sufficiently large field-of-view with acceptable spatial resolution. For this reason, the integrated detector arrays which are currently being available [64–69], with pixel numbers of less than ten thousand, are only of limited usefulness for standard two-dimensional (2D) imaging as well as for three-dimensional (3D) computed tomography [28, 32], because the detectors cover only a small field-of-view with good resolution.

An alternative is Fourier imaging with the detector array being positioned in the focal plane of the optical system, where the beam cross-section is smallest along the entire beam path. As with other coherent microwave and THz imaging techniques such as phase-shift interference imaging [44, 45], holography [46], in-line holography [49, 70] as well as off-axis holography [50–53], near-field holography [54] and time-reversal holographic imaging of hidden objects [55], the image is calculated numerically from the recorded data. The field-of-view is determined by the pixel pitch with which the field has been recorded, and not by the size of the detector array as in conventional imaging.

### 2.3.1 Simulation of THz Fourier imaging setup with simple samples

To have an easier subsequent resolution demonstration and image quality comparison, the work here will look at differences between the practical imaging system and the simulation. The photo of a 1951 USAF test chart (microscopic optical resolution test device originally defined by the U.S. Air Force MIL-STD-150A standard of 1951) as shown in Fig. 2.14, a Siemens star (alias: spoke target, a device used to test the resolution of optical instruments, printers, and displays) depicted in Fig. 2.19 and a two-dimension grids drawn as Fig. 2.24 are utilized as the target objects for simulation. These three objects are also used as the imaging targets in the experiment, the pictures of the real

objects will be shown in the experimental part. Furthermore, in order to be as close to the experimental scene, the collimated Gaussian beam with 2-inch aperture is projected onto the simulated objects, the beam center is shifted a little bit from the optical axis, and the pixel size of the simulated object is imitated and adjusted according to the actual experimental scene. Next, the adjustment of different target objects and the Fourier spectrum distribution generated by simulation will be analyzed.

### Simulation of USAF chart

A 1951 USAF resolution test chart is a resolution test device originally defined by the U.S. Air Force MIL-STD-150A standard of 1951 [71]. The design provides numerous small target shapes exhibiting a stepped assortment of precise spatial frequency specimens. The full standard pattern consists of 9 groups as Fig. 2.14 shows, with each group consisting of 6 elements; thus there are 54 target elements provided in the full series. Each element consists of three bars that form a minimal Ronchi Ruling. The scales and dimensions of the bars are given by the expression of

$$Resolution(lp/mm) = 2^{Group+(element-1)/6}. \quad (2.28)$$

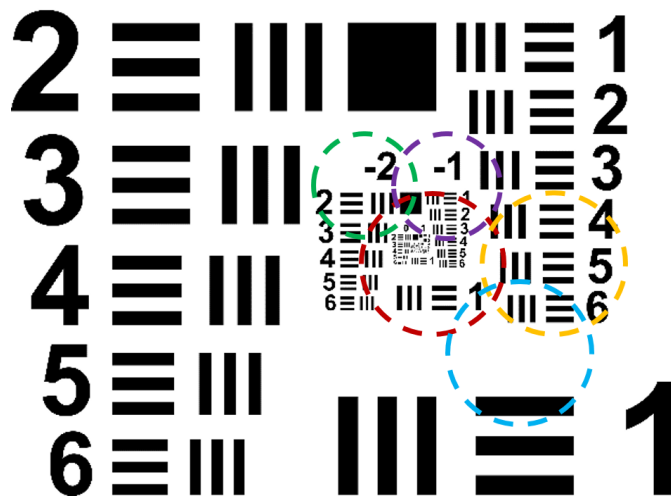


Figure 2.14: Photo of USAF chart test target.

The simulation of different selected parts will be presented depending on the imaging

radiation wavelength, scales and the dimensions of the bars on the USAF chart. In this thesis, the validation frequencies of the Fourier imaging are 300 GHz and 600 GHz. Therefore, the areas circled by the red, yellow and blue dashed rings in Fig. 2.14 are selected as the target for the 300-GHz radiation case, the ones indicated by the green and purple dashed rings are used for the 600-GHz radiation case. The size of the rings is decided by the aperture size of the quasi-Gaussian beam generated by the collimation lens (the values will be analyzed in Section 3.1.2).

The selected targets (circled by the red, yellow and blue dashed rings) illuminated by the 300-GHz Gaussian beam are shown as the top to the bottom panels in the first column of Fig. 2.15. Here, the object distance for each sample is set as 10 cm, the focal length of the Fourier lens is 15 cm, the effective aperture size of the illuminated Gaussian beam is 5.5 cm. The corresponding intensity and phase of the Fourier spectrum, generated by applying the mathematical principles as Eq. 2.27 describes can be displayed by the second and third columns in Fig. 2.15, respectively. The corresponding reconstructed images are shown in Fig. 2.16.

For practical experiment at 600 GHz, the utilized illuminating radiation has a relatively low power of 56 pW. That only allows a relatively small aperture size of 4 cm. A 4-cm aperture-size Gaussian beam is therefore projected onto the imaging targets to have the closest simulation. The imaging results at 600 GHz will have a better resolution than that at 300 GHz, thanks to the shorter intrinsic wavelength, thus the -2 and -1 group were selected as the imaging targets (indicated by the green and purple dashed circles in Fig. 2.14). The corresponding Gaussian beam illuminated targets can be shown as the top and bottom plots in the first column in Fig. 2.17. The generated intensity and phase Fourier spectrum are shown in the top and bottom rows in the second and third columns. The data in the second column are the intensities and those in the third column are the phase spectrum. Here, a 6-cm object distance and a focusing lens with a 5-cm focal length are adopted. From the Fourier spectrum, one can see, the focus point is smaller than that at 300 GHz. This is because of the shorter wavelength and focal length. Correspondingly, the resolution will be better.

With the same reconstruction method as 300 GHz, the images retrieved based on the

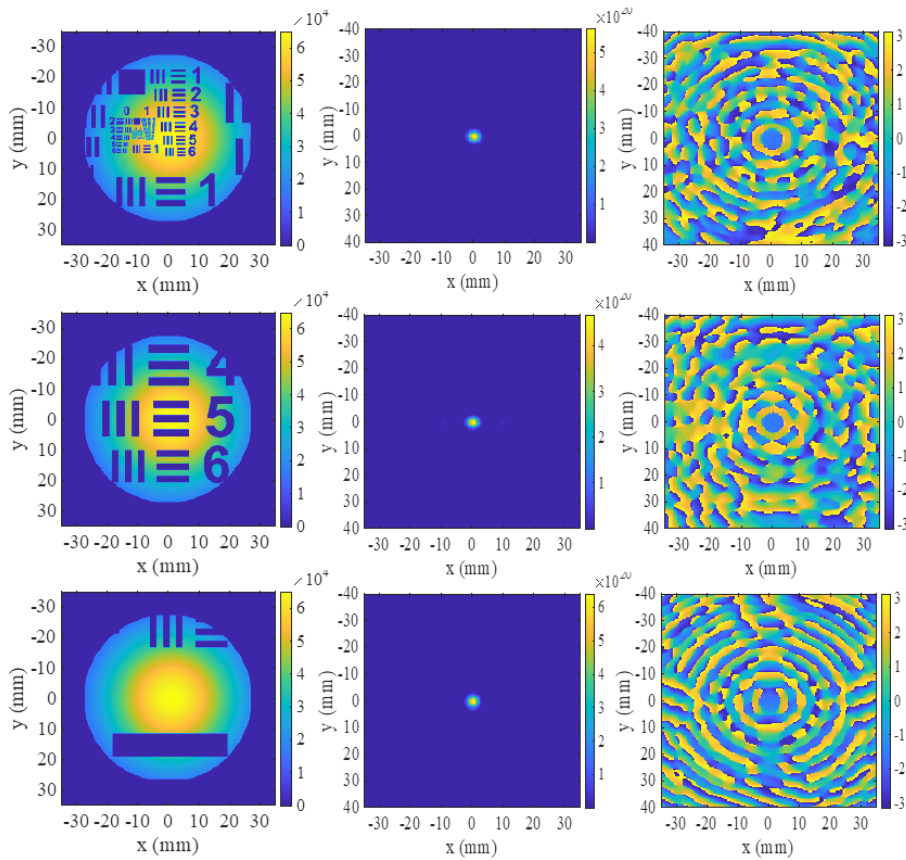


Figure 2.15: Fourier spectrum simulation of three different parts of the USAF chart. The panels in the first column are the imaged targets illuminated by the Gaussian beam. The panels in the second column are the intensity of Fourier spectrum distributions. The panels in the third column are the Fourier phase distributions.

Fourier spectrum in Fig. 2.17 are shown in Fig. 2.18, the top and bottom rows correspond to the object order in Fig. 2.17. The plots in the first column show the absolute intensity distributions, those in the second column display the intensity in log scale, the ones in the last column present the phase. From the simulated reconstructed image, one could get that, the resolution at 600 GHz is better than that at 300 GHz as conceived. The relationship between the resolution and the wavelength, the focal length of the system will be investigated in Chapter 5.

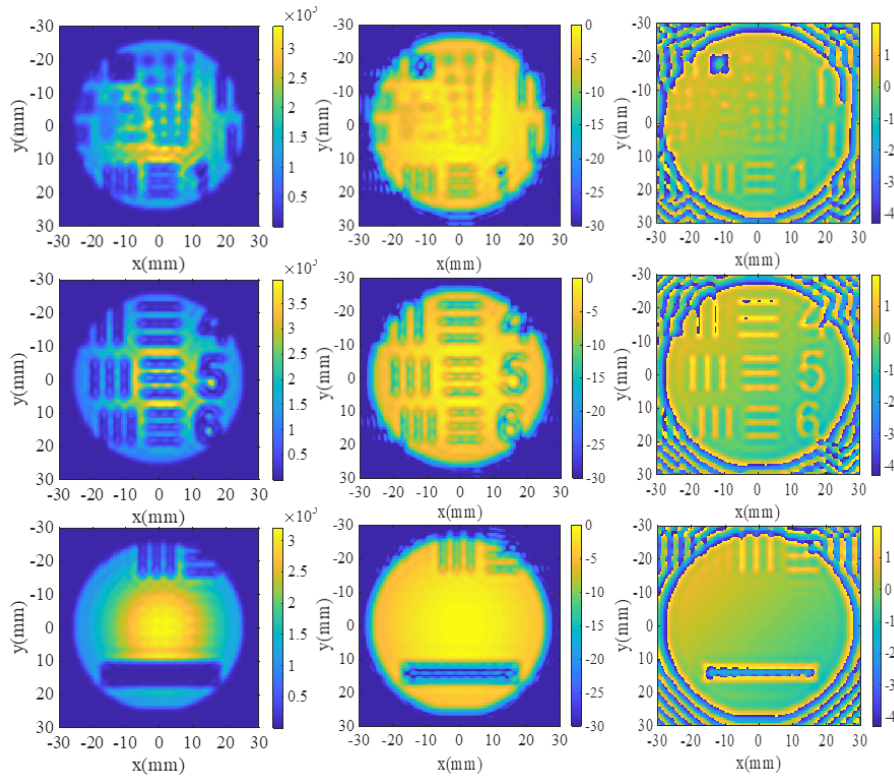


Figure 2.16: The reconstructions of each imaged targets in Fig. 2.15. The plots in the first column are the intensity reconstructed image. The plots in the second column are the intensity in the log scale. The plots in the third column are the phase reconstructed image.

### Simulation of Siemens star

Siemens star is another resolution verification device, which is more representative in all directions than the USAF resolution chart. Here, the simulations of the Siemens star target will be presented. The Siemens star exists as Fig. 2.19. The area circled by the red dashed line will be used for 300 GHz simulation and experiment, the green dashed line separates the part for 600 GHz imaging.

At 300 GHz, the area of the Siemens star off the center is selected as the imaged target to have a wider resolution validation range. The simulation of the selected area illuminated by the 5.5 cm diameter Gaussian beam is shown as the left panels in Fig. 2.20. The generated intensity and phase Fourier spectrum are shown as the middle and right plots in Fig. 2.20, respectively. Here, the object distance is set as 10 cm, the used focal length of the Fourier lens is 15 cm.

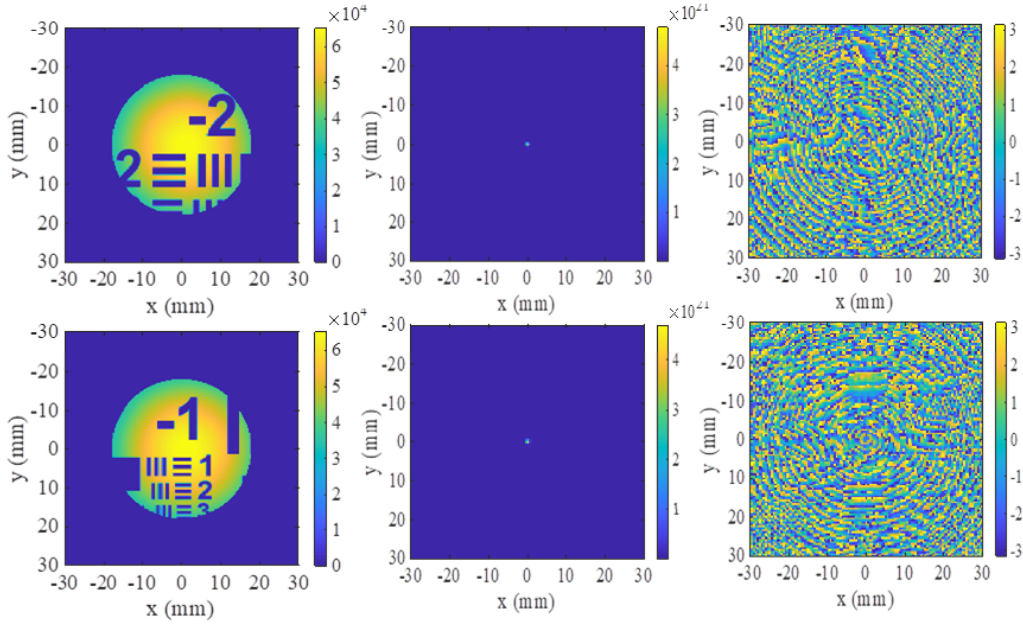


Figure 2.17: Simulation of Fourier spectrum of two different parts of the USAF chart. The plots in the first column are the imaged targets illuminated by the Gaussian beam. The plots in the second column are the intensity Fourier spectrum distributions. The plots in the third column are the Fourier phase distributions.

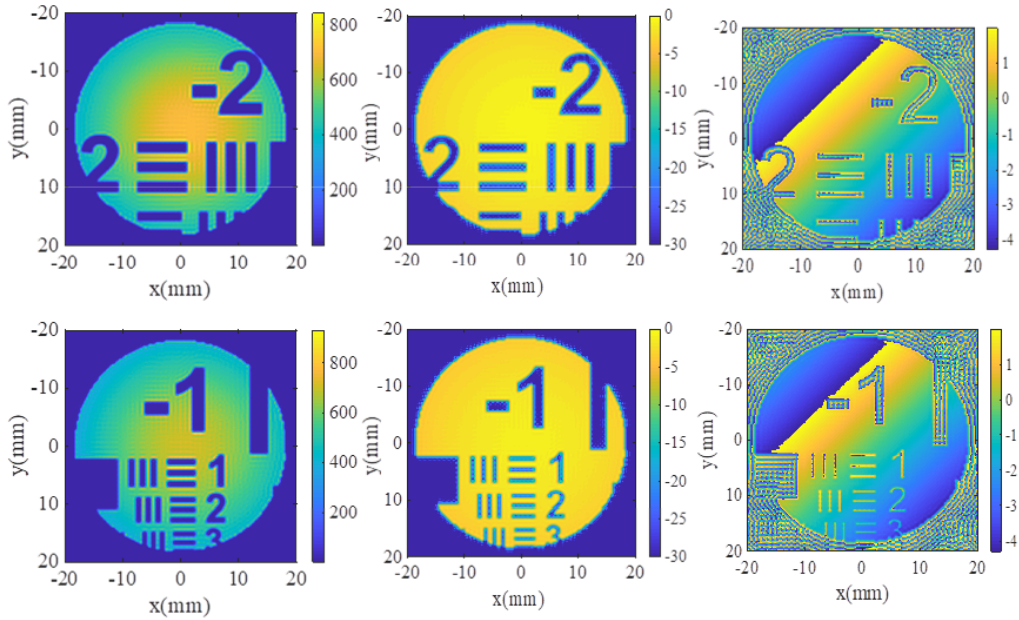


Figure 2.18: The reconstructions of imaged targets in Fig. 2.17. The plots in the first column are the intensity reconstructed images. The plots in the second column are the intensities in the log scale. The plots in the third column are the phase reconstructed images.

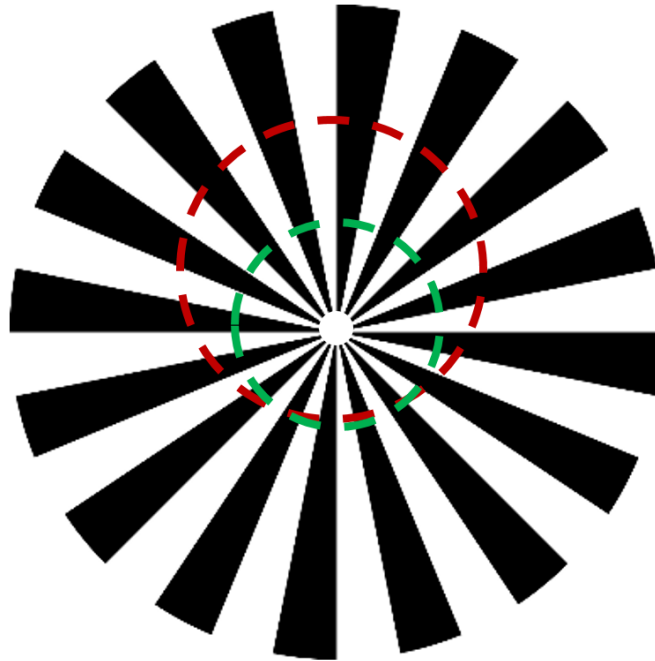


Figure 2.19: Photo of Siemens star test target. The dashed rings circled the areas illuminated by the Gaussian beam.

The reconstructed results from the Fourier spectrum shown in Fig. 2.20 are shown in Fig. 2.21. The left plot is the intensity distribution, the middle plot is the intensity distribution in the log scale, the right plot is the phase distribution.

At 600 GHz, the selected area is focused to the center (as that circled by the green dashed line in Fig. 2.19) to better display the detail structures of the Siemens star. The Gaussian beam size is locked to 4 cm with the same reason demonstrated in the Section of USAF chart simulation. The focal length of the convex lens is 5 cm. The Gaussian beam illuminated image target is the left panel in Fig. 2.22, the corresponding intensity and phase Fourier spectrum can be shown as the middle and the right panels, respectively.

The reconstructed results are displayed in Fig. 2.23. The left figure is the intensity distribution, the middle figure is the intensity distribution in the log scale, the right figure is the phase distribution. The comparison between the 300 GHz and the 600 GHz reconstructed images again shows the imaging resolution principles. It is more obvious in the Siemens star.

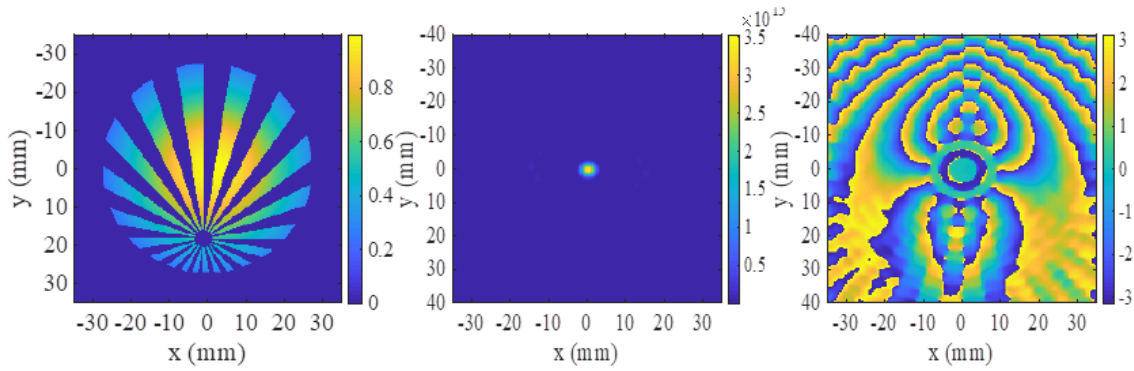


Figure 2.20: Simulation of Fourier spectrum of Siemens star at 300 GHz. The left panel is the image target illuminated by the Gaussian beam. The middle panel is the intensity Fourier spectrum distribution. The right panel is the Fourier phase distribution.

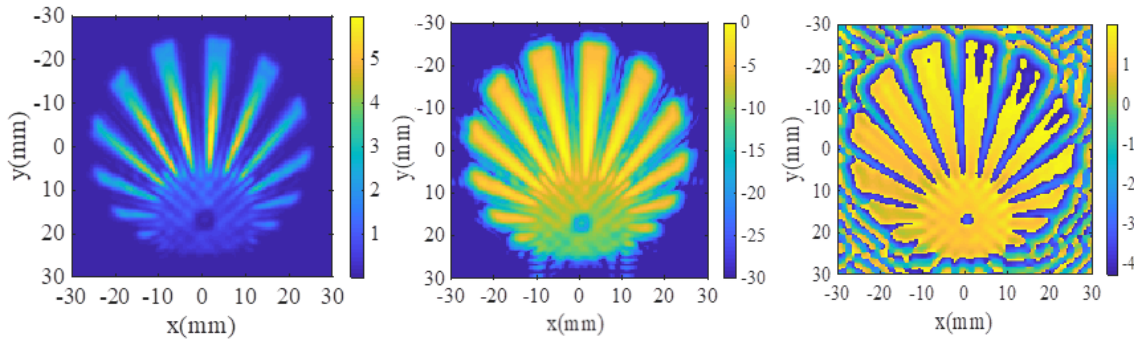


Figure 2.21: The reconstructed imaging results of the Siemens star at 300 GHz. The left plot is the intensity distribution, the middle plot is the intensity distribution in the log scale, the right plot is the phase distribution.

### Simulation of 2D grids

In the last simulation, a 2D periodic grid with a 7.5 cm period in both directions is used as the target. The simulated transmission distribution of the grid is shown in Fig. 2.24, the black part 100% blocks the radiation, the white part presents 100% transmission area. The red and green dashed lines here are used to show the imaging area at 300 GHz and 600 GHz, respectively.

Using the target in the red dashed circle in Fig. 2.24 as the target, projecting a 5.5-cm diameter Gaussian beam composed of 300 GHz radiation, the imaged object can be expressed as the left plot of Fig. 2.25. Following the Fourier transform principles with a 10-cm object distance in front of a 15-cm focal-length Fourier lens, the intensity and

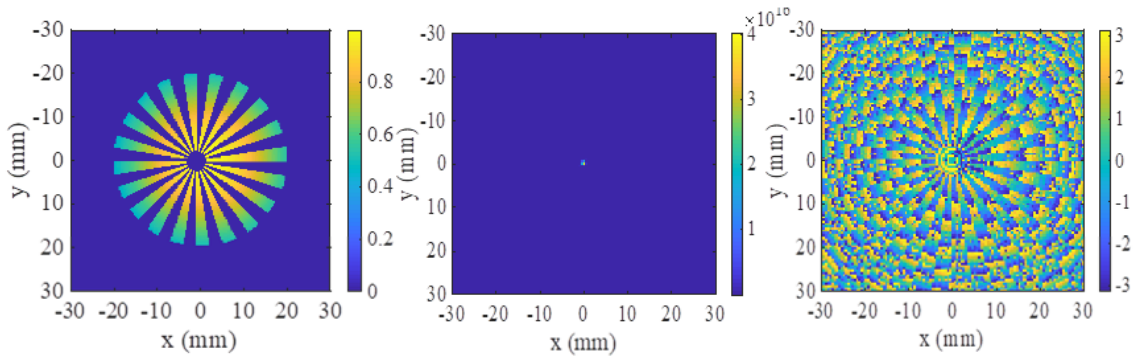


Figure 2.22: Simulation of Fourier spectrum of Siemens star at 600 GHz. The left figure is the image target illuminated by the Gaussian beam. The middle figure is the intensity Fourier spectrum distribution. The right figure is the Fourier phase distribution.

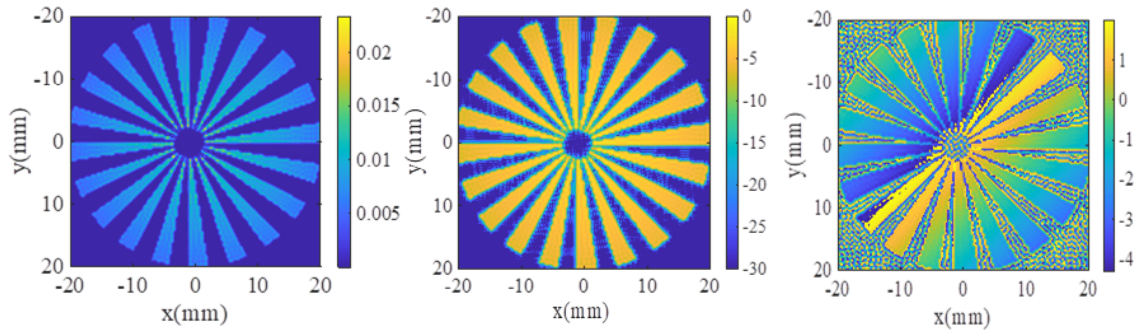


Figure 2.23: The reconstructed imaging results of the Siemens star at 600 GHz. The left figure is the intensity distribution, the middle figure is the intensity distribution in the log scale, the right figure is the phase distribution.

phase Fourier spectrum distribution will be as that shown in the middle and right plots in Fig. 2.25. From the Fourier spectrum, one can see that, both the intensity and the phase are the spread focus spots periodically shifted from the center. The intensity of the focusing spots degrades with the order off the center, while, the phase nearly keeps the same.

The reconstructed images based on the 300-GHz Fourier spectrum can be shown as Fig. 2.26. The left, middle and right graphs display the intensity, log scale intensity and phase images of the rebuilt results, respectively. From the results, one can see, the sharp edge of the corner for each transmitted rectangular is round chamfered because of the resolution limit. The phase looks better visually since it is more sensitive than the

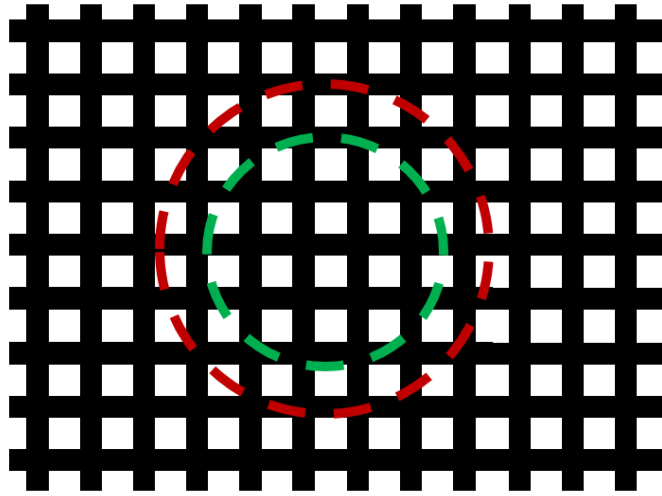


Figure 2.24: Photo of the 2D grid test target. The dashed rings circled the areas illuminated by the Gaussian beam.

intensity.

A smaller illuminated area of the 2D grid with a 4-cm aperture at 600 GHz is shown in the left figure of Fig. 2.27. By applying a 6-cm object distance and 5-cm Fourier focal length, the Fourier spectrum in the middle and right graphs of Fig. 2.27 can be generated. The middle one is the intensity spectrum and the right one is the phase spectrum. Compared with the spectrum at 300 GHz, the period of the focusing points are smaller, the size of each focusing point is smaller. This attributes to the imaging wavelength and the focusing length of the Fourier lens.

The reconstructed images are stated as Fig. 2.28. The left, middle and right panels are the intensity, log scale intensity and phase images, respectively. The imaging results show a sharper edge and corner of the periodic structure than that with 300-GHz radiation, presenting a better resolution.

### 2.3.2 Field of View of Fourier imaging setup

Considering now the images are reconstructed by applying the inverse Fourier transform on the recorded Fourier spectrum. The field-of-view covered by the object reconstruction is given approximately by (derived from the spatial frequency component  $f_{\xi} = \lambda f/x$ ,

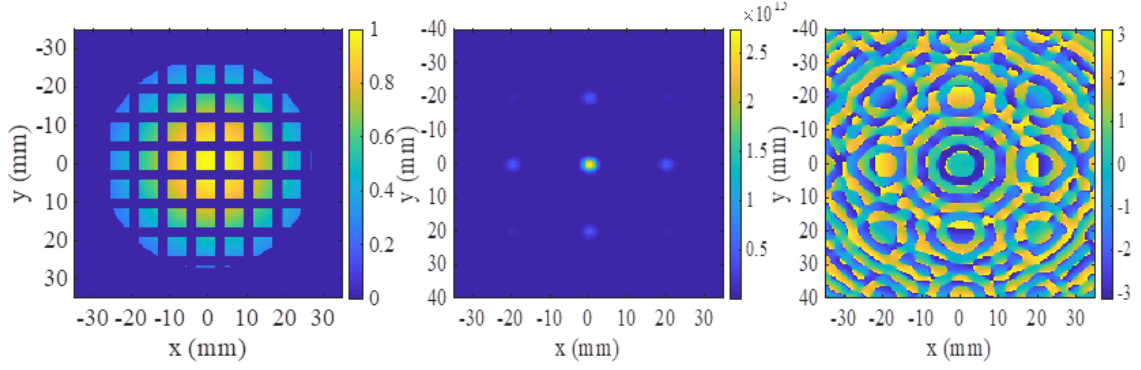


Figure 2.25: Simulation of Fourier spectrum of the 2D grid at 300 GHz. The left graph is the image target illuminated by the Gaussian beam. The middle graph is the intensity of the Fourier spectrum distribution. The right graph is the Fourier phase distribution.

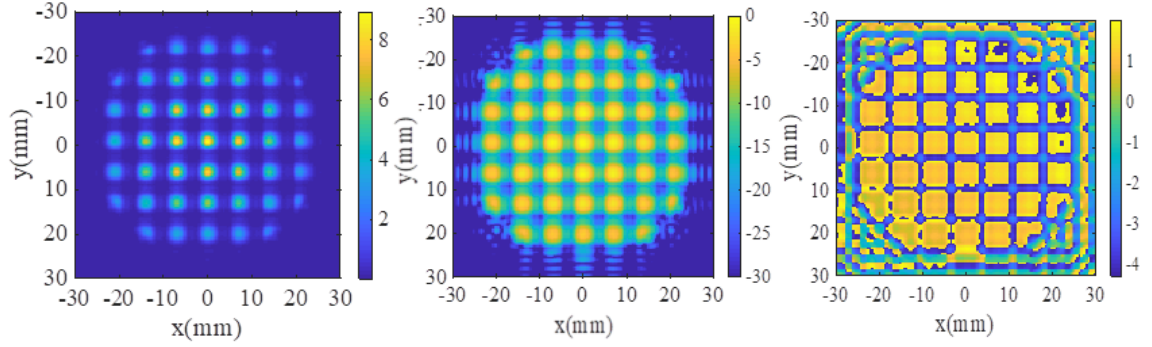


Figure 2.26: The reconstructed imaging results of the 2D grid at 300 GHz. The left panel is the intensity distribution, the middle panel is the intensity distribution in the log scale, the right panel is the phase distribution.

$$f_n = \lambda f / y$$

$$D_{tx} \approx \frac{\lambda f}{\delta x}, D_{ty} \approx \frac{\lambda f}{\delta y}, \quad (2.29)$$

where  $\delta x$ ,  $\delta y$  are the step width of the field scanning in the focal plane. For a 1-mm pixel size in the focal plane and a Fourier focal length of 15 cm at 300 GHz, the inverse transformation to the object plane yields a field-of-view of 15 cm.

Fig. 2.29 is the simulated images of the reconstructed USAF resolution chart under different pixel pitch size and recording area range in the Fourier plane. To have a more direct visual sense, the whole chart is squeezed to  $100 \times 100 \text{ mm}^2$  and used for the simulation at 300 GHz. The object distance is selected as 10 cm, the focal length of the

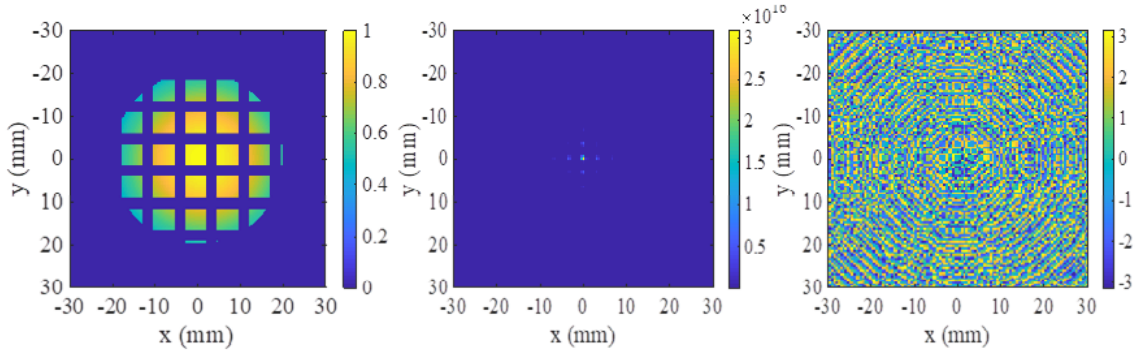


Figure 2.27: Fourier spectrum simulation of the 2D grid at 300 GHz. The left map is the image target illuminated by the Gaussian beam. The middle map is the intensity of the Fourier spectrum distribution. The right map is the Fourier phase distribution.

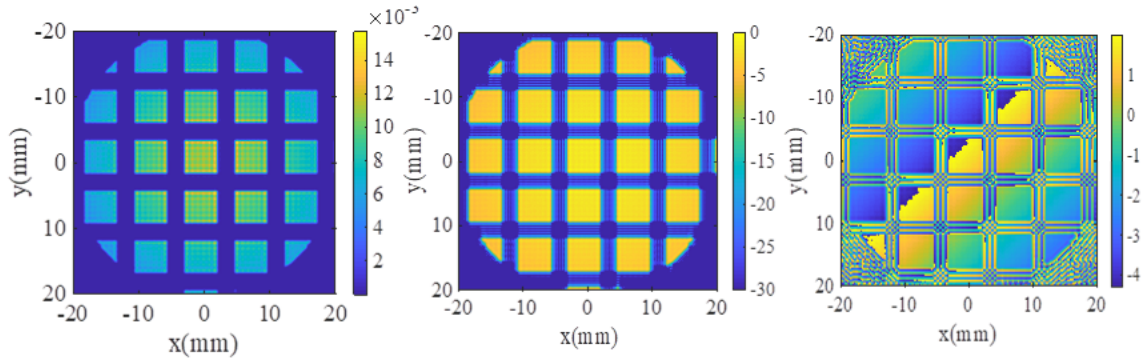


Figure 2.28: The reconstructed imaging results of the 2D grid at 600 GHz. The left plot is the intensity distribution, the middle plot is the intensity distribution in the log scale, the right plot is the phase distribution.

Fourier focusing lens is set for 15 cm. The graphs in the top and bottom rows are the results for  $50 \times 50 \text{ mm}^2$  and  $100 \times 100 \text{ mm}^2$  recorded areas, respectively. The plots in left and right columns are the results for 1-mm and 0.5-mm pixel sizes, correspondingly.

From Fig. 2.29, one will find the field-of-view of the reconstructed image based on the 0.5-mm pixel-size Fourier spectrum ( $100 \times 100 \text{ mm}^2$ ) is 2 times large of that generate based on the 1-mm pixel-size Fourier spectrum ( $50 \times 50 \text{ mm}^2$ ). This validates the mathematical expression in Eq. 2.29. The characteristic allows it to achieve large field-of-view imaging in a specific recording range, as long as the pixel size in the Fourier plane is small enough. This is consistent with what was discussed in Section 2.2.2.

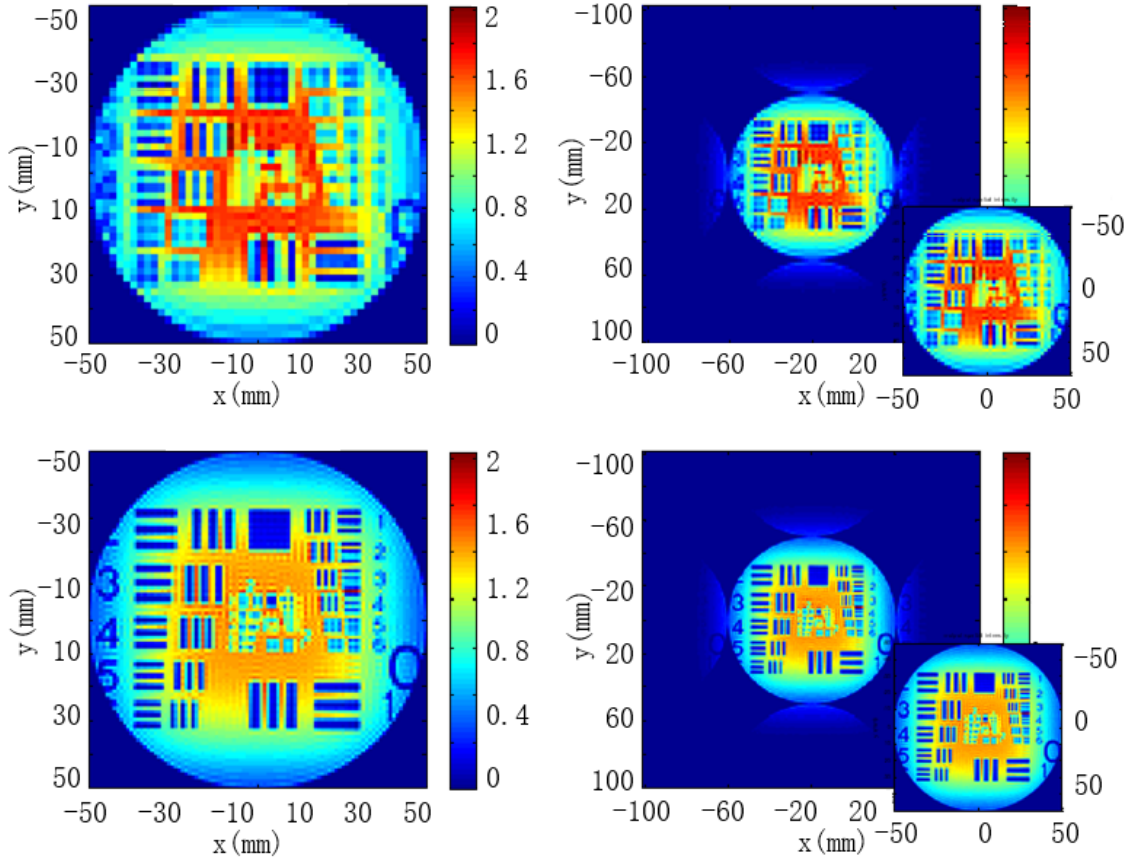


Figure 2.29: The simulation of the USAF resolution chart for different pixel pitch and recording range. The plots in the top and bottom rows are the results for  $50 \times 50 \text{ mm}^2$  and  $100 \times 100 \text{ mm}^2$  recorded areas, respectively. The plots in the left and right columns are the results for 1-mm and 0.5-mm pixel sizes, correspondingly.

### 2.3.3 The primary analysis of Fourier imaging resolution

Owing to the properties of the spatial Fourier transformation, a higher scan resolution in the focal plane results in a larger field-of-view in the object plane. A wider scanning area in the focal plane of the lens, on the other hand, converts to a higher lateral resolution in the object plane. The increased lateral resolution finds its limitation, however, when all wave-vectors permitted by the diffraction limit of the lens (or more generally correct of the entrance pupil of the imaging optics) are covered. The lens induces a soft cut-off for wave-vectors with an absolute value of the lateral component  $k_{||} \geq k_{cut} = k D / \sqrt{D^2 + 4d^2}$ , when  $d \gg D/2$ , we have paraxial approximation  $k_{||} \geq k_{cut} = k D / 2d$  where  $k$  is the

absolute value of the wave-vector,  $d$  is the object distance from the lens, and  $D$  is the diameter of the lens. In order to find the location of the  $k_{cut}$  Fourier representation in the focal plane of the lens, we can use geometrical optical arguments. For a point object at  $d > f$  on the optical axis, the real image is located on the optical axis at the image distance  $b = fd/(d - f)$ . The  $k_{cut}$  Fourier representation is then found in the focal plane at a distance  $|R_{cut}|$  from the optical axis given by

$$|R_{cut}| = \frac{b - f}{b} \frac{D}{2} = \frac{f}{d} \frac{D}{2}. \quad (2.30)$$

If the field map in the Fourier plane extends over a width of more than  $2|R_{cut}|$ , then the resolution, i.e. the smallest resolved distance  $Y_{>}$  in the object plane, is given approximately by

$$Y_{>} = \frac{\lambda d}{D}, \quad (2.31)$$

while for a scan area with a diameter of  $2|R_{max}|$  less than  $2|R_{cut}|$ ,  $D$  must be replaced by an effective lens aperture

$D_{eff} = 2b|R_{max}|/(b - f) = 2|R_{max}|d/f$ , which yields the resolution

$$Y_{<} = \frac{\lambda d}{D_{eff}} = \frac{\lambda f}{2|R_{max}|}. \quad (2.32)$$

These equations are not only applicable for  $d > f$ , but for all values  $d > 0$ .

With Eqn. 2.30, one finds for the simulation as Fig. 2.29 (with  $D = 10$  cm,  $d = 10$  cm,  $f = 15$  cm and  $\lambda = 1$  mm), the  $2|R_{cut}|$  will be 15 cm, which is larger than both recording area range. Thus, the resolution will be defined by Eq. 2.32 with the values of 3 mm and 1.5 mm for the  $50 \times 50$ -mm<sup>2</sup> and  $100 \times 100$ -mm<sup>2</sup> recorded-area cases which is also presented in Fig. 2.29.

## 2.4 Discussion and conclusions

In this chapter, optical analysis in Fourier optics was demonstrated. Based on that, with the use of Fourier transformation, the principle of Fourier imaging is derived by enclosing

the Fourier transform between the imaging targets and the space spectrum into the THz range. The imaging is selected as the physically recorded complex field distribution in the focal plane of the imaging system. After that, the target is reconstructed by numerically applying the inverse Fourier transformation. The simulation of Fourier imaging at both 300 GHz and 600 GHz proves the imaging method to be more robust than conventional methods in a couple of ways. It has a relatively large field-of-view, 3D imaging capability, and compressed sensing possibility, which enables its camera-like professional potential. The simulated Fourier-spectrum generation and the reconstruction of the USAF resolution chart, Siemens star and the 2D grid show that the Fourier spectrum distribution is defined by the imaging wavelength, the object distance and the focal length of the Fourier focusing lens. The imaging field-of-view and resolution can be controlled by choosing a proper pixel size and the recording area range in the Fourier plane, respectively. Although the solution is limited, the fitting camera for the imaging demand is still on the way, the advantages of the Fourier imaging geometry, makes this setup still interesting for potential applications.

## 3 Fourier imaging at 300 GHz

Deep sub-THz radiation (approximately 0.1-0.6 THz) has the advantage of high power and strong penetration capability compared with the higher frequency THz regime. The challenges in this frequency range are the limited pixel numbers in the integration of the detection arrays and the low resolution because of the large wavelength. The demonstrated Fourier imaging technique in this thesis can be utilized to solve these problems since the detection plane is the focal plane where the beam size is the smallest in the system and the resolution can be improved through virtual imaging object distance. In this chapter, the Fourier imaging working at 300 GHz based on heterodyne detection will be presented and analyzed.

### 3.1 Experimental setup of 300-GHz Fourier imaging system

#### 3.1.1 Principle of heterodyne detection

The key idea towards the implementation to Fourier imaging is to record the data in Fourier space coherently. Currently developed coherent imaging with continuous THz waves (CW THz) is mostly based on homodyne detection (i.e. interference, such as holography and phase-shift imaging), frequency-modulated continuous wave (FMCW) methods and heterodyne detection. Considering the advantages with regard to signal to noise ratio, sensitivity and the compactness of the system, the heterodyne detection is adopted here. The following is a brief introduction of the heterodyne detection technique.

Heterodyning is a signal processing technique invented by Canadian inventor-engineer

Reginald Fessenden that creates new frequencies by combining or mixing two frequencies [72, 73]. Heterodyning is used to shift one frequency range into another, and is also involved in the processes of modulation and demodulation [74, 75]. The two frequencies are combined in a nonlinear signal-processing device such as a vacuum tube, transistor, or diode, usually called a mixer [74]. In the most common application, two signals at frequencies  $f_1(\omega_1)$  and  $f_2(\omega_2)$  are mixed, creating two main new signals, one at the sum  $f_1 + f_2$  of the two frequencies, and the other at the difference  $f_1 - f_2$  [73] (higher order sum and differential frequencies will be discussed in later chapters). These frequencies are called heterodynes. Typically only one of the new frequencies is desired, and the other signal is filtered out from the mixer's output. Heterodyne frequencies are related to the phenomenon of "beats" in acoustics.[74, 76]

The intensity of the output signal generated by nonlinear mixing of input signal  $E_1 = E_{in} \cos(\omega_1 t + \phi_1)$  and the reference signal (also called local oscillator)  $E_2 = E_{lo} \cos(\omega_2 t + \phi_2)$  can be expressed as

$$\begin{aligned}
 I &= [E_1 + E_2]^2 \\
 &\propto E_{in}^2 + E_{lo}^2 \\
 &\quad + E_{in}E_{lo} \cos[(\omega_1 + \omega_2)t + (\phi_1 + \phi_2)] \\
 &\quad + E_{in}E_{lo} \cos[(\omega_1 - \omega_2)t + (\phi_1 - \phi_2)].
 \end{aligned} \tag{3.1}$$

Similar to the optical range, at THz frequencies the lower frequency component which can be handled electrically is usually filtered for demodulation.

### 3.1.2 300-GHz Fourier imaging setup based on heterodyne detection

We investigate THz Fourier imaging experimentally at 300 GHz. A single-pixel TeraFET detector operated in heterodyne mode [77–81] is raster-scanned across the focal plane of an imaging lens and records amplitude and phase of the radiation arriving from the scene under investigation. The complex-valued focal-plane field map then allows the

reconstruction of the object with an inverse Fourier transform method. This method is different from single-pixel imaging where a power detector is located at a fixed position and time-varied intensity or phase patterns are projected onto it [82–84].

The measurement set-up is displayed in Fig. 3.1. For object illumination, an electrical multiplier-chain source (S1, vendor: Virginia Diodes Inc., base frequency of 16.66 GHz generated by a HP synthesizer, frequency multiplication factor:  $18\times$ , output power: 1 mW) whose continuous-wave radiation leaves the horn antenna with a  $20^\circ$  divergence angle is selected. The radiation is collimated with a 3-inch-diameter aspherical teflon lens (L1, from Thorlabs Inc.,  $f=15$  cm). The resultant beam diameter is about 5.5 cm. Another 3-inch teflon lens (L2, same parameters as L1) focuses the transmitted radiation onto a TeraFET detector [85, 86] consisting of a Si CMOS field-effect transistor with a monolithically integrated dipole antenna. The numerical aperture (NA) of the system is also equal to the lens's NA with the value of 0.254. The radiation is coupled into the TeraFET through its weakly doped substrate which is attached with a silicon substrate lens [87, 88] (diameter: 4 mm). A second multiplier-chain source (S2, vendor: RPG-Radiometer Physics GmbH, base frequency of 16.66 GHz + 1 kHz generated by a second HP synthesizer, frequency multiplication factor:  $18\times$ , output power:  $432\ \mu\text{W}$ ) serves as local oscillator, its radiation is focused with a third teflon lens (L3,  $f=10$  cm) from the front side onto the active region of the TeraFET. The difference-frequency signal from the TeraFET is then integrated in a lock-in amplifier (Perkin Elmer, integration time: 50 ms, providing a dynamic range of 60 dB) whose reference signal at 1 kHz is obtained by mixing the drive signals from the two synthesizers in an MARKI electrical mixer. The lock-in amplifier works at the 18th harmonic of the reference signal.

The detector together with lens L3 and the radiation source S2 is mounted on a translation stage which allows to perform raster-scan imaging of the amplitude and phase of the radiation field across the focal plane ( $xy$ -plane) of lens L2. The step width is 1 mm in both the  $x$ - and  $y$ -direction. The scans cover an area of  $80\times 80\ \text{mm}^2$ , the total data recording time is 30 min (single scan).

A major challenge with these measurements has been the long coherence length of the radiation resulting from the narrow bandwidth of the radiation of 1 MHz which leads to



interpreted as the Fourier transform of the complex transmission function  $T(X, Y)$  in an object plane at a distance  $d$  in front of L2. In order to reconstruct the transmission function from the complex-valued focal-plane field map, a MATLAB routine that utilizes the inverse 2D FFT to calculate the light field at any given distance  $d$  in front of the focusing lens (taking a deliberate tilt of the object into account, see above) has been implemented. The routine returns the relative amplitude and the phase of the scattered target wavefront. In order to smoothen the reconstructed image, the field-map area is expanded by a factor of two by padding zeros [89] around the raw data. An example of a reconstruction is given in Fig. 3.2. It shows a metal grid consisting of 2.5-mm-wide aluminum stripes with a spatial period of 7.5 mm, the recorded amplitude and phase maps, and the reconstructed amplitude and phase at the object plane. The grid is well resolved although the stripe width is close to the resolution limit of 1.875 mm calculated by Eq. 2.32.

#### 3.1.3 Image reconstruction

The distribution of the electric field coming from the scene and arriving in the focal plane of lens L2 is described by Eq.2.25. The integral contained therein can be interpreted as the Fourier transform of the complex transmission function  $T(\xi, \eta)$  in an object plane at a distance  $d$  in front of L2.

The reconstruction routine includes a data preprocessing with the purpose of decoding the object distance  $d$  by dividing the quadratic phase factor. At the end, the routine returns the relative amplitude and the phase of the scattered target wave front. In order to decrease the pixel size in the reconstruction image and show more detailed information, the field-map area is expanded by a factor of two by padding zeros [89] around the raw data.

## 3.2 Imaging results of 300-GHz Fourier imaging system

Based on the experimental setup described in Section 3.1.2, both the 2D imaging results and 3D imaging results are recorded. The practical lateral and axial resolution of the imaging system thus can be extracted from the imaging results.

### 3.2.1 Imaging results of different sample

To demonstrate the 2D imaging capability, a thin metal grid and a PCB board taped with the USAF chart are utilized as the samples. In a first experiment, a planar object hidden between sheets of plastic foam, which is opaque in the visible but transparent at terahertz frequencies, is demonstrated to be detected with good spatial resolution using Fourier imaging. For this measurement, a metal grid consisting of 2.5-mm-wide aluminum stripes with a spatial period of 7.5 mm, is embedded between two 2-cm-thick layers of polyurethane foam and placed into the collimated illumination beam 10 cm in front of the lens L2. Fig. 3.2 shows the photo of the metal grid, recorded amplitude and phase maps, and the reconstructed amplitude and phase at the object plane. The recorded data and the reconstructed results show a good agreement with the 300-GHz simulation of the 2D grid target in Fig. 2.25 and 2.26 of Section 2.3.1. The grid is well resolved although the stripe width is close to the resolution limit (demonstrated in Chapter 5).

In the second experiment, a USAF 1951 resolution test chart, imprinted in the metal of a printed circuit board, is selected and again embedded between two 2-cm-thick layers of polyurethane foam and placed into the collimated illumination beam 10 cm in front of the lens L2. Fig. 3.3 shows three segments of the chart of which images are taken and the three reconstructed intensity images. They are corrected for the Gaussian intensity profile of the beam measured previously. Given the width of the metal structures (the minus sign of number 3 as well as the stripes in front of number 1 have a width of 2 mm, while that of numbers 1, 4, 5, and 6 is less than 1 mm), one determines the resolution to be on the order of 2 mm. Here, only the reconstructed images are presented. The recorded

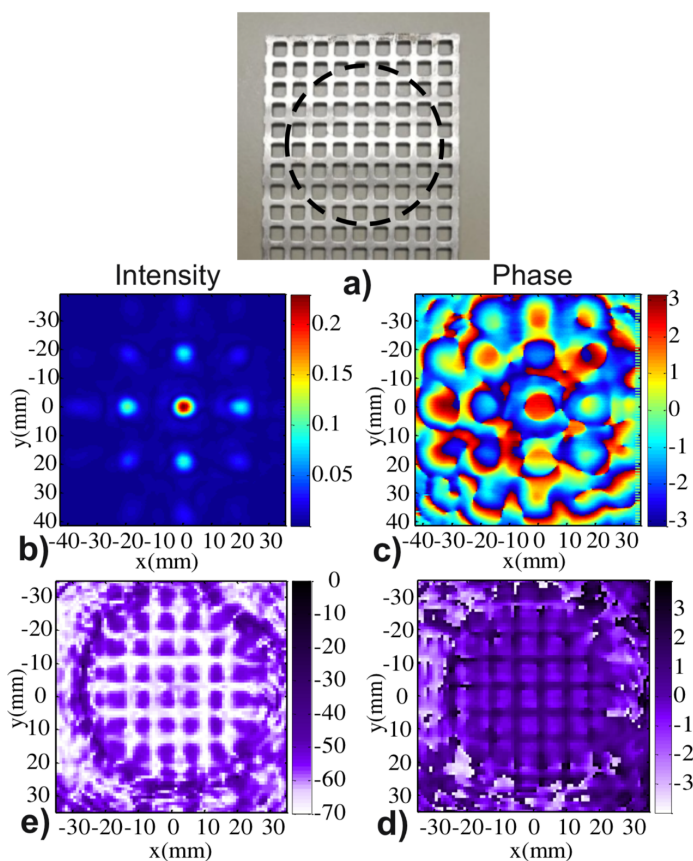


Figure 3.2: (a) Photograph of the aluminum grid. (b) The measured intensity and (c) phase in the Fourier plane (raw data, not corrected for the intensity profile of the illumination). Lower row: Reconstructed intensity in dB units (d) and phase (e) in the object plane. The intensity data are corrected for the Gaussian intensity profile of the illumination beam. The color bar of the phase images gives the phase in units of rad.

Fourier spectrum can be found in Appendix A.1. The results show a good consistency with the simulation results in Fig. 2.16 (since the experimental USAF chart target is a special customized, Fig. 3.3) has an additional number -3 compared with the simulation in Fig. 2.16).

With Eq. 2.30 and 2.32, one finds that the system (with  $D = 7.6$  cm,  $f = 15$  cm and  $\lambda = 1$  mm), for a typical object distance  $d = 10$  cm, will generate a value of  $2|y_{cut}|$  with 11.4 cm. The lens-passed Fourier components hence span a rather large area in the focal plane. The quadratic scan area in the focal plane is  $8.0 \times 8.0$  cm<sup>2</sup>. Approximating it by a circular area with a diameter of  $2|y_{max}| = 8.0$  cm, one finds  $|y_{max}| < |y_{cut}|$ . The resolution is hence to be estimated with Eq. 2.32 which gives a value of  $Y_{<} = 1.875$  mm,

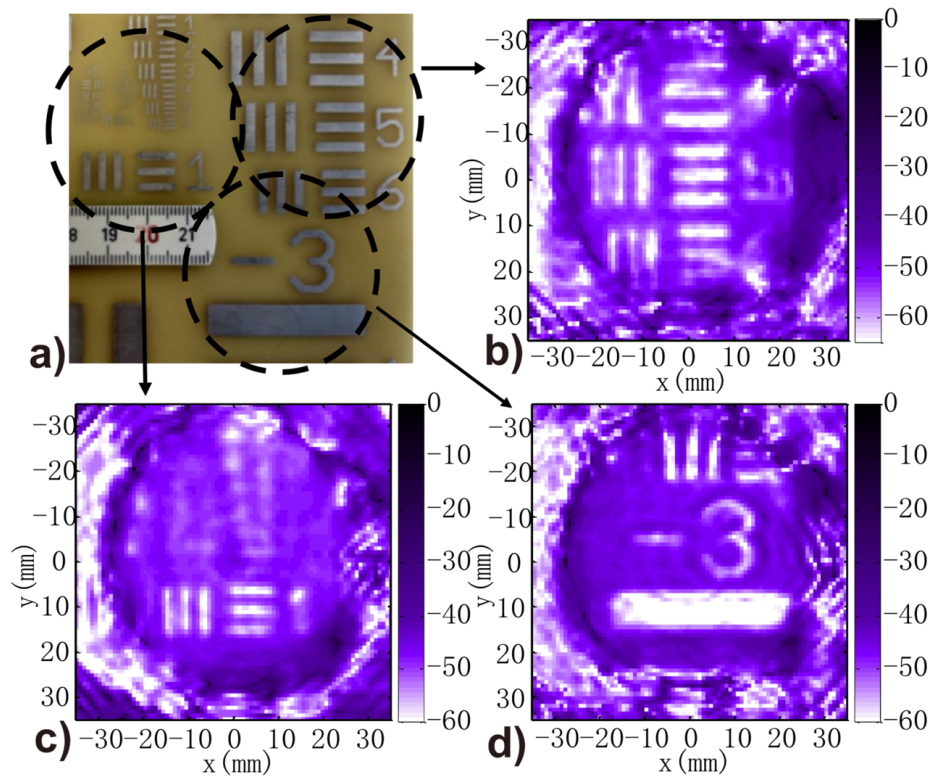


Figure 3.3: (a) Photograph of imaged segment of a USAF chart. The three dashed circles mark the regions for which the three intensity image reconstructions are displayed. (b), (c), and (d) Reconstructed intensity images for different regions in a). Here and in all other intensity images exhibited in this paper, the colorbar is in units of dB.

i.e., the smallest measurable distance between neighboring points in the object plane, expected for our experimental parameters. The 2-mm resolution estimated above from the experimental data is indeed close to the theoretical resolution value of 1.875 mm.

### 3.2.2 Imaging results for different image distances

With Eq. 2.27, one will find the object distance  $d$  is encoded in the phase factor  $g(x, y)$  of the recorded data. The reconstruction relies on numerical refocusing. This section will investigate numerical refocusing during image reconstruction and the effect of the variation of the assumed object distance onto the lateral spatial resolution. The object-under-test is the Siemens star shown in Fig. 3.4a. The area within the dashed circle is the imaged region (whose size is determined by the optical system). The center of the

Siemens star has been shifted a little bit off the optical axis in order to cover a region of the star with a strong variation of the pattern size. Fig. 3.4b displays an intensity image taken in the conventional way of a  $4f$ -setup (object and image distance equal to  $2f$ ) based on the same collimated illuminating beam and using the same focusing lens L2 of the Fourier imaging system. The image has been corrected for the Gaussian intensity profile of the collimated illumination (measured without the object in the beam path). The circular structures (blotchy white rings) in the figure come from the diffraction at the edge of the collimation lens. Fig. 3.5 shows a series of reconstructed images obtained with the Fourier method. With Eq. (D1) given in Ref. [47], one calculates that the expected depth resolution of our experiment is 0.7 cm (assuming the values  $2|y_{max}| = 80$  mm,  $f = 15$  cm, and  $\lambda = 1$  mm, see Ref. [47] Appendix D for details). Based on this expected resolution, the Siemens star has been placed at different distances  $d$  from the lens L2 ranging from 9 cm to 12 cm in 1-cm steps. For each of the Fourier maps, we then assume these four values of  $d$  also for the reconstruction. This yields the matrix plot of Fig. 3.5 where the variation of the object position occurs along the columns and that of the recovery distance along the rows. Object and recovery distances coincide along the diagonal of the matrix plot. Similar to physical defocusing, an unblurred image is obtained only in this case, and the image quality degrades, if the recovery distance deviates from the object distance.

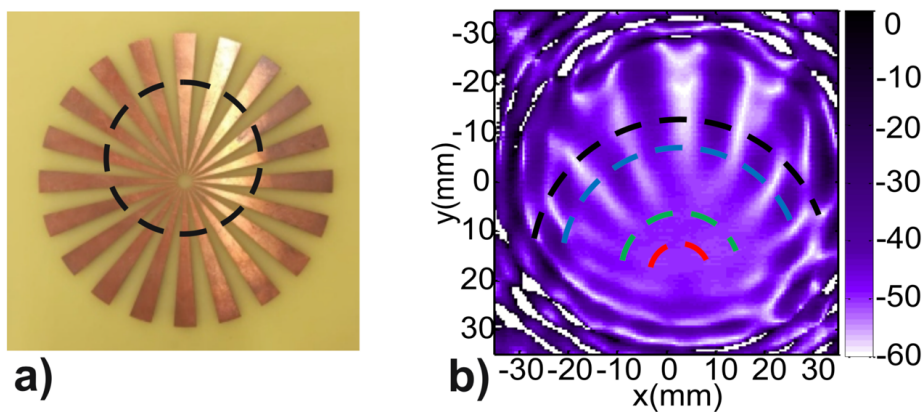


Figure 3.4: (a) Photograph of the Siemens star (copper on plastic substrate). (b) Intensity image recorded in the conventional way in a  $4f$ -arrangement. The colored circle segments indicate the paths of the line scans of Fig. 3.6.

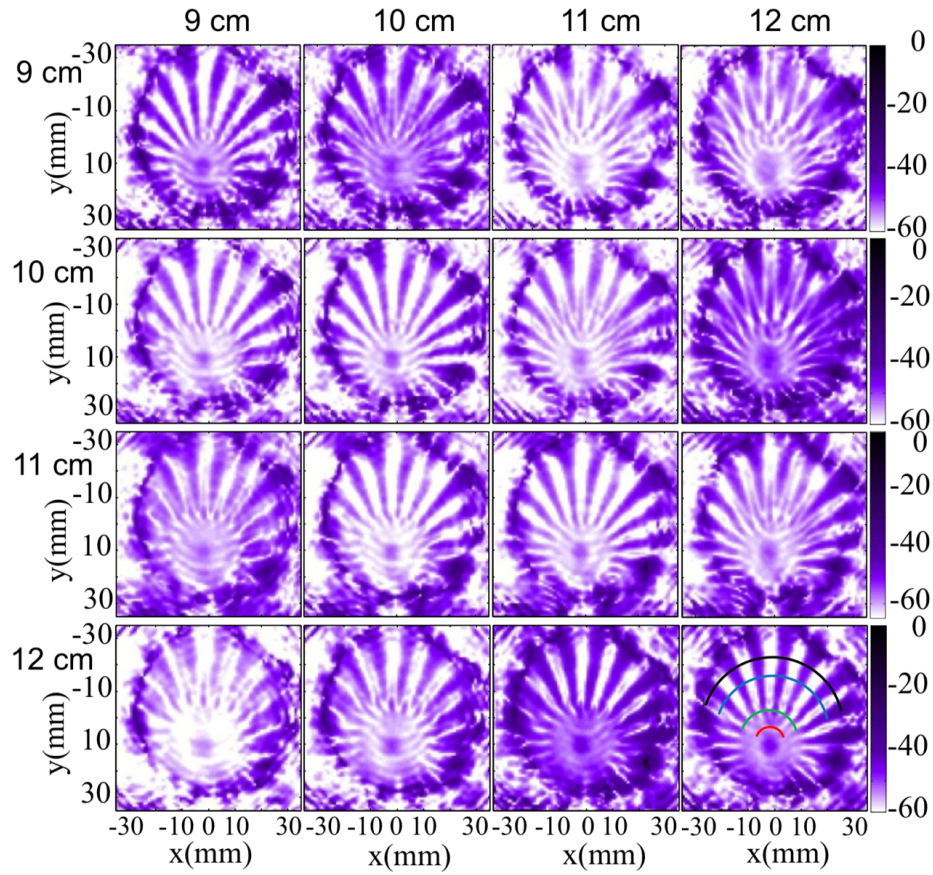


Figure 3.5: Reconstructed intensity images of the Siemens star for different object distances (varied along the columns) and recovery distance (varied along the rows). The colored arcs inserted into the image at the bottom right indicate the positions of the line scans of Fig. 3.6.

Fig. 3.6 compares the lateral spatial resolution achieved by conventional  $4f$ -imaging with that of the object reconstruction by Fourier imaging. The comparison is performed with the help of circular line scans in the respective intensity images of Fig. 3.4b and the bottom right of Fig. 3.5. The circles have radii of 6.4 mm, 12.7 mm, 25.5 mm, and 31.8 mm, corresponding to a local width of the triangular metal patches of the Siemens star of 1 mm, 2 mm, 4 mm, and 5 mm (each patch covers a central angle of  $9^\circ$ ). The position of each arc is marked by a dashed or solid red, green, blue, or black line in Fig. 3.4b and the bottom right of Fig. 3.5, dashed lines for the conventional image and solid lines for the Fourier reconstruction. Considering first the conventional image, one finds that the line scans along the two arcs with the smallest radii show hardly any modulation, while a modulation is visible for the other two line scans. The bright-dark pattern of

the metal-dielectric sequence is not fully resolved in any line scan. From these findings, one estimates that the spatial resolution is about 4 mm. Using the knife-edge method, one also finds a resolution of about 4 mm, which is in agreement with the 3.95-mm resolution calculated for the  $4f$ -geometry (see Appendix B in Ref. [47]) with a 3-in. focusing lens aperture and a 15-cm focal length at 300 GHz. In contrast, the line scans of the reconstructed Fourier image exhibit a more pronounced modulation, even revealing sharp dark-bright modulation for the two arcs with the smallest radii. These observations suggest a resolution on the order of 2 mm, which is in good agreement with the calculated resolution of 1.875 mm.

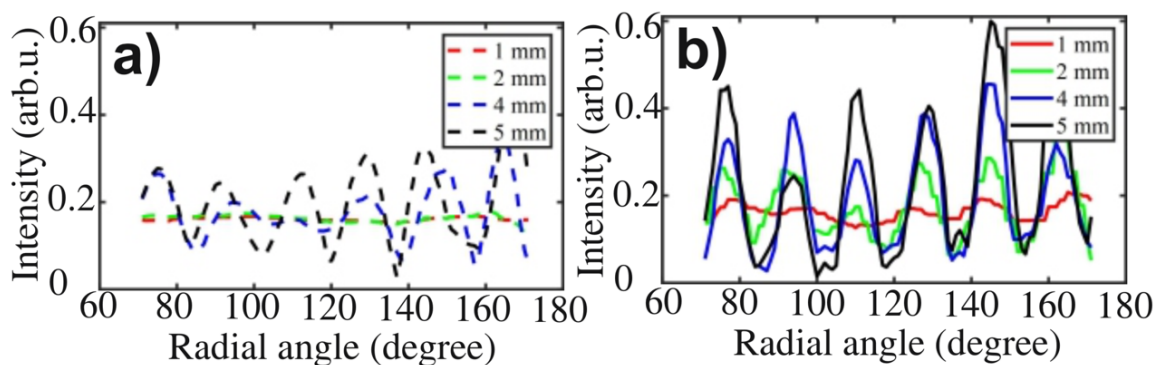


Figure 3.6: Scans along the circular lines shown in the intensity images of Fig. 3.4(b) and the bottom right of Fig. 3.5. (a) Line scans taken in the conventional image, and (b) those taken in the reconstructed Fourier image. The legend lists the local width of the metal segments of the Siemens star ranging from 1 mm to 5 mm, the centers of the circles are located in the centers of the Siemens star images.

For the chosen parameters, the Fourier imaging system achieves a resolution more than twice better than the  $4f$ -imaging system built with the same imaging source and imaging lens and using the same data recording area (in one case in the image plane and in the other in the focal plane). The better resolution of the Fourier image is entirely a consequence of the fact that the object has been placed closer to the lens. In fact, we have chosen  $d < f$ , which for conventional imaging implies the generation of a virtual image where direct image recording with a sensor matrix is not possible anymore. Conventional imaging reaches maximal resolution for  $d = f$ . With Fourier imaging, using the same lens, an improved resolution beyond this limit is possible.

### 3.2.3 Imaging results of obstacle objects

In a last experiment, the capability of Fourier imaging to allow detection of objects in the line-of-sight of other ones by numerical focusing is demonstrated. This is achieved since the edge of the objects can provide enough scattered radiation to reach the detector. A steel screw is placed at  $d = 18\text{cm}$  in front of the lens L2 and a steel washer at  $d = 16\text{cm}$ . The objects are held in place in the beam path by polyurethane foam, which they have been pressed into. The washer blocks the line-of-sight of the screw toward the lens in the direction parallel to the optical axis of the imaging system. This arrangement is indicated in Fig. 3.7a. The intensity and phase images of the washer and the screw recovered from a single frame recorded in the focal plane of lens L2 are shown in Figs. 3.7b–e. Since the washer and the screw are opaque to terahertz waves, traditional imaging would hardly allow us to identify the screw behind the washer. However, the complex-valued field map of the focal plane contains enough scattered and phase-encoded distance information that it is possible to extract the information about the screw's contour upon numerical focusing into the plane where it is located. The ability to distinguish the two objects vanishes as the objects are moved closer together, and less scattered light passing around the washer or through its hole is collected by the lens L2 and reaches the detector.

## 3.3 Discussion and comparison

This chapter further discussed the advantages and challenges brought about by the coherent field detection in the focal plane of a lens. The capability of Fourier imaging to enable a better spatial resolution than conventional imaging with a given lens is stressed because it is possible to place the object closer to the lens, at a position between the lens and focal point where conventional imaging generates virtual images. This does not affect the image reconstruction capability of Fourier imaging, which then benefits at closer distance to the lens from the reduced lens-aperture-induced obstruction of the k-space components of the radiation coming from the object.

The strength of Fourier imaging to recover 3D space information by sequential object-plane reconstruction via the variation of the distance  $d$  in the back-transformation process

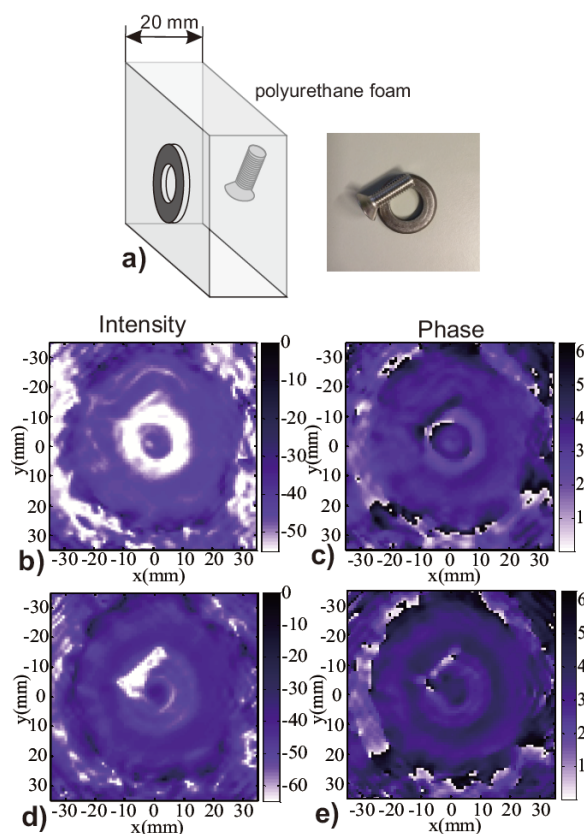


Figure 3.7: Washer-and-screw scene sketched in (a) where the objects are held in place by a hard foam material into which they have been pressed. The washer obscures the line-of-sight of the screw. Middle panels: Intensity (b) and phase images (c) for a reconstruction distance equal to the position of the washer; lower two panels: reconstructed intensity (d) and phase (e), but for the distance equal to that of the screw.

is emphasized. While this capability is intrinsic to all coherent imaging techniques, Fourier imaging owing to the focusing effect of the lens has the advantage that the beam area to be covered is smallest. Thus, it lends itself to the use of heterodyne focal plane arrays. This can be especially beneficial for the terahertz frequency regime given the practical restrictions for detector arrays arising from the large wavelength of the radiation. The heterodyne operation can be achieved in a subharmonic manner [90], thus alleviating the costs for a second high-frequency radiation source. A specific benefit arising from the capability of numerical focusing is that two opaque targets, although they are in each other's beam path, can be distinguished from each other using the field map of a single focal-plane frame. The requirement is to have enough light intensity available

at the detector from each object. This object distinction as well as most other aspects of Fourier imaging depends critically on the avoidance of detrimental standing waves, which arise if the coherence length of the radiation is too large. These standing waves usually cannot be taken into account properly in the back-transformation process, even after careful calibration of the illumination beam prior to the imaging process, because the objects to be studied are not known well enough to account for the change in the field distribution caused by them.

# 4 Fourier imaging based on sub-harmonic heterodyne detection at 600 GHz

In the far-field imaging system, the minimum recognizable distance (i.e. the resolution) is proportional to the imaging radiation wavelength according to the diffraction criterion. Therefore, to improve the imaging resolution, the most simple and effective way is to use short-wavelength radiation. However, at THz frequencies, the device/transceiver's price increases with the rising frequency whilst the output power decreases extremely fast. Considering the cost-effectiveness, the sub-harmonic detection schematic using 600-GHz waves as radiation and 300-GHz waves as LO signal will be demonstrated in this chapter. In order to enhance the sensitivity, the innovative structure that mounting a two-stage wax/PTFE lens on the front of the detector is first proposed. Benefiting from the enhanced detector sensitivity, the dynamic range and the imaging resolution of the imaging system is improved.

## 4.1 Fourier imaging based on sub-harmonic heterodyne detection

### 4.1.1 Sub-harmonic heterodyne detection

Fundamental heterodyne detection (FHD) loses its appeal at high sub-THz frequencies, because power availability becomes more and more limited with rising frequency [90].

Sub-harmonic mixing is a substitute choice in this case, since the LO frequency can be a fraction (plus a frequency offset) of the signal frequency rather than nearly same with each other in FHD. The lower LO frequency allows it to be all-electronic component with readily high power, strong coherence and comparable low price.

Both fundamental and sub-harmonic heterodyne detection (SHHD) relies on the nonlinear mixing of the detected signal (indicated by RF here) and the LO signal based on the detector. A new intermediate frequency (IF, differential frequency of the RF and the LO signals) signal which carries on the target response information could be extracted and analysed. The accurate model of the nonlinear characters of the TeraFET detector is based on the antenna design, the antenna-transistor resistance matching and the structure of the transistor, which has different models when using different processing technology and is difficult to estimate. Here the analysis will be purely explored by the polynomial expansion of the current-voltage response which is a general approach. The equation can be written as

$$I(V) = b_0 + b_1V + b_2V^2 + b_3V^3 + b_4V^4 + \dots, \quad (4.1)$$

where  $b_i$  ( $i = 1, 2, 3, \dots$ ) is the coefficient of different order items. Defining the detected signal as  $V_{i1} = V_{RF} \cos(\omega_{RF}t + \phi_{RF})$  and the LO signal as  $V_{i2} = V_{LO} \cos(\omega_{LO}t + \phi_{LO})$  and substituting  $V = V_{i1} + V_{i2}$  into Eq. 4.1, one will get

$$I_{res} = k_{mn} \sum_{m=-\infty}^{\infty} \sum_{n=-\infty}^{\infty} \cos(|m\omega_{RF} + n\omega_{LO}| + m\phi_{RF} + n\phi_{LO}), \quad (4.2)$$

$k_{mn}$  is the coefficient of each frequency. Omitting the 4th and higher order components in Eq. 4.1,  $k_{mn}$  can be expressed as

$$\begin{aligned} k_{00} &= b_0 + \frac{b_2}{2}(V_{RF}^2 + V_{LO}^2), \\ k_{10} &= b_1V_{RF} + \frac{3b_3}{4}V_{RF}^3 + \frac{9b_3}{4}V_{RF}V_{LO}^2, \\ k_{01} &= b_1V_{LO} + \frac{3b_3}{4}V_{LO}^3 + \frac{9b_3}{4}V_{RF}^2V_{LO}, \\ k_{11} &= b_2V_{RF}V_{LO}, \\ k_{20} &= \frac{b_2}{2}V_{RF}^2, \\ k_{02} &= \frac{b_2}{2}V_{LO}^2, \end{aligned}$$

$$k_{21} = \frac{3b_3}{4} V_{RF}^2 V_{LO}.$$

$$k_{12} = \frac{3b_3}{4} V_{RF} V_{LO}^2.$$

$$k_{30} = k_{03} = \frac{3b_3}{4} V_{RF}^3,$$

$$k_{03} = k_{30} = \frac{3b_3}{4} V_{LO}^3.$$

One can find that apart from the initial frequencies of  $f_{RF}$  ( $f_{RF} = \omega_{RF}/2\pi$ ) and  $f_{LO}$  ( $f_{LO} = \omega_{LO}/2\pi$ ), new signal components with frequencies of  $|mf_{RF} + nf_{LO}|$ , ( $m, n = \dots 1, 2, 3 \dots$ ) appear in the response current. Heterodyne detection filters the differential term with  $m = 1$ , thus the down-mixing IF frequency  $f_{IF} = |f_{RF} - nf_{LO}|$ , ( $n = 1, 2, 3 \dots$ ) shifts THz waves detection to lower frequency band where the high-performance microwave devices such as LNAs (low noise amplifier), filter and other components are easy to access. When  $n = 1$ , the mixing is FHD. If  $n \geq 2$ , the mixing is n-th sub-harmonic heterodyne detection. The coefficient of n-th sub-harmonic IF signal is

$$k_n = \frac{V_{RF} V_{LO}^{*n}}{2^n n!} \cdot \frac{\partial^{n+1} I_{res}}{\partial V^{n+1}}, \quad (4.3)$$

For the 2rd SHHD, the IF signal will be

$$I_{IF} \approx \frac{3b_3}{4} V_{RF} V_{LO}^2 \cos((\omega_{RF} - 2\omega_{LO})t + \phi_{RF}). \quad (4.4)$$

This calculation is derived from Eq. 4.1 omitting the 4th and higher order components which has a trivial contribution. Using the lock-in amplifier with the reference of  $f_{IF-sub} = |f_{RF} - 2f_{LO}|$  to analyse the IF signal, both the intensity and the phase of the detected signal will be resolved.

Considering from the detector factors, the output current is related to the coefficient  $b_3$  in Eq. 4.1, which is usually smaller than the FHD coefficient  $b_2$ . Taking  $V_{LO}$  into consideration, one can find the response of 2rd SHHD is proportional to  $V_{LO}^2$  and FHD is proportional to  $V_{LO}$ . Based on this knowledge, the intrinsic lower small-signal conversion efficiency of 2rd SHHD compared with heterodyne mixing at the fundamental driven by the detector can be compensated by applying a strong LO radiation. However, in practice, both the power of the radiation and the responsivity of the TeraFET detector at sub THz frequencies are not adequate to supply enough  $V_{LO}$ . The integration of the two-stage

wax/PTFE lens on TeraFET detector can solve this problem by improving the coupling efficiency of the LO radiation.

#### 4.1.2 Characteristics of sub-harmonic detection at THz range

To have a basic knowledge of the detector, first, the calibration of the detector work in the direct detection mode (intensity detection) will be presented. The conventional incoherent direct detection scheme is shown in Fig. 4.1a [91]. If an input signal  $V_{RF} \cos(\omega_{RF}t + \phi_{RF})$  is applied, the produced DC output will be  $a_2 V_{RF}^2/2$ , where  $a_2$  is determined by the nonlinear device. To alleviate the impact of the device flicker noise, the output signal is chopped. As a result, the output signal (fundamental tone of the square wave after chopping) is

$$V_{chopp}(t) = \frac{1}{\pi} a_2 V_{RF}^2 \cos(\omega_{chopp}t), \quad (4.5)$$

in which  $\omega_{chopp}$  is the chopping angular frequency. This signal is load to a lock in for filtering and readout.

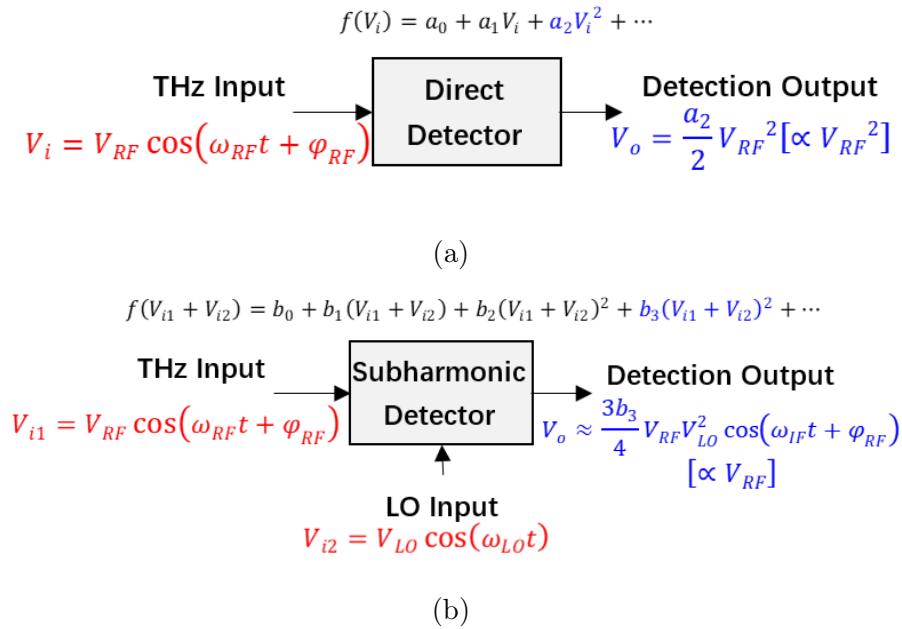


Figure 4.1: Response of (a) direct detection and (b) sub-harmonic detection.

Eq. 4.5 shows us that the output is proportional to the received power. Thus, the

corresponding NEP (noise-equivalent power) can be calculated as

$$NEP = \frac{\sqrt{4k_B T R}}{V_{res}/P}, \quad (4.6)$$

where  $k_B = 1.3806 \times 10^{-23} J/K$  is the Boltzmann constant,  $T$  is the temperature,  $R$  is the effective resistance of the detector and  $V_{res}$  is the voltage response of the detector under the illuminating power  $P$ .

A broadband CMOS FET based bow-tie antenna is captured as a detector for the heterodyne mixing in the experiment. For each gate voltage, the corresponding DC resistance can be derived from the output current versus input voltage (I-V) curve of a detector. In Fig. 4.2(a), the I-V curve of a bowtie antenna integrated CMOS FET detector is presented. The corresponding DC resistance is depicted in Fig. 4.2(b) with black circle line. The direct response of the detector at both 300 GHz (VDI  $18\times$  multiplier chain with  $600\text{-}\mu W$  output power) and 600 GHz (RPG  $36\times$  multiplier chain with  $56\text{-}\mu W$  power) versus the gate voltage are depicted in Fig. 4.3(a), and the NEP can be calculated as Fig. 4.3(b). Here, the detectors are integrated with a 12-mm diameter Si lens to get a better coupling of the illuminating radiation, the size and the thickness of the Si lens is optimized according to the focusing spot size and usually selected for the radiation coupling.

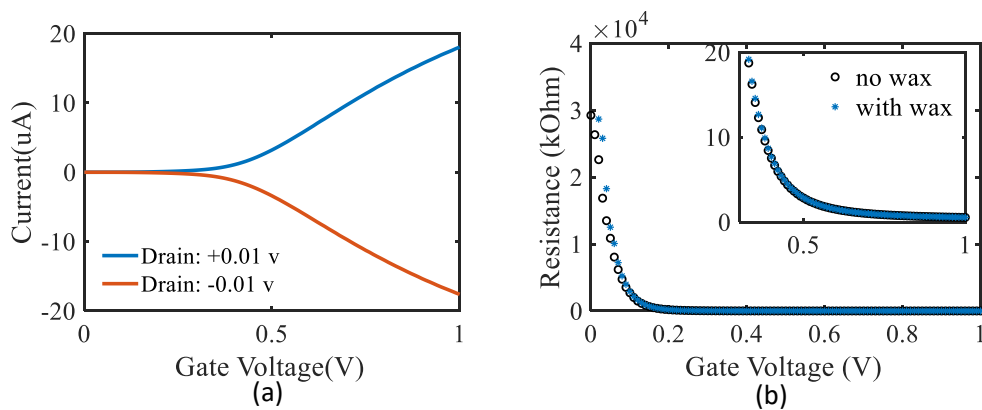


Figure 4.2: (a) I-V response of the detector with the drain biases of  $\pm 0.01$  V, and (b) DC resistance of the detector versus the gate voltage supply.

In the measurement setup, a PTFE focusing lens with 3-inch diameter and 15-cm focal

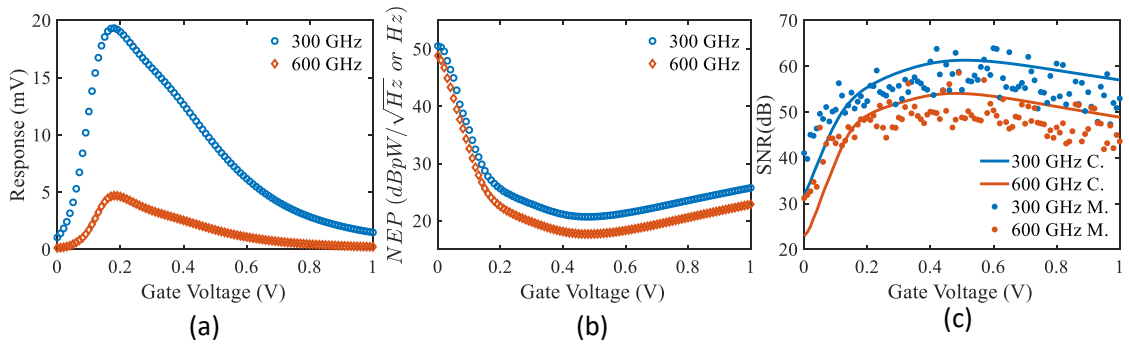


Figure 4.3: Detector response with 12-mm diameter Si lens at 300 GHz ( $600\text{-}\mu\text{W}$  output power) and 600 GHz ( $56\text{-}\mu\text{W}$  output power). (a) Output voltage versus different gate voltage supply, (b) NEP over the gate voltage and (c) relative signal to noise ratio (SNR) including the measured (indicated with M.) and calculated (indicated with C.) values.

length is utilized to focus the radiation onto the Si lens in free space at both 300 GHz and 600 GHz. The best NEP with  $600\ \mu\text{W}$  output power of 300 GHz radiation is  $117.49\ \text{pW}/\text{Hz}^{-2}$  and it is reduced to  $58.75\ \text{pW}/\text{Hz}^{-2}$  at 600 GHz with a  $56\ \mu\text{W}$  source output power. This is comparable to the description in Ref.[92]. The measured (marked with letter C.) and the calculated (marked with letter M.) signal to noise ratio (SNR) based on NEP is shown in Fig. 4.3. The general trends of the measured data and the calculated data are consistent. The jitter of the measured data can be attributed to the intrinsic lock-in noise and the THz radiation distributed in the surrounding environment. Furthermore, the data shows that the peaks of the SNR is at the gate voltage of 0.48 V for both 300 GHz and 600 GHz radiation. Which also means the best dynamic range point is located at this gate voltage supply.

To work in the sub-harmonic regime and be implemented into Fourier imaging application, the detector cannot receive the radiations under the 12-mm diameter Si lens. Smaller aperture size Si lens need to be used for detected radiation to enable a proper pixel size. On the other side, where LO is coupled, the bonding wires of the chip hinders the lens integration. However without substrate lens, LO coupling efficiency will be pretty low which will affect the detection performance. To solve the problem, the detected radiation can be coupled through a 4-mm diameter Si substrate lens glued on the back side of the detector, meantime, the sub-frequency LO can be coupled from the front side

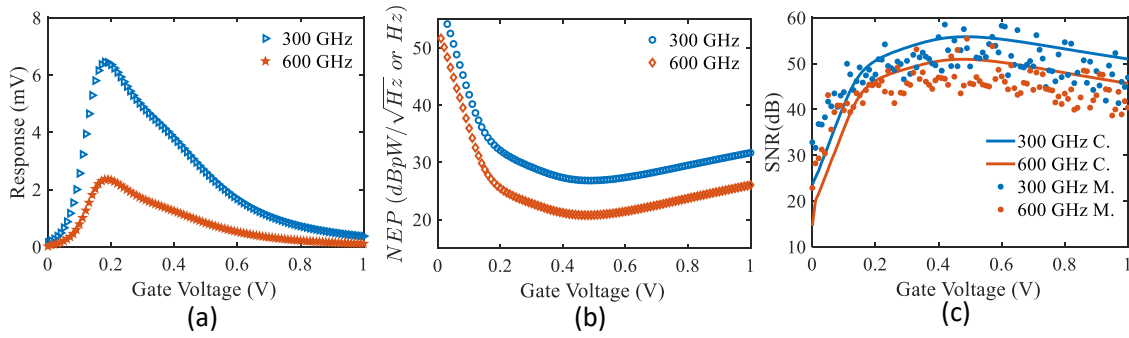


Figure 4.4: Detector response at 300 GHz ( $600\text{-}\mu\text{W}$  output power) with 8-mm diameter wax/PTFE lens and at 600 GHz ( $56\text{-}\mu\text{W}$  output power) with 4-mm diameter Si lens. (a) Output voltage over different gate voltage supply, (b) NEP over the gate voltage and (c) relative signal to noise ratio (SNR) including the measured (indicated with M.) and calculated (indicated with C.) values.

of the detector through a wax/PTFE lens. The wax/PTFE lens allows itself to contain the bonding wires inside and integrated on the detection chip directly, at the same time, improve the LO coupling efficiency to the acceptable level.

The direct detection of the 600-GHz and 300-GHz radiation are explored with the two-lens-integrated detector to demonstrate the detection performance with the lenses. The DC resistance of the detector with the wax/PTFE lens is shown in Fig.4.2 (b) with the blue circle line. In this figure, the unchanged resistor by adding the paraffin wax layer can be observed, which proves the feasibility of wax-PTFE lens. The response of the detector under 300-GHz (with a 8-mm diameter wax/PTFE lens) and 600-GHz (with a 4-mm diameter Si lens) illumination, the calculated NEP based on the response and DC transistor resistor and the related SNR curve are shown in Fig. 4.4. All the data are captured by linearly scanning the gate voltage of the transistor. The response of 300-GHz radiation declines a lot however of 600-GHz radiation a little bit. This is because, the refractive index of the wax/PTFE (1.52 for paraffin wax, the measurement result will be shown in Chapter 4.1.4 and 1.42 for PTFE [93]) is about 2.5 times smaller than the refractive index of the Si (approximately 3.5), the focusing efficiency of the wax/PTFE lens at 300 GHz therefore is not so good as that with the same size Si lens. While at 600-GHz, the shorter wavelength allows smaller focusing spot size than 300 GHz radiation. Thus the squeezing size of the Si substrate lens does not affect too much. The corresponding

NEP at 300 GHz and 600 GHz are  $481.95 \text{ pW/Hz}^{-2}$  and  $119.94 \text{ pW/Hz}^{-2}$ . At 300 GHz, it is 4 times of the initial detector, and at 600 GHz, it is 2 times. Though the detector is not integrated in optimum status for single direct detection, it is the best choice for sub-harmonic detection and can meet the requirements of Fourier imaging at 600 GHz. The related SNR curve shows that the best SNR gate voltage keep the same as 0.48 V.

Based on Eq. 4.5, one can see that in the SHHD case, the followings hold

1. The output changes with the fluctuation of  $V_{RF}$  instead of  $V_{RF}^2$ , which means when the RF signal is weak and decreasing, the output of a heterodyne detector drops much slower compared with that of a direct detection one.
2. The output signal is also proportional to  $V_{LO}^2$ . Normally, as the LO power is considerably higher than the RF signal, the output signal will also be stronger.
3. Phase information of the RF signal ( $\phi_{RF}$ ) is preserved at the output. As a result, electrical scanning based on digital beam steering is achievable, which has the potential to replace the traditional mechanical scanning to significantly reduce the imaging time.

Combined Eq.4.4 and Eq. 4.5, one can find the NEP of 2nd sub-harmonic detection can be deduced as

$$NEP_{heter} = \frac{4k_B T R}{V_{res}^2 / P}. \quad (4.7)$$

To evaluate the measurement, the I-V and the response data are necessary. The sub-harmonic response by tuning the gate voltage based on one lens case (indicated by no lens in figure) and the double lens model (indicated by with wax/PTFE lens) are displayed in Fig. 4.5 (a). From the data, one will find the sensitivity is enhanced by approximately 10 dB by using the wax/PTFE lens. The corresponding NEP and SNR are shown in Fig. 4.5 (b) and (c), from where the NEP and SNR enhancements driven by the wax-PTFE lens are both 20 dB.

The minimum NEP is found to be  $17.33 \text{ pW/Hz}$  and  $0.3 \text{ pW/Hz}$  for the cases without and with wax/PTFE lens. Comparing with the direct detection which keeps the same

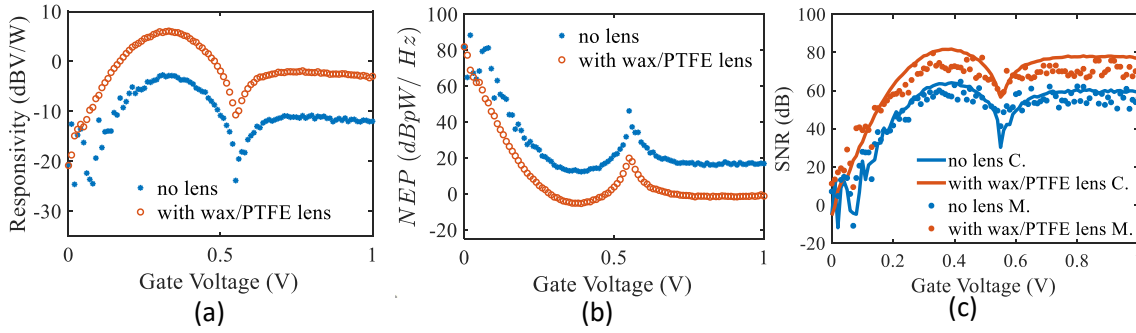


Figure 4.5: Sub-harmonic response of the detector with a 4-mm diameter Si lens and without/with a 8-mm diameter wax/PTFE lens. (a) Responsivity, (b) NEP and (c) relative signal to noise ratio (SNR) versus gate voltage supply including the measured (indicated with M.) and calculated (indicated with C.) values.

illuminating power and detection hardware, the NEP is 27.8 times and 1606.5 times better for two cases. The peak value of SNR appears at the gate voltage of 0.38 V, which is different from the best SNR voltage in the direct detection. During the whole experiment of Fourier imaging based on SHHD, the gate voltage is set as 0.38 V to guarantee the detector works in the optimal status.

### 4.1.3 Integration of sub-harmonic detection in THz Fourier imaging

As aforementioned, Fourier imaging records the data in the focal plane of the imaging system. In this plane, most of the energy is concentrated in the central area to convey the low space frequency information of the imaged target. Going away from the center, locates the high space frequency component. The further from the center, the higher spatial frequency settles, meanwhile, its energy is weaker. Thus to achieve the desired imaging quality, i.e. record the data in a certain distance from the center in Fourier plane, high sensitivity and low noise level of the detection is required. Since the sensitivity, NEP and SNR of SHHD rely on the intensity of the LO radiation, the coupling efficiency of the LO radiation is crucial to meet the requirement of Fourier imaging. This section therefore focuses mainly on the discussion of the LO coupling efficiency.

The usual radiation coupling method mostly adopted at sub THz frequencies has two

steps. The first step is to focus the radiation by using a optical lens such as Teflon lens in free space, the second step is a boosting focus procedure based on the first step by utilizing a hemispherical or hyperhemispherical Si substrate lens. For the first step, the size of the focus spot can be estimated by the Gaussian distribution theory the same as that used in the optical range since the source radiation in our system has a Gaussian-like distribution in free space. The mathematical calculation of the focus spot size thus is

$$D_s = \frac{4M^2\lambda f}{\pi D}, \quad (4.8)$$

where  $\lambda$  is the wavelength,  $f$  is the focal length of the lens,  $D$  is the beam diameter projected onto the lens (at the  $1/e^2$  of the peak value),  $M^2$  is the beam mode parameter and for ideal TEM<sub>00</sub> laser beam  $M^2 = 1$ . This formula shows that the selection of the focusing lens depends on the divergence angle of the incident beam or the aperture of the collimated incident beam. In the experiment, a 3-inch-aperture Teflon lens with 15-cm focal length is utilized to focus the 300-GHz waves radiated by the multiplier chain with the horn antenna (diverging angle is  $20^\circ$ ). The focus spot size has a 7.4-mm diameter. Using a focusing lens which has 2-inch diameter and 10-cm focal length to focus the 600-GHz radiation emitted by the multiplier chain with the  $27^\circ$  diverging angle horn antenna, the focus spot size is 5 mm in diameter. For the second step of the focusing, the selection of the size of the Si substrate lens depends on the size of the first-step focusing spot on one hand. On the other hand, taking the effect that at a large angle of incidence the refracted light concentration efficiency will be reduced into consideration, the diameter of the substrate lens should be larger than that of the first-step focused spot. For LO coupling in single pixel detector case, it is easy to meet this conditions. However, for the detected radiation in imaging applications, the size of the substrate lens is also the pixel size. Thus the pixel size limitation has to be considered. For Fourier imaging, a large pixel size in Fourier plane will squeeze the imaging area or the field of view. In this case a proper small size of substrate lens needs to be selected even though it will take the expense of sacrificing energy coupling efficiency. Taking all the above discussed conditions into consideration, the 4-mm Si lenses from Tydex is selected as the substrate

lens for imaging radiation coupling at both 300 GHz and 600 GHz, the 12-mm diameter Si lenses from Tydex can be used for detector calibration.

For Fourier imaging at sub-THz frequency, if one wants to keep the coupling of LO radiation in the back-side direction through the Si substrate lens, the most efficient way is the configuration sketched in Fig. 4.6a. In this setup, a Si wafer is in demand for combining the imaging radiation and the LO radiation. While for both radiations, the power will be attenuated by at least 3 dB for the reason that the beam combiner is 50% transmitting and 50% reflecting for the radiation power. In addition, the bulk volume of the Si wafer will block the use of a shorter focal-length lens. This will prevent the enhancement of the resolution or reduce the scanning area (demonstrated in the imaging area and imaging resolution part in Section 2.3.2). The heterodyne working mode demonstrated at 300 GHz uses the  $18\times$  VDI multiplier chain as the imaging radiation and the  $18\times$  RPG multiplier chain as the LO radiation. A substitution is that shown in Fig. 3.1, the LO radiation is focused by the Teflon lens and coupled through the front side of the detector in free space. The advantage of this configuration is the compact system, high imaging energy utilization and high resolution possibility. However, migrating to 600 GHz, the LO coupling efficiency is not strong enough in direct free space coupling. One reason is that the radiation power at 600 GHz is lower, therefore, the demand for LO coupling is more strict. Another reason is the intrinsic low conversion efficiency of the LO radiation.

If one still wants to apply the two sides coupling detector in Fourier imaging using SHHD, the LO coupling efficiency needs to be promoted. However, it is impossible to do that with the conventional method by integrating a Si lens because of the existence of the bonding wires which is utilized to connect the readout circuit and the detector chip on the front side. To solve the problem, the idea of utilizing a 4-mm diameter Si substrate lens to the back side of the detector and integrating a two-stage wax/PTFE lens on the front side of the detector is proposed. This design can balance the imaging pixel size, resolution, the coupling efficiency of the radiations to the detector and the dynamic range of the imaging. The system is shown Fig. 4.6b. It in outlook looks the same as Fig. 3.1, but the detector is integrated differently. The Si substrate lens is used to collect the

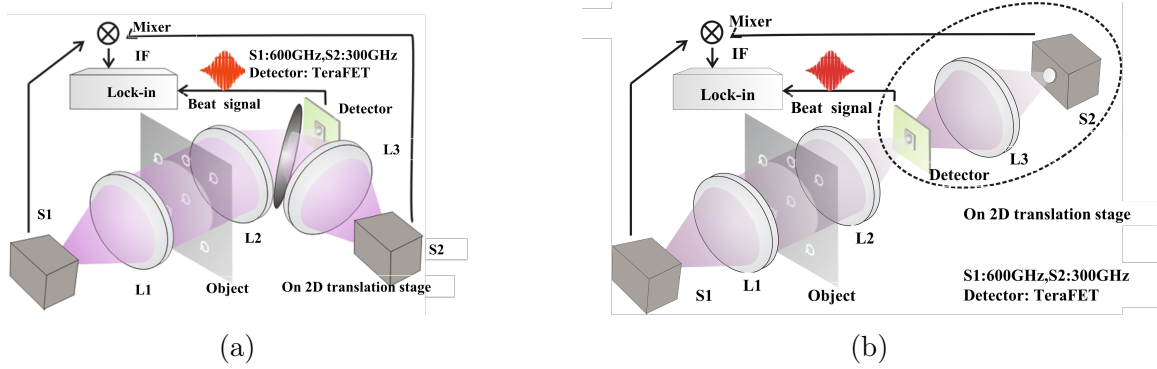


Figure 4.6: Schematic of Fourier imaging system based on sub-harmonic detection. (a) The LO radiation coupled onto the detector through the Si substrate lens integrated on the back side of the detector, (b) the LO radiation is coupled onto the detector from the front side of the detector.

imaging radiation while the wax/PTFE lens is aiming at coupling the LO radiation into the detector. In this way, the coupling efficiency of the LO power is improved by 10 dB (will be demonstrated in Section 4.1.6), in other words, the sensitivity will be raised by 20 dB for the sub-harmonic detector in this case, which will make it possible for Fourier imaging at 600 GHz with 300-GHz radiation as LO waves.

#### 4.1.4 Characteristics of paraffin wax at THz band

White colored paraffin wax is a soft solid derived from petroleum, coal or shale oil. The molecular formula is  $C_nH_{2n+2}$ , where  $n = 20 \sim 40$ . It is solid at room temperature and begins to melt above approximately  $37^\circ C$  ( $99^\circ F$ )[2]. Common applications include lubrication, electrical insulation, and candles, here, it will be used for the substrate lens of the TeraFET at sub-THz frequency since it is easy to be melted and has a soft solid state. Thus, the validation of the characteristics of paraffin wax at THz range is crucial.

The characteristics of the paraffin wax at THz frequencies are achieved by using the THz time-domain spectroscopy (TDS) system. The TDS system has a frequency bandwidth of 2.5 THz. The samples are prepared by melting and drawing the paraffin wax into film with a metal ring frame. They are prepared in three different thickness, 0.82 mm, 1.37 mm and 2.44 mm. The photo of the samples is shown in Fig. 2.5.

When the TDS system works without any samples, the reference time domain pulse is



Figure 4.7: Photo of the wax material.

captured. It is shown as the black line in Fig. 4.8. When the samples are inserted into the system exactly in front of the THz emitter, the detected transmitted data are the blue, red and rose red lines in Fig. 4.8 corresponding to the sample thickness of 0.82 mm, 1.37 mm and 2.44 mm, respectively. From the data, one can see that the delay time is proportional to the thickness and defined by the refractive index  $n$ . Reference pulse and the pulses with samples have two peaks. These two peaks are generated by the reflections of the front and back surfaces of the GaAs wafer (380  $\mu\text{m}$  thick) which is used for THz waves generation. The first peak in the time domain pulse contains all the information of the paraffin-wax sample. Thus only the main peak will be kept for the derivation of the refractive index and the permittivity. If one includes the second peak in the calculations, oscillations will appear in frequency spectrum.

Once the data is prepared, the reference  $Er$  and the test data  $Es$  in the time domain are Fourier transformed to the frequency domain. The phase information  $\phi_s$  and  $\phi_r$  in the frequency domain are used to calculate the sample refractive index  $n$  by applying

$$n(f) = n_0 + \frac{c|\phi_s(f) - \phi_r(f)|}{2\pi fd}, \quad (4.9)$$

where,  $c$  is the light velocity,  $d$  is the thickness of the sample,  $n_0$  is the refractive index

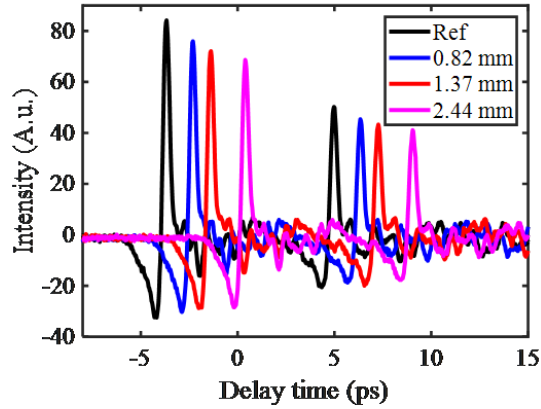


Figure 4.8: Transmission THz pulse with and without paraffin wax material.

in the air,  $f$  is the frequency. Based on Eq. 4.9, the permittivity can be calculated by

$$\varepsilon(f) = n^2(f) - k^2, \quad (4.10)$$

where  $k$  is the extinction coefficient, for the polymer material,  $k$  is much smaller than  $n$ , thus in practical calculation,  $\varepsilon(f)$  is approximated as the square of  $n(f)$ .

The Fourier transformed spectrum of the reference pulse and the measured pulses of the samples are plotted in Fig. 4.9. Fig. 4.9a presents the intensity of the frequency spectrum and Fig. 4.9b depicts the phase of the frequency spectrum from 0.4–0.5 THz.

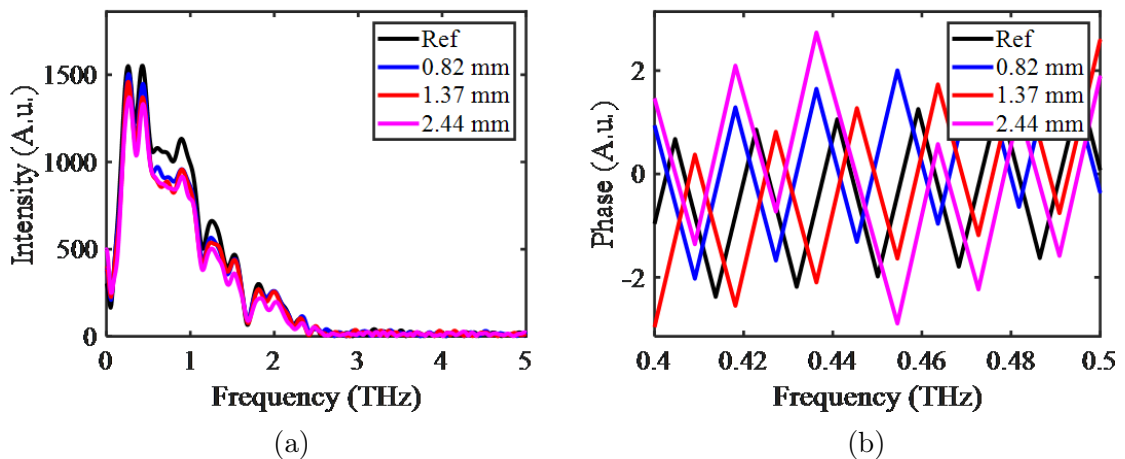


Figure 4.9: The Fourier transform spectrum of the reference pulse and the test pulses of the samples. (a) The intensity of the frequency spectrum, (b) the phase of the frequency spectrum.

From the complex frequency spectrum of the test data and the reference data, the transmission and the phase delay at each frequency can be calculated. They are displayed as Fig. 4.10a and 4.10b, respectively. The transmission has a value higher than 80% over the whole range, and for the 0.82-mm sample the transmission is higher than 90%, showing a relatively weak reflection and absorption loss at 0.3-1.5 THz.

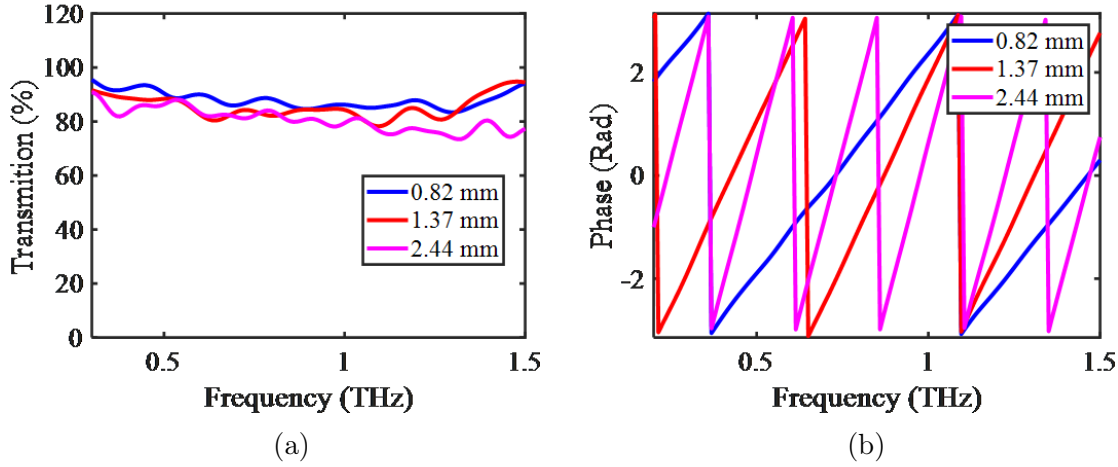


Figure 4.10: The transmission rate and the phase delay of paraffin wax at each frequency. (a) The transmission rate of paraffin wax, (b) the phase delay of paraffin wax.

Taking the phase delay and the thicknesses of the samples into Eq. 4.9, the refractive index of the paraffin wax can be calculated. Results are shown in Fig. 4.11. The refractive index decreases a little bit as the frequency gets higher, having the value of 1.52 at 300 GHz and an average value of 1.515 at the whole range.

To calculate the permittivity of the paraffin wax at the sub THz band, the extinct coefficient  $k$  is in demand. The relationship between  $k$  and the transmission, refractive index and the thickness of the sample can be expressed as

$$k = \ln\left[\frac{4n(f)}{T(f)(n(f) + n_0)^2}\right] \frac{c}{2\pi f d}. \quad (4.11)$$

The derived extinct coefficient  $k$  over the frequency range for different samples is displayed in Fig. 4.12a. Based on this, one can get the absorption coefficient  $\alpha$  by

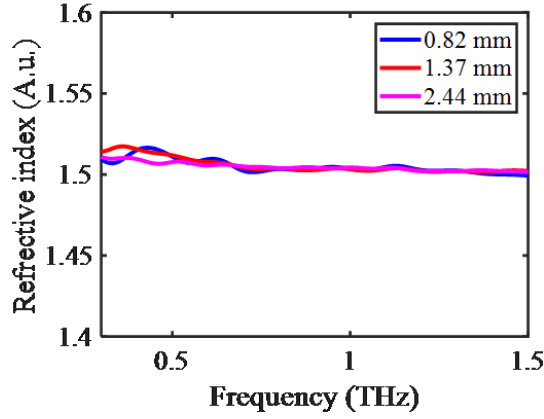


Figure 4.11: Refractive index of the paraffin wax at THz range.

applying

$$\alpha = \frac{2\pi f k}{c}. \quad (4.12)$$

The measured absorption coefficient is displayed in Fig. 4.12b. The test results here show a value of  $0.5 - 1/cm^{-1}$  (The value for the thickest sample is captured since the thickness of the thin sample is close to the wavelength thus reflection and interference will affect the measurement).

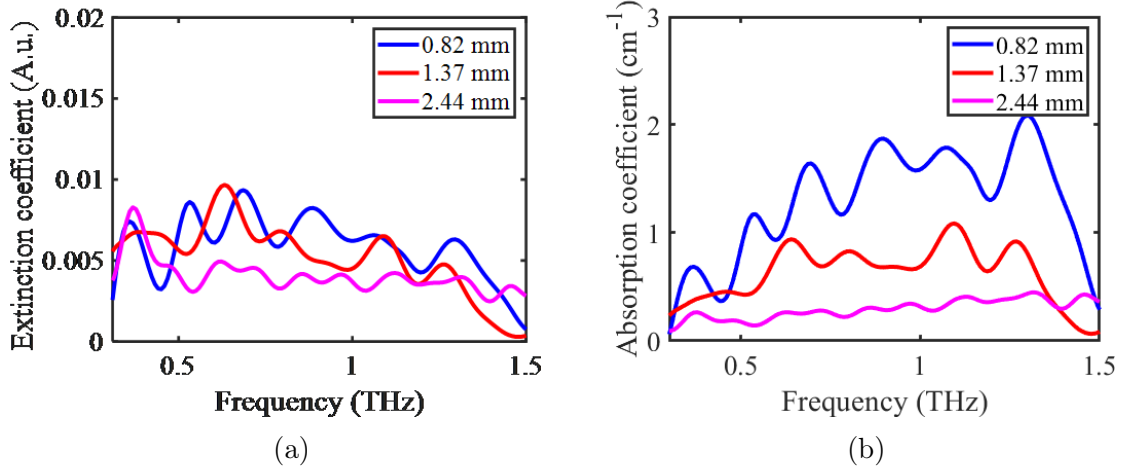


Figure 4.12: Absorption and extinct coefficient of paraffin wax with frequency. (a) Absorption coefficient of paraffin wax, (b) extinct coefficient of paraffin wax.

Taking  $k$  and the refractive index  $n$  back to Eq. 4.10, one can find the permittivity for the paraffin wax can be expressed as Fig. 4.13. From the measurement results, one

will find that the paraffin wax has a quite stable permittivity value over 0.3-1.5 THz of approximately 2.4.

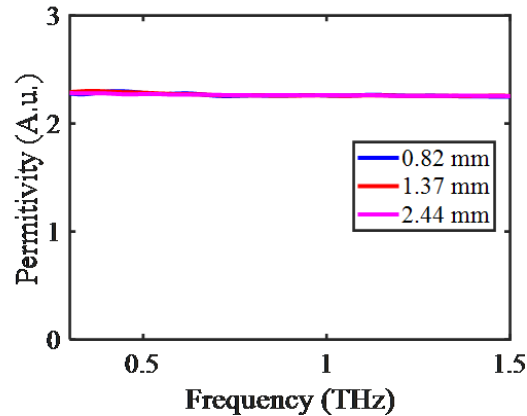


Figure 4.13: Permittivity of the paraffin wax at THz range.

The relatively flat dispersion characteristics over a frequency range of 0.3 to 1.5 THz have been observed for all the parameters of the paraffin wax material. The transmission data shows that the absorption is low enough for paraffin wax to work in the range from 300 GHz to 1.5 THz, and the elements built by the material will have a broadband response though in this work the system is merely operating at a certain frequency. The transition period of melting and solidification paraffin wax allows it to be used as a protective material for bonding wires. In addition, the similar refractive index to that of PTFE material [93] supplies the opportunity to use it for the compound lens combined with a custom-designed PTFE lens.

#### 4.1.5 Processing of wax/PTFE lens on TeraFET detectors

The composite wax/PTFE lens is fabricated by first dripping molten wax onto the detector to embed the bonding wires and form a protection layer, then on top of this layer after its hardening, a custom-designed hemispherical PTFE lens is pasted exploiting the adhesive character of the re-warmed and softened wax. Fig. 4.14 is the schematic of the integration of the detector and the photos of the detector with the wax/PTFE and Si lens.

The size and the shape of the PTFE lens should be custom designed to focus the radiation effectively. According to Snell's law, during the propagation, when the elec-

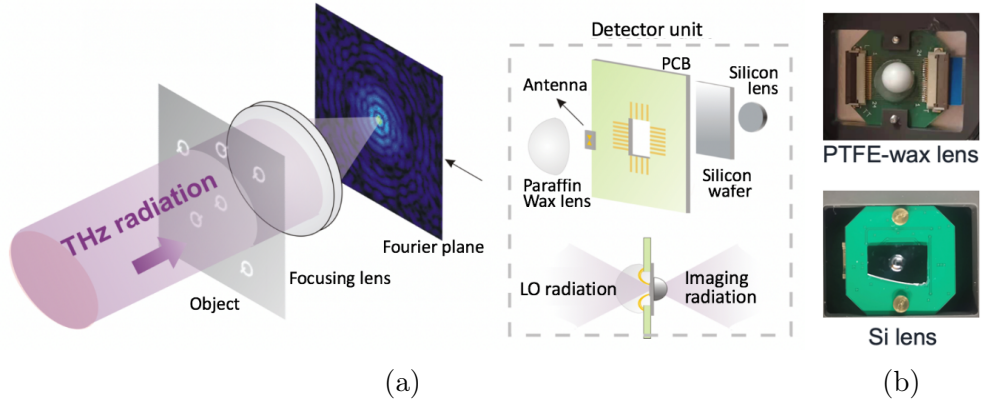


Figure 4.14: Schematic of the wax/PTFE lens and the Si lens integration on the detector. (a) Schematic of the integration of the wax/PTFE lens and the Si lens on the detector, (b) photo of wax/PTFE lens.

When electromagnetic waves interact with a curved dielectric material surface, the beam will be refracted. Therefore, the divergent or parallel incident beams can be gathered to a single point by designing a reasonable lens structure to achieve energy focusing.

In the situation of LO injection, the THz radiation will be focused first by a Teflon lens before it arrives at the detector. However, the focus spot size is much larger than the active detection area of the detector, which will lead to energy waste. Thus here a focusing lens that can be integrated on the detector chip is in demand to focus the first step spot to a tighter one (comparable to the level of the active detection area). Usually a single lens for a tight focus design under a focusing beam situation needs to be a hemispherical lens or super hemispherical lens. For better focusing quality consideration, first, an aspherical surface is used for the lens design and named as booster lens. Assuming the lens is set in the Cartesian coordinate system  $(h, r)$  as Fig. 4.15 shown. If there is no booster lens, the radiation will be focused to the point  $S_0$ , if the booster lens is inserted, the radiation will first hit the point  $(h, r)$ , after refraction will be focused to the point  $S_1$ . The total optical path will be changed from the original value  $R$  to the sum distance in the air  $l_1$  and the path in the booster lens  $nl_2$ . For all the radiation focused to a single point, the optical path keeps a constant value of  $s = l_1 + nl_2$ . In this case, the optical path in the air  $l_1$  is

$$l_1 = R - \sqrt{(R - h)^2 + r^2}. \quad (4.13)$$

The math distance in the lens  $l_2$  is

$$l_2 = \sqrt{r^2 + (d - h)^2}, \quad (4.14)$$

where  $d$  is the center thickness of the booster lens.

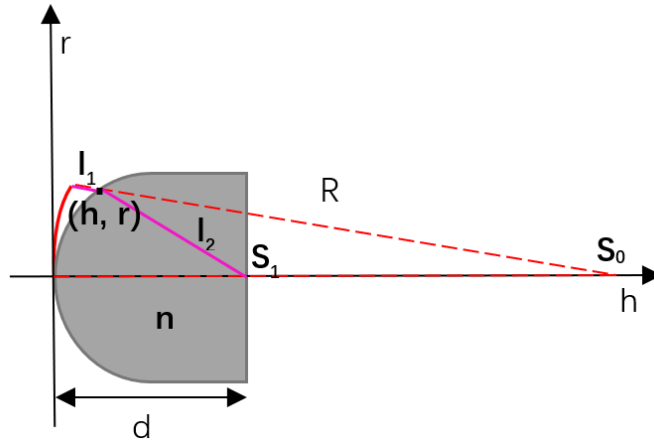


Figure 4.15: Schematic of the light refraction in wax/PTFE lens.

Substituting the total optical path with  $l_1$  and  $l_2$ , the equation will be

$$R - \sqrt{(R - h)^2 + r^2} + n\sqrt{r^2 + (d - h)^2} = nd, \quad (4.15)$$

from which, one can get the relationship between  $h$  and  $r$  (i.e. the surface shape of the booster lens) if the focus spot size is known and the thickness of the booster lens is given. For the actual situation, the original optical length  $R$  is much larger than the thickness and the maximum radius of the booster lens. By this assumption, Eq. 4.15 can be simplified to

$$\sqrt{r^2 + (d - h)^2} = d. \quad (4.16)$$

It is a hemispherical lens expression with the radius of  $d$ . For 300-GHz radiation, the focus point in the free space by using a Teflon lens is 7.5 mm, thus the 8-mm radius is selected for the booster to be integrated in the system.

### 4.1.6 Characteristics of wax/PTFE lens on TeraFET detectors

To identify the characteristic of the paraffin lens, the coupling efficiency of the LO radiation without and with wax/PTFE lens (shown in Fig. 4.16) will be calculated.

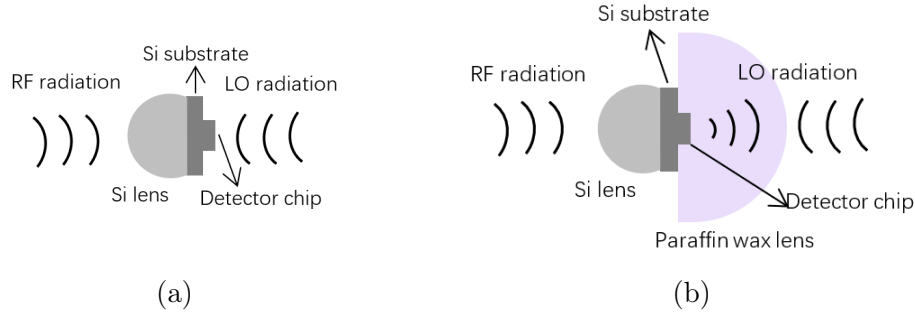


Figure 4.16: Schematic of the LO injection non- and through paraffin wax onto the detector. (a) LO injection without the wax/PTFE lens, (b) LO injection with wax/PTFE lens.

Overall pattern-coupling efficiency of detection depends on the integral of the field distribution on the effective area of the antenna and the matching efficiency of the antenna and the transistor. The matching efficiency of the antenna and the transistor is fixed for specific chip design, therefore the analyzation will only focus on the focused field energy distribution related to the optical system and effective detection area derivation depended on the detector geometry.

In practice, a single pixel detector is usually illuminated by a focused THz beam that assumed to have a Gaussian power density distribution. Placing the detector within the focus spot in the focal plane where the field energy density is maximum has the best optical coupling efficiency. The pre-focusing optical system usually consists of a convex Teflon lens. The focus spot and the energy distribution can be calculated by Fast Fourier Transform (FFT) of the field distribution in the pupil of the beam focused system according to the physical optics theory. This is also defined as PSF (point spread function) in optical design. In this work, a substrate wax-PTFE lens is used for coupling efficiency enhancement. To compare the focusing systems and find the optimum system configurations with and without wax-PTFE lens, the commercial software Zemax is utilized. In Zemax simulation, material effects and the aberrations of the lenses are included. System can also be optimized by using merit functions. Therefore, the result can be regarded

as a pertinent evaluation. Fig. 4.17 shows the simulation systems and results. The pre-focusing Teflon lens is a hyperboloid-surface lens with 5-cm focal-length. The two-satege wax-PTFE lens consists of a 8-mm diameter PTFE hemispherical lens and 2.1-mm thickness wax layer (optimized for the best focus on the antenna plane under illuminating wavelength of  $1mm$ ). The detail parameters of the systems are in Appendix A. Fig. 4.17 (a) is the 3D presentation of the PSFs. The insets are the layout of the system. The left and right panels are the PSFs without and with the wax-PTFE lens after optimization. Fig. 4.17 (b) presents the cross section of the PSFs normalized by the total power. The normalized curves show that a much higher energy density can be achieved by using a wax-PTFE lens.

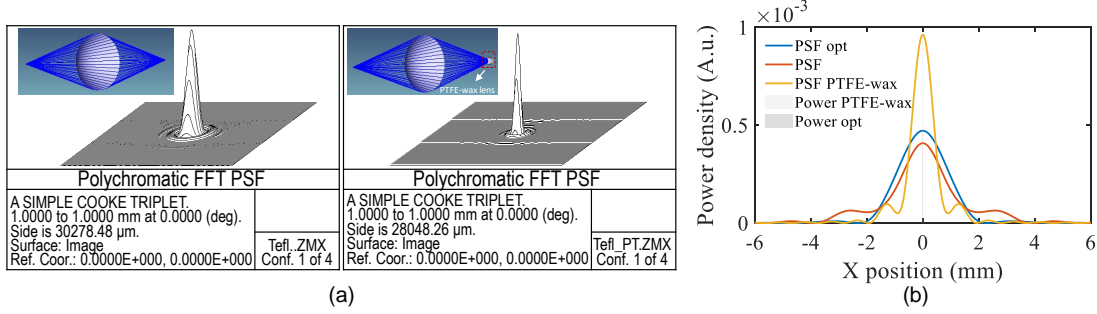


Figure 4.17: Simulation of the LO coupling systems with/without the wax-PTFE lens. (a) The polychromatic FFT PSF figures of the optical coupling without and with wax-PTFE lens and (b) the cross PSF data after energy normalization for the systems with and without wax-PTFE lens.

If the detector is embedded on the contact surface of two half infinite dielectric materials, the radiation power ratio on both sides can be roughly defined as  $n_1^3/n_2^3$  ( $n_1$  and  $n_2$  are the refraction indexes of the dielectrics) [94]. Thus the directivity in the direction to dielectric 1 is  $n_1^3/(n_2^3 + n_1^3) \cdot D_r$  ( $D_r$  is the total antenna directivity). Based on  $A_r = (D_r \lambda^2)/4\pi = (n_1 + n_2) \cdot A_{antenna}/2$  [95], where  $A_r$  is effective antenna area and  $A_{antenna}$  is the physical antenna area, the equivalent effective antenna area in dielectric 1 will be

$$A_1 = \frac{n_1^3(n_1 + n_2)}{2(n_2^3 + n_1^3)} \cdot A_{antenna} \quad (4.17)$$

The focus of research is coupling the LO through the front-side of the detector while the Si substrate and the hemispherical Si lens is used on the other side to approximate

semi-infinity dielectric. Therefore in Eq.4.17,  $n_2$  should be substitute by  $n_{Si}$ ,  $n_1$  by  $n_{air}$  or  $n_{wax}$  for the two coupling systems. Applying  $n_{Si} \approx 3.5$ ,  $n_{air} = 1$ ,  $n_{wax} = 1.52$  (see Appendix A for detail) and  $D_{antenna} = 220 \mu m$  ( $D_{antenna}$  is the diameter of the physical antenna area), one will find the equivalent effective diameters of the antenna area in air and wax-PTFE lens directions are  $11.3 \mu m$   $41.8 \mu m$ , respectively. These are relatively small values compared with the physical size of the antenna. Using these sizes as the integral boundary of the power density distributions in Fig. 4.17 (b) (the dark and light gray areas), the coupling efficiency / received power promotion by the wax-PTFE can be derived as  $14 dB$ . Taken the absorption of the PTFE and paraffin wax material with 10% (derived based on material thickness and absorption coefficient, see Appendix A for detail) at 300 GHz in consideration, the value is still  $13.5 dB$ .

After finding the optimum system, we can put the systems in HFSS to do the simulation which include the reflections of the materials and the effect of the Si on the other side of the detector. The simulated results are shown in Fig. 4.18. Fig. 4.18 (a) shows the

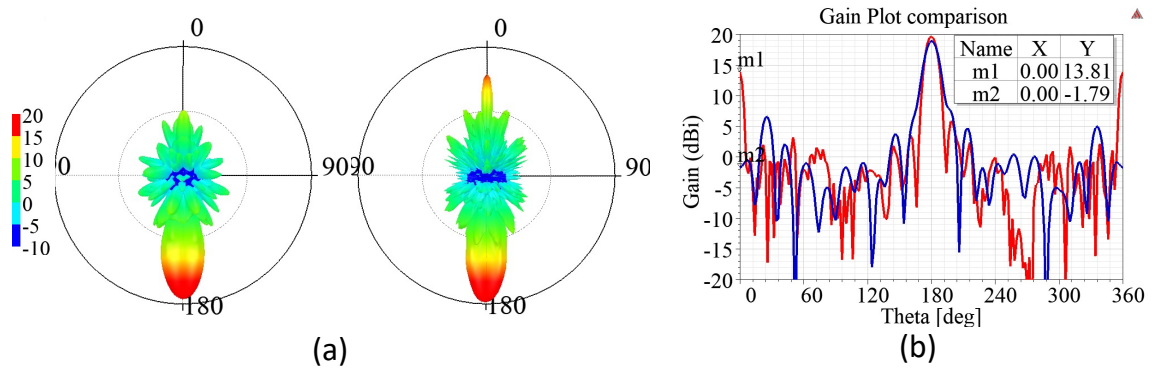


Figure 4.18: Simulation of the LO coupling systems with and without the wax-PTFE lens in HFSS. (a) The 3D directivity plot without and with wax-PTFE lens and (b) The E-plane data for the systems with and without wax-PTFE lens.

3D directivity of the two setups, one can find from the figure, the coupling efficiency in the Si lens side is much higher than that on the other side. Even though, the wax-PTFE lens show a obviously enhancement. Fig. 4.18 (b) displaces the 1D data in E-plane, from which one can find the coupling efficiency in LO direction is improved by  $15.6 dB$ . The reason of this is higher than Zemax calculation is that the multi-reflections in the Si lens

generates the standing waves. However, due to the refractive index mismatch between the PTFE material and the paraffin wax material and the undefined aberrations of the lenses, the measured coupling efficiency enhancement is just 10 dB (shown in Fig. 4.5 (a)).

## 4.2 Dynamic range enhancement of wax/PTFE lens integration

Integrating the detection unit shown in Fig. 4.14 to the system as that in Fig. 4.6b, the Fourier spectrum of the Siemens star depicted in the bottom plots in Fig. 4.19 can be achieved. The left plot is the intensity distribution and the right plot is the phase distribution. The top plots in Fig. 4.19 are the Fourier space spectrum recorded by using the detector without wax/PTFE lens (left panel is the intensity distribution and the right panel is the phase distribution). Comparing the two sets of data, one will find, the dynamic range of the Fourier spectrum is improved from 25 dB to 45 dB by adding the wax/PTFE lens, which is consistent with the data in Fig. 4.5 (c).

The reconstructed images based on the inverse Fourier transform are shown in Fig. 4.20. The top panels show the retrieved images by using the detector without the wax/PTFE lens, the bottom panels present the results when the wax/PTFE lens is utilized on the detector. In both sets of figures, the left side is the intensity distribution and the right side is the phase distribution. Based on the imaging results, one can find, not only the dynamic range of the reconstructed images are improved by 20 dB approximately, but also the SNR and the contrast of the images are improved notably.

## 4.3 Resolution enhancement of wax/PTFE lens integration

Thanks for the injection efficiency enhancement of the LO radiation by the integration of the wax/PTFE lens on the TeraFET detector, the dynamic range of the imaging radiation

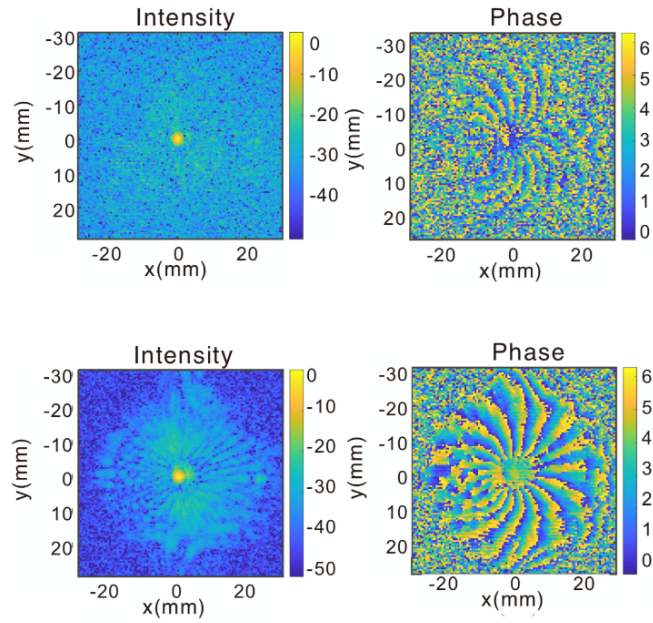


Figure 4.19: Fourier spectrum of the Siemens star under sub-harmonic detection at 600 GHz with and without wax/PTFE lens integrated on the detector, the top and bottom rows are the data recorded without and with the wax/PTFE lens, respectively.

detection is improved markedly in Fourier domain as Fig. 4.19 shown. This in turn allows the detectable area expansion and noise reduction. As the discussion in Section 2.3.2, the larger the detection area in Fourier plane is recorded, the better resolution will be reached by the reconstructed image. Extracting the data along the arcs with different radius (the arcs have radius of 3.2 mm, 4.8 mm, 6.4 mm, and 9.6 mm, corresponding to a local width of the triangular metal patches of the Siemens star of 0.5 mm, 0.75 mm, 1 mm, and 1.5 mm, each patch covers a central angle of  $9^\circ$ ) on the reconstructed images ( the left figures in Fig. 4.21), we can get the 1D intensity distribution shown as the right figures in Fig. 4.21. The top plots in Fig. 4.21 display the image and the 1D data by using the TeraFET detector without wax/PTFE lens, the bottom plots in Fig. 4.21 depict the image and the 1D data with the wax/PTFE lens. The resolution (minimum resolvable distance) is changed from 1.5 mm to 0.75 mm at 600 GHz by utilizing the wax/PTFE lens shown by the comparison of the 1D data. In another word the resolution is improved by two times. After the promotion, the resolution is close to the diffraction resolution limitation of the wave length at 600 GHz (0.5 mm).

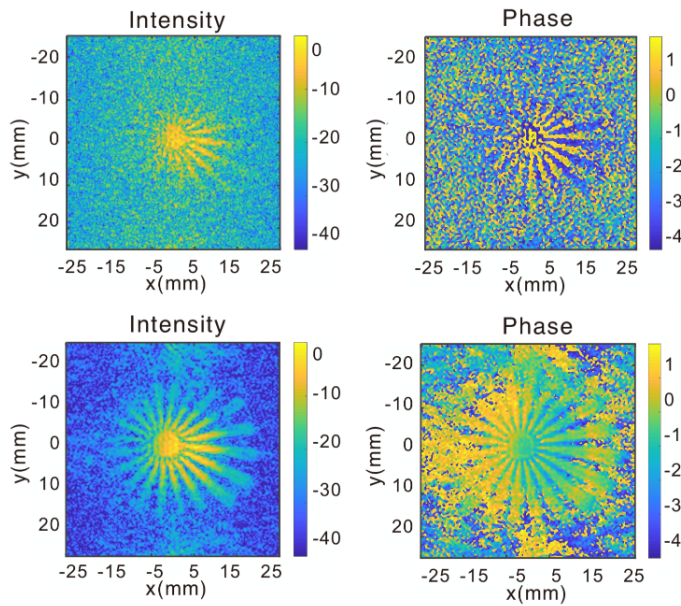


Figure 4.20: The reconstructed imaging results of the data in Fig. 4.19, the top and bottom rows correspond to without and with wax/PTFE lens cases, respectively.

## 4.4 Fourier imaging results at 600 GHz

To further qualify the imaging properties of the Fourier imaging system at 600 GHz, a USAF resolution test pattern on a printed-circuit board is adopted as the imaged target. Fig. 4.22 displays the imaged parts of the pattern (left side) and the reconstructed images (right side). A dynamic range of 35 dB is reached with  $56 \mu W$  power of the 600-GHz imaging radiation. This value is better than the 60 dB obtained at 300 GHz with a power of 1 mW [47]. The difference in dynamic range is to a large degree explained by the much lower small-signal conversion efficiency of sub-harmonic mixing compared with heterodyne mixing [3]. In addition, The lateral spatial resolution is found to be better than 0.9 mm, which is two times smaller than the results obtained at 300 GHz, as expected if the dynamic range is not the limiting factor.

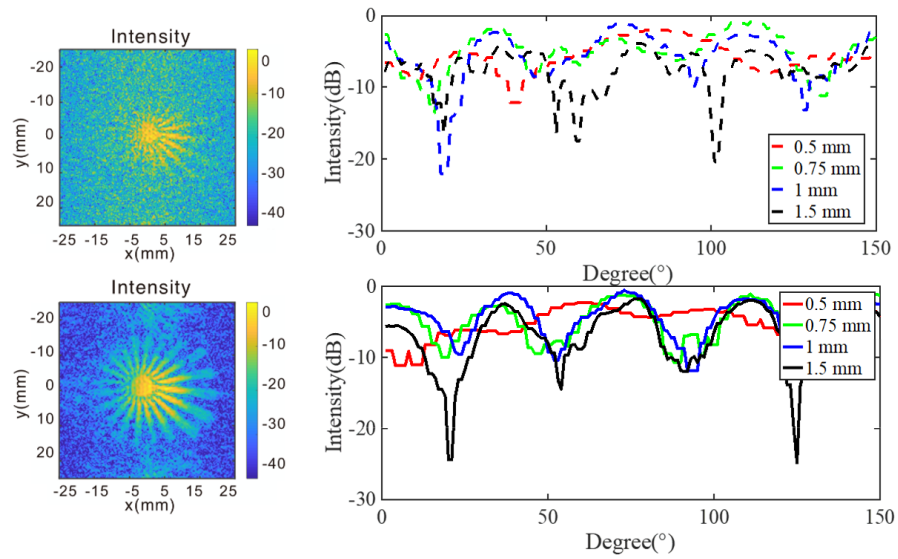


Figure 4.21: Scans along the circular lines shown in the intensity images of the reconstructed intensity results on the left side. The top and bottom rows are without and with wax/PTFE lens results. The legend lists the local width of the metal segments of the Siemens star ranging from 0.5 mm to 1.5 mm, the centers of the circles are located in the centers of the Siemens star images.

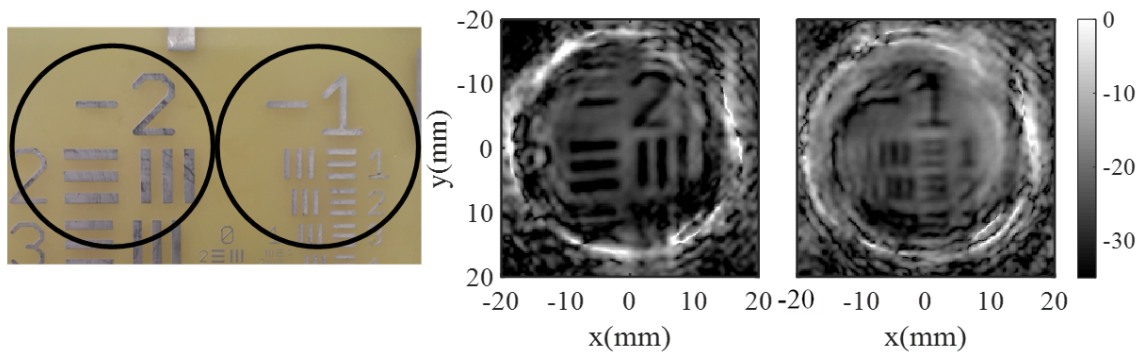


Figure 4.22: Imaging results of USAF resolution chart at 600 GHz based on subharmonic detection. left is the imaged parts of the pattern, right is the reconstructed intensity results.

# 5 Resolution Comparison of Fourier imaging system and microscopy system

Image resolution refers to the ability of a measurement or display system to resolve the details of a sample. It is one of the most important parameters for evaluating the imaging quality. In this chapter, the imaging resolution in 3 dimensions will be exploited to analyze how the Fourier imaging system works. First, the principle lateral resolution of Fourier imaging will be presented, followed by the practical imaging results which can validate the discussion. Based on the lateral imaging resolution, the depth resolution related to the phase will also be investigated and verified by the imaging results. The comparison of the imaging results of conventional microscopy and Fourier imaging system with the same system configuration is compared to show a resolution enhancement by the Fourier imaging system.

## 5.1 Lateral resolution of Fourier imaging setup

A Fourier imaging system is an indirect imaging system as the recorded data is the complex field distribution in the focal plane of the imaging system. The image is numerically reconstructed by the inverse Fourier transform of the recorded data. Based on the physical Fourier transform and digital inverse Fourier transform mechanism, the pixel size/repeating rate in the Fourier plane will be transferred to the key factor of the field of view, while the resolution is defined by the maximum data recording area in Fourier plane. Apart

from the data recording area, the factors that can affect the resolution will be analyzed here and the experimental data will be presented.

### 5.1.1 Lateral resolution of Fourier imaging setup in principle

As described in Chapter 2, the field distribution in the Fourier plane can be expressed as

$$E(x, y) = g(x, y)t(f_\xi, f_\eta), \quad (5.1)$$

where  $g(x, y) = \frac{E_0}{jd\lambda} e^{jk(d_0+f)} e^{j\frac{k}{2f}(1-\frac{d_0}{f})(x^2+y^2)}$ ,  $t(f_\xi, f_\eta) = \iint T(\xi, \eta) e^{-j2\pi(f_\xi\xi+f_\eta\eta)} d\xi d\eta$ ,  $f_\xi = x/(\lambda f)$ ,  $f_\eta = y/(\lambda f)$ . To reconstruct the target scene, the parabolic phase part needs to be removed numerically before the inverse Fourier transform. While, most of the time,  $d_0$  used in the reconstructed procedure can not be exactly equal to the real value in the physical imaging system, suppose  $d = d_0 + \Delta d$  is applied, the residual phase will be

$$\Delta g(x, y) = e^{jk\Delta d} e^{-j\frac{k\Delta d}{2f^2}(x^2+y^2)}. \quad (5.2)$$

Applying it to the field distribution  $E$  in Fourier plane in Eq. 5.1 yields

$$\Delta E(x, y, \Delta d) = \Delta g(x, y)t(f_\xi, f_\eta). \quad (5.3)$$

Take this in consideration, the reconstructed field distribution  $E_o$  in object plane will be

$$E_o(\xi, \eta, \Delta d) = \mathfrak{F}^{-1}[\Delta g(x, y)] \otimes T(\xi, \eta), \quad (5.4)$$

Assuming  $r = \sqrt{x^2 + y^2}$ ,  $\rho = \sqrt{\xi^2 + \eta^2}$ , one will have

$$E_o(\rho, \Delta d) = \mathfrak{F}^{-1}[\Delta g(r)] \otimes T(\rho). \quad (5.5)$$

It is the model of the field distribution modified by the point spread function (PSF) of

the imaging system. The PSF can be expressed as

$$H(\rho, \Delta d) = \mathfrak{F}^{-1}[\Delta g(r)] = 2\pi e^{jk\Delta d} \int_0^{R_{max}} e^{j\frac{k\Delta d}{2f^2}r^2} J_0(2\pi\rho r) r dr, \quad (5.6)$$

where  $R_{max}$  is the maximum radius range of the recording/Fourier plane as defined in Sec. 2.3.3. Since the constant coefficient will not affect the intensity distribution,  $e^{jk\Delta d}$  will be omitted for the later calculation in this chapter.

To calculate the lateral resolution, defocusing is not considered, i.e.  $\Delta d = 0$ , the PSF therefore will be

$$H(\rho, 0) = \mathfrak{F}^{-1}[\Delta g(r)] = 2\pi \int_0^{R_{max}} J_0(2\pi\rho r) r dr. \quad (5.7)$$

Applying  $\mathfrak{R} = 2\pi\rho r$ , the integrated PSF will be

$$H(\rho, 0) = \mathfrak{F}^{-1}[\Delta g(r)] = 2\pi \int_0^{2\pi\rho R_{max}} \frac{J_0(\mathfrak{R})\mathfrak{R}}{(2\pi\rho)^2} d\mathfrak{R}, \quad (5.8)$$

According to  $\int x J_0(x) dx = x J_1(x)$ , Eq. 5.8 can be rewritten as

$$H(\rho) = 2\pi \frac{2J_1(\mathfrak{R})\mathfrak{R}}{(2\pi\rho)^2} \Big|_0^{2\pi\rho R_{max}} = \pi R_{max}^2 \frac{J_1(\pi D_{max}\rho)}{\pi D_{max}\rho}, \quad (5.9)$$

where  $D_{max}$  is the whole range of the recording plane, i.e.  $D_{max} = 2R_{max}$ . Transferring back to Cartesian coordinate system, the PSF can be derived as

$$H_0(x, y) = \pi R_{max}^2 \frac{2J_1\left(\frac{\pi D_{max}\sqrt{x^2+y^2}}{\lambda d}\right)}{\frac{\pi D_{max}\sqrt{x^2+y^2}}{\lambda d}}. \quad (5.10)$$

If the minimum distance between the two points that can be distinguished is  $\delta = \gamma\lambda d/D_{max}$  ( $\gamma$  is a unitless parameter to keep a form consistent with the Rayleigh criterion and only one dimension is taken in calculation), supposing  $I_0 = \pi R_{max}^2$  one will have the intensity distribution

$$I(x) = I_0 \left| \frac{2J_1\left(\frac{\pi D_{max}}{\lambda d}\left(x' - \frac{\gamma}{2}\frac{\lambda d}{D_{max}}\right)\right)}{\frac{\pi D_{max}}{\lambda d}\left(x' - \frac{\gamma}{2}\frac{\lambda d}{D_{max}}\right)} + \frac{2J_1\left(\frac{\pi D_{max}}{\lambda d}\left(x' + \frac{\gamma}{2}\frac{\lambda d}{D_{max}}\right)\right)}{\frac{\pi D_{max}}{\lambda d}\left(x' + \frac{\gamma}{2}\frac{\lambda d}{D_{max}}\right)} \right|^2. \quad (5.11)$$

This equation is derived based on the coherent radiation illuminating situation and suppose that the phase difference between the two points to be discriminated is 0 (the worst resolution situation). The two points are defined to be placed on both sides of the coordinate origin with equal distance. One can extract the intensity distribution in the middle point by

$$I(x) = 4I_0 \left| \frac{2J_1\left(\frac{\pi\gamma}{2}\right)}{\frac{\pi\gamma}{2}} \right|^2. \quad (5.12)$$

Normalizing the middle point intensity by the intensity of one point need to be recognized ( $6I_0$ ) and plotting the intensity coefficient on the coordinate origin position, one can find from Fig. 5.1, when  $\gamma = 1.64$ , the energy  $I(0)$  is a fraction of 0.735, corresponding to the Rayleigh criterion. Thus the resolution in this case is

$$d_{min} = 1.64 \frac{\lambda d}{D_{max}}. \quad (5.13)$$

This is a little worse than the incoherent radiation illuminating situation (principle reso-

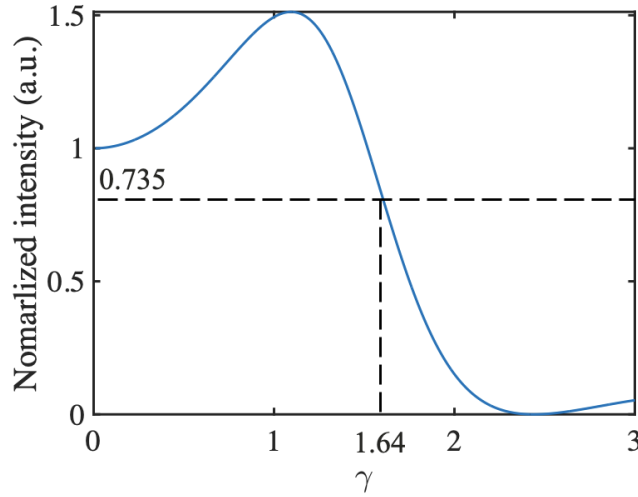


Figure 5.1: The intensity distribution of the point spread function (PSF).

lution is  $1.22\lambda d/D_{max}$  [96]). However, if the phase difference between the two point is not 0 but  $\Delta\phi$ , the resolution will be changed. The intensity distribution will be

$$I(x) = I_0 \left| \frac{2J_1\left(\frac{\pi D_{max}}{\lambda d} \left(x' - \frac{\gamma}{2} \frac{\lambda d}{D_{max}}\right)\right)}{\frac{\pi D_{max}}{\lambda d} \left(x' - \frac{\gamma}{2} \frac{\lambda d}{D_{max}}\right)} + e^{j\Delta\phi} \frac{2J_1\left(\frac{\pi D_{max}}{\lambda d} \left(x' + \frac{\gamma}{2} \frac{\lambda d}{D_{max}}\right)\right)}{\frac{\pi D_{max}}{\lambda d} \left(x' + \frac{\gamma}{2} \frac{\lambda d}{D_{max}}\right)} \right|^2. \quad (5.14)$$

Again, setting the middle position between two points as the coordinate origin, the normalized intensity distribution (normalized by the intensity of one point need to be recognized) change with  $\gamma$  and  $\Delta\phi$  will be

$$I_{nm} = \frac{(2 + 2 \cos \Delta\phi) \left| \frac{2J_1(\frac{\pi\gamma}{2})}{\frac{\pi\gamma}{2}} \right|^2}{|2 + e^{j\Delta\phi} \frac{2J_1(\pi\gamma)}{\pi\gamma}|^2}. \quad (5.15)$$

The relationship between the intensity distribution and resolution coefficient  $\gamma$  and the phase difference  $\Delta\phi$  can be displayed as Fig. 5.2. One can find for  $\Delta\phi = 90^\circ$  the resolution is equal to that by using incoherent radiation illuminating, when  $90^\circ < \phi < 180^\circ$ , the resolution is better than the incoherent case. In principle, there is a limitation aroused by the detector sensitivity. In any practical system, the phase difference between

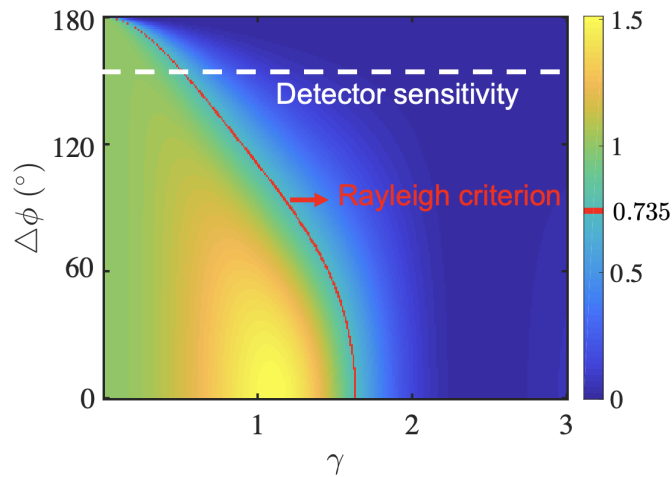


Figure 5.2: The resolution coefficient  $\gamma$  changes with the phase difference.

imaging points are defined by the object and effected by multiple factors, thus it is quite complicated to give the expression. Here, the 0 phase difference is taken for all the following calculations in this chapter.

It is worth mention that if the recording area is large enough ( $R_{max} \geq \frac{f}{d} \frac{D}{4}$ ),  $R_{max}$  should be substituted by  $R_{cut}$  (see Sec. 2.3.3), the resolution therefore will be expressed by

$$\delta = 1.64 \frac{\lambda d^2}{f D}, \quad (5.16)$$

where  $D$  is the aperture size of the focusing lens as defined in Sec. 2.3.3.

### 5.1.2 Lateral resolution of experimental results

To validate the lateral resolution of the imaging system, the experimental results of the USAF chart with Group -1 and 0 (see the panels highlighted by the blue, black and red dashed circles in Fig. 5.3) at 600 GHz are presented. The photo of the sample and the reconstructed images are shown in Fig. 5.3. The system is configured with parameters of 6-cm object distance and 6-cm focal length. From the result, one sees

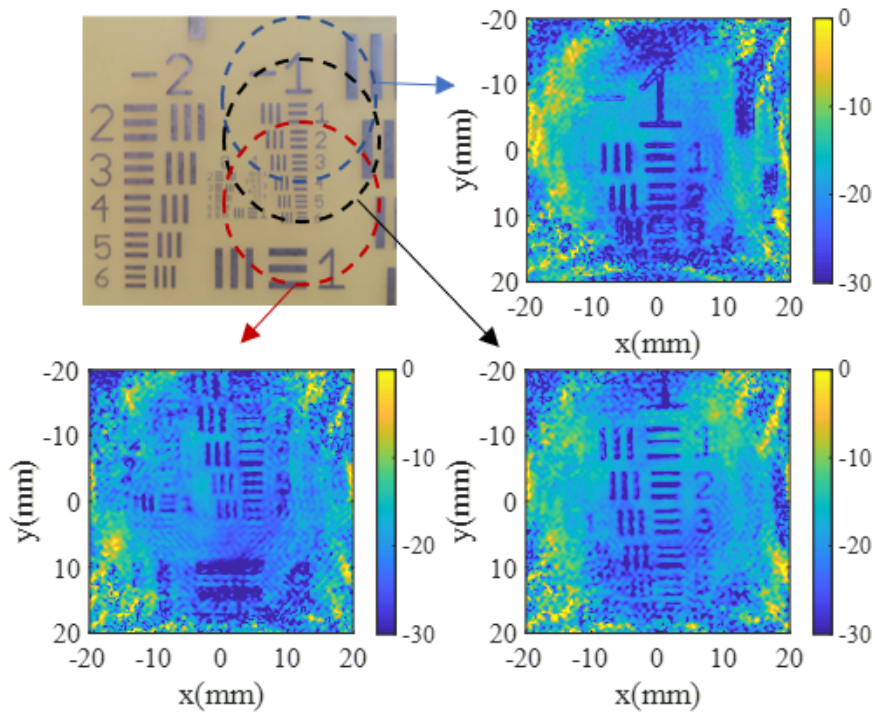


Figure 5.3: The imaging results of the USAF chart with Group -1 and 0 at 600 GHz. The plot in the upper left corner is the photo of the USAF chart, the other three plots are the imaging results corresponding to the sections marked by the dashed circles.

that the system can resolve the stripes of Group 0 No.1. Cutting the stripes in both vertical and lateral directions of Group 0 No.1, the 1D data can be extracted as depicted in Fig. 5.4 (the left and the right plots are cutting the stripes arranged in the vertical and lateral directions, respectively). Approximately 10 dB contrast of the 500  $\mu\text{m}$ -width

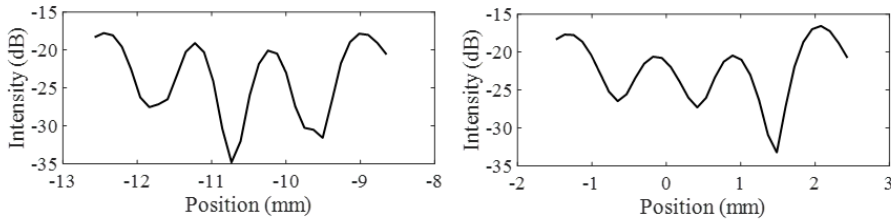


Figure 5.4: The one dimensional data be extracted from intensity stripes of Group 0 No.1. The left and right figures are the data cutting the stripes in vertical and lateral directions, respectively.

stripe displays a resolution of  $500 \mu m$  is reached by the system working with a 6-cm object distance, a 6-cm focal length and  $6 \times 6\text{-cm}^2$  scanning area. This is better than the 0 phase difference theoretical value derived by Eq. 5.13.

By using the same cutting way to extract the one dimension data of the phase imaging results, one can get the data presented by Fig. 5.5, which is another evidence of the resolution reaching  $500 \mu m$ .

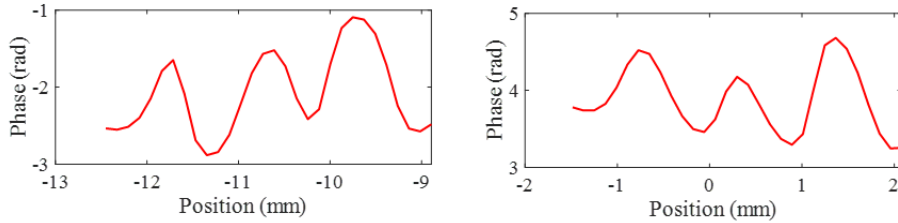


Figure 5.5: The one dimensional data be extracted from phase stripes of Group 0 No.1. The left and right figures are the data cutting the stripes in vertical and lateral directions, respectively.

To verify the resolution variation with the object distance, the imaged USAF chart is located at different positions from 6 cm to 9 cm with an interval of 1 cm. The generated Fourier spectrum for each case is displayed in Fig. 5.6. From the spectrum distribution, one will find out that, the larger object distance will squeeze the effective spectrum distribution area, which will lead to a resolution degrade. The top and bottom plots are intensity and phase Fourier spectra, respectively. From left to right the object distance changes from 6 cm to 9 cm. The reconstructed images based on the data are shown in Fig. 5.7. The top and bottom plots are intensity and phase images, respectively. From left to right the object distance changed from 6 cm to 9 cm. Cutting the stripes of Group

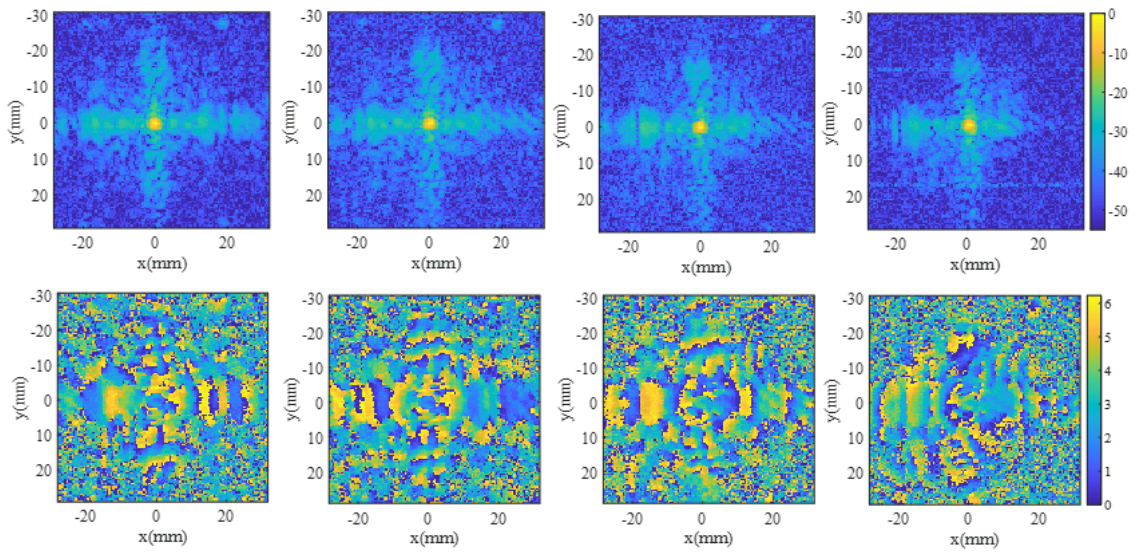


Figure 5.6: The generated Fourier spectrum of the imaged USAF chart located at from 6 cm to 9 cm with an interval of 1 cm. The top and bottom rows are intensity and phase spectrum, respectively. From left to right the object distance changed from 6 cm to 9 cm.

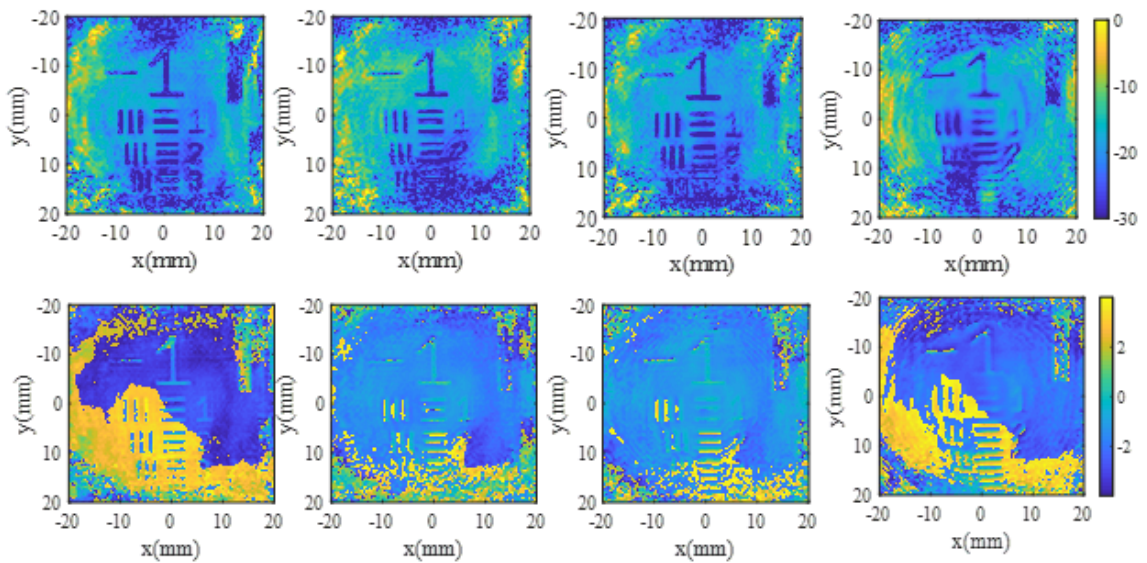


Figure 5.7: The reconstructed images of the USAF chart located from 6 cm to 9 cm with an interval of 1 cm. The top and bottom rows are intensity and phase spectrum, respectively. From left to right the object distance changed from 6 cm to 9 cm.

-1 No. 1 and 2 in both vertical and lateral directions generates the one dimensional data in Fig. 5.8. The plots in the top two rows and the bottom two rows are the data extracted from the intensity and the phase, respectively. The plots in the first and the third rows

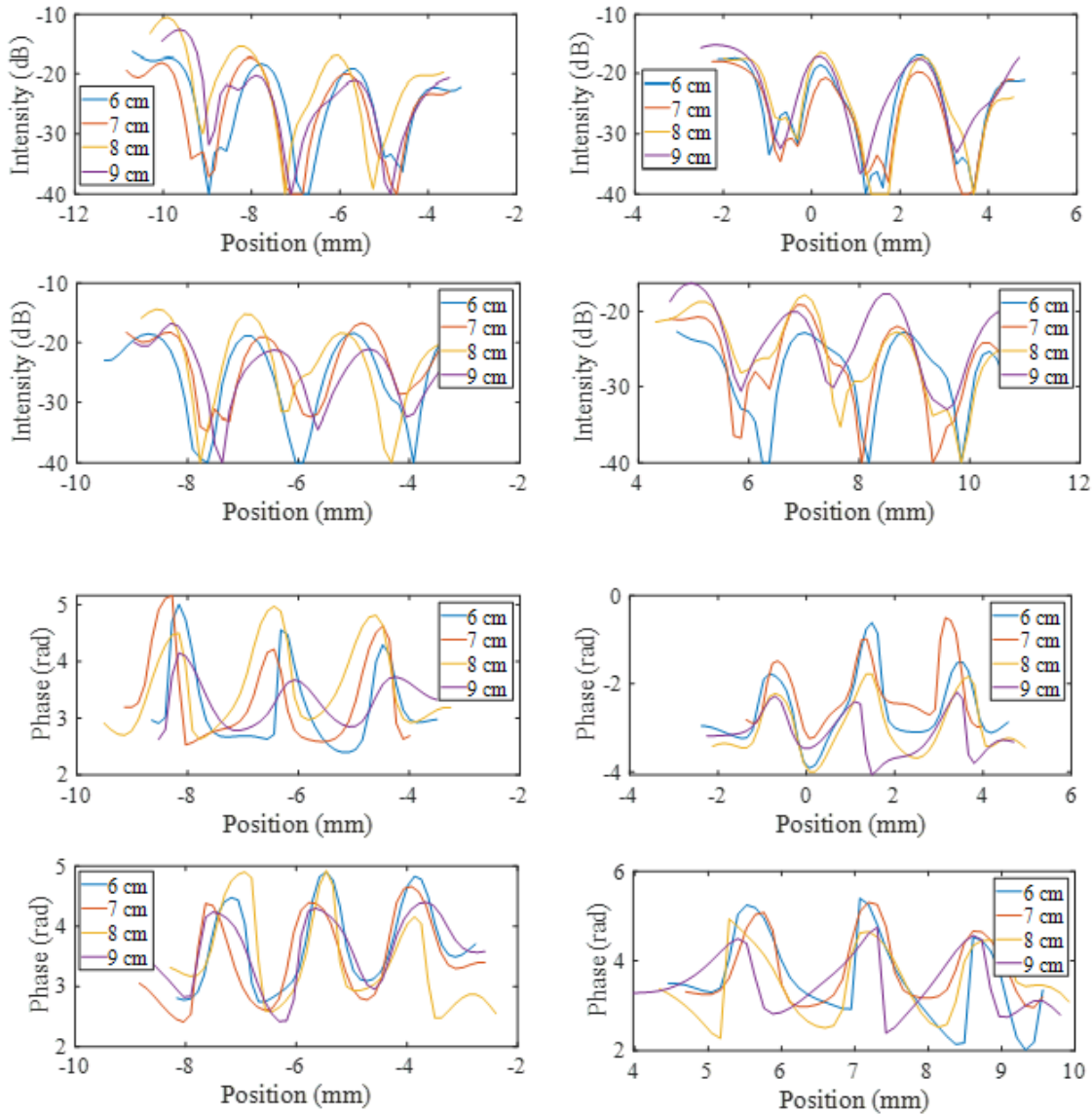


Figure 5.8: One dimension data cutting the stripes in vertical and lateral directions in Fig. 5.7. The two top rows and the two bottom rows are the data extracted from the intensity and the phase, respectively. The first and the third rows are the data of Group -1 No.1, the second and the last rows are the data of Group -1 No.2. The left and the right columns are the data cutting the stripes arranged in the vertical and lateral direction, respectively.

are the data of Group -1 No.1, the ones in the second and the last rows are the data of Group -1 No.2. The plots in the left and the right columns are the data cutting the stripes arranged in the vertical and lateral direction, respectively. The one dimensional

phase data are the unwrapped data.

Both the intensity and the phase data show that the smaller the object distance, the better contrast and resolution of the images will be, which is consistent with the derivation result of Eq. 5.13. Furthermore, the contrast of the phase reconstructed data is better than the intensity data reconstructed from the same spectrum. This is because of that phase is more sensitive than the intensity in Fourier spectrum.

## 5.2 Depth resolution of Fourier imaging setup

### 5.2.1 Depth resolution of Fourier imaging setup in principle

The depth resolution will be demonstrated based on the lateral resolution. The lateral resolution is adopted to calibrate the recognizable phase difference in the Fourier plane. Suppose one point shifts from the coordinate origin of the object plane to the  $\gamma\lambda d/D_{max}$  position (the minimum resolvable distance) on the lateral axis. The corresponding phase change is an additional tilt plane. The mathematical expression is

$$P_{add}(\delta) = e^{j2\pi f_\xi \delta} = e^{j2\pi \frac{x}{\lambda f} \delta}. \quad (5.17)$$

The phase change on the edge of the Fourier plane can be therefore expressed as

$$P_\delta = 2\pi \frac{R_{max}}{\lambda f} \delta = \gamma\pi \frac{d}{f}. \quad (5.18)$$

This is derived based on that  $\gamma$  meets the Rayleigh criterion, and presents that when the phase change at the edge of the detected area induced by the movement of the object or between two targets is larger than  $\gamma\pi d/f$ , it is resolvable. For the other case that the resolution is defined by the lens aperture  $D$ , the result keeps the same. Using it to substitute the depth resolution case, and assuming the phase change  $\Delta\psi = (\pi R_{max}^2 \cdot \Delta d)/(\lambda f^2)$  (according to Eq. 5.1) induced by the object movement of distance  $\Delta d$  in depth axis is larger than the minimum recognizable phase difference of  $P_\delta$ , the minimum

distinguishable object distance change in depth direction can be given by

$$\delta_d = \gamma \frac{\lambda df}{R_{max}^2}. \quad (5.19)$$

When phase difference between two points is 0, the minimum resolvable depth distance is  $1.64\lambda df/R_{max}^2$ . If the recording area in the Fourier plane is large enough, the resolution will be

$$\delta_d = 4\gamma \frac{\lambda d^3}{fD^2}. \quad (5.20)$$

For 0 phase difference case, the resolution is  $6.56\lambda d^3/(fD^2)$ . Based on the lateral resolution formulas Eq. 5.13 and 5.16, the depth resolution formulas Eq. 5.19 and 5.20, one will find the relationship between both resolutions can be written as  $\delta_d = \frac{4f}{D_{max}}\delta$  or  $\delta_d = \frac{4d}{D}\delta$  when the scanning area is not- or large enough, respectively. If we define  $\frac{f}{D_{max}}$  as the image space  $NA_i$  and  $\frac{d}{D}$  as the object space  $NA_o$  of the imaging system and take the smaller one as the NA (Numerical aperture,  $NA=\min(NA_i, NA_o)$ ) of the system, one can conclude that the depth resolution is  $4NA$  times of the lateral resolution.

### 5.2.2 Validation of depth resolution

The reconstructed intensity distribution of the bright point on axial direction will be presented here theoretically and experimentally. Normalizing the Fourier space by  $R' = r/R_{max}$  in Eq.5.6 and set  $\rho = 0$ , the axial PSF can be written as

$$H(\Delta d) = H(0, \Delta d) = 2\pi R_{max}^2 \int_0^1 e^{jkWR'^2} R' dR', \quad (5.21)$$

where  $W = \frac{R^2 \Delta d}{2f^2}$ , substituting  $x = R'^2$ ,  $dx = 2R' dR'$ , Eq. 5.21 will be

$$H(\Delta d) = \pi R_{max}^2 \int_0^1 e^{jkWx} dx, \quad (5.22)$$

According to  $\int e^{bx} dx = e^{bx}/b$  Eq. 5.22 will be

$$H(\Delta d) = \pi R_{max}^2 e^{jkWx} \Big|_0^1 = \pi R_{max}^2 \frac{e^{jkW} - 1}{jkW} = \pi R_{max}^2 [\sin(kW) - j(\cos(kW) - 1)]. \quad (5.23)$$

Then the axial intensity distribution will be

$$I(\Delta d) = H(\Delta d)H^*(\Delta d) = \pi R_{max}^2 \left[ \frac{\sin(\frac{kW}{2})}{\frac{kW}{2}} \right]^2 = \pi R_{max}^2 \text{sinc}^2\left(\frac{\pi W}{\lambda}\right). \quad (5.24)$$

Substituting  $\Delta d$  with the minimum resolvable distance  $\delta_d$  in Eq. 5.19. The corresponding  $W$  will be  $\gamma\lambda d/(2f)$ . For 0 phase difference case,  $W = 0.77\lambda d/f$ . Displaying two points' reconstructed intensity distribution on axial for this situation will be like Fig. 5.9. The parameter of the system is set as  $f = 6 \text{ cm}$ ,  $\lambda = 0.5 \text{ mm}$ , the first point object locates at distance  $d = 5 \text{ cm}$ , the second point object is  $\Delta d_{min} = 2.78 \text{ mm}$  away from the first point, the scanning area size in Fourier plane is  $6 \text{ cm} \times 6 \text{ cm}$ . From the figure, one sees the two peaks are resolvable under this definition.

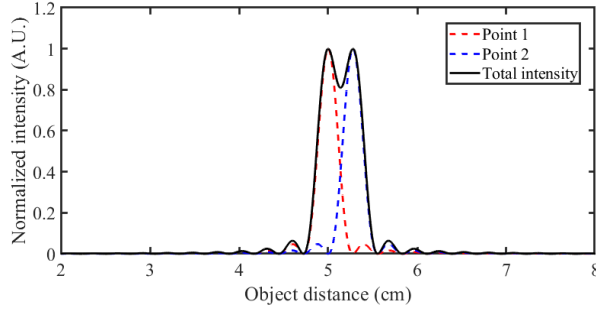


Figure 5.9: Reconstruction intensity distribution of the point objects along the axial direction of the imaging system.

### 5.2.3 Depth resolution of experimental results

The USAF chart imaging results at 600 GHz are again adopted to validate the depth resolution. In this section, the sharpness of the reconstructed image is used to identify the focused and unfocused status, and then to demonstrate the depth resolution. The reconstructed images of the 6-cm object distance Fourier spectrum under different calculated object distance are shown in Fig. 5.10, the plots in the top and bottom rows are the

intensity and phase reconstructed images, respectively, the plots in columns from left to right correspond to the reconstructed distance of 4 cm to 8 cm with 1 cm interval. For the sharpness calculation, the data reconstructed distance sweeps from 2 cm to 10 cm with a step of 1 mm. The sharpness of each image is derived based on the shape from focus method [97]. Fig. 5.11 depicts the sharpness change with the calculated object distance for the 6-cm object distance data. The sharpness is roughly distributed as a  $Sinc^2$  function, which proves Eq. 5.24. The arched baseline can be attributed to the aperture effect of the focusing lens in system or the cutting width of the scanning range in the Fourier plane.

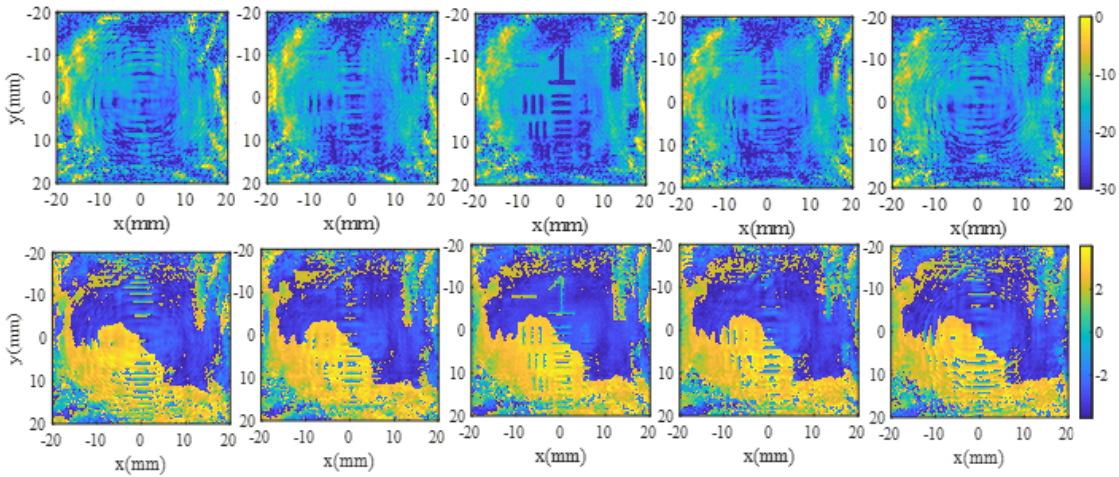


Figure 5.10: The reconstructed images of the 6 cm object distance data.

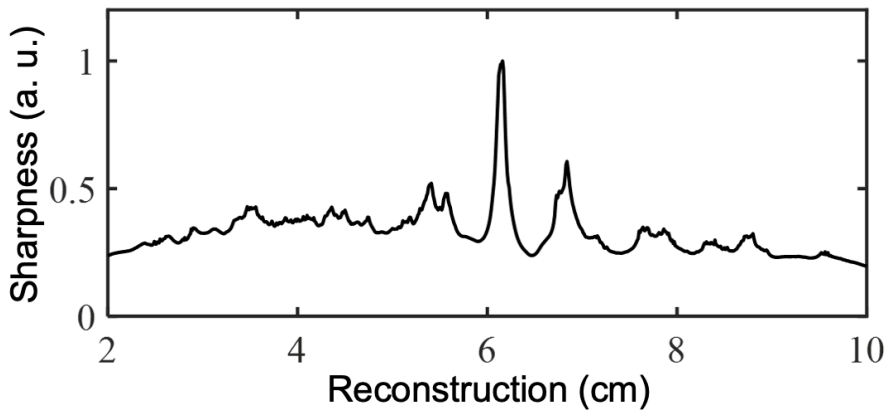


Figure 5.11: The sharpness distribution along the axial direction.

Including two objects (metal stripes glued on the PVC board) in the beam path of the system described as Fig. 5.12, the Fourier spectrum in Fig. 5.13 can be obtained. One object is composed of five 1-mm metal stripes with 1-mm interval and placed 5.4 cm in front of the focusing lens. The other is consist of three 1.5-mm metal stripes with 1.5-mm interval and set 6.9 cm in front of the focusing lens. The 1-mm stripes are arranged in vertical direction, the 1.5-mm stripes are arranged in lateral direction. The left and right figures in Fig. 5.13 are the intensity and phase spectrum, respectively.



Figure 5.12: The photos of two objects to be imaged. Left is the 1-mm-stripe-width object, right is the 1.5-mm-stripe-width object.

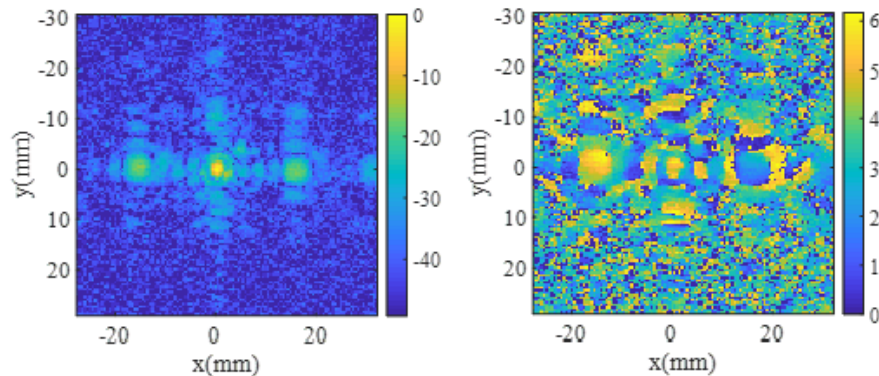


Figure 5.13: Fourier spectrum of the 1-mm and 1.5 mm metal stripes in the beam path at the same time. Left is the intensity spectrum, right is the phase spectrum.

Reconstructing the image with object distances from 2 cm to 10 cm and extracting the sharpness of each reconstructed image, one will find the sharpness of the reconstructed image changes with the calculated object distance explained by Fig. 5.14. Five peaks can be found in the figure. Taking the two main peaks' positions as the restore distance,

the images in Fig. 5.15 can be regenerated. The plots in the top and bottom rows are the reconstructed images of the 1-mm stripes and 1.5-mm stripes, respectively; the plots in the left column are the intensity images, the plots in the right column are the phase images. One can see, when the reconstruction is numerically focused on to the 5.4 cm object plane, the 1-mm metal stripes can be well resolved while the 1.5-mm metal stripes are blurred as a dark area; when focused onto the 6.9 cm object, the 1.5-mm metal stripes can be resolved (though not as good as the 1-mm stripes, this is because of the position, the 1-mm stripes are closer to the focusing lens.) but the 1-mm metal stripes image is out of focus.

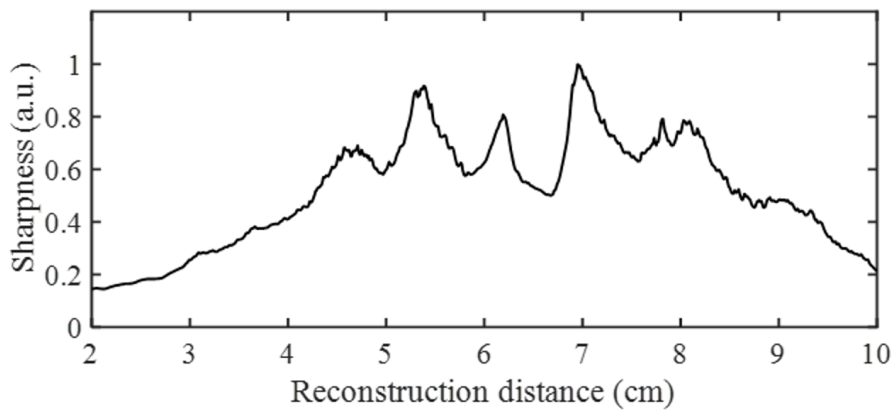


Figure 5.14: The sharpness distribution along the axial direction.

The two-objects imaging results show that 1.5 cm depth distance can be resolved. This is not as good as the estimation in theory because the illuminating radiation power is in the level of tens of  $\mu W$ , the system aperture size is limited and the aberrations of the imaging system are not corrected. An easy way to solve the problem is using a numerical algorithm to compensate [98]. This will be investigated in future.

## 5.3 Resolution of conventional microscopic imaging system

The role of the microscope is to magnify the microscopic world, so as to distinguish the details of microscopic objects. The invention and application of the microscope greatly

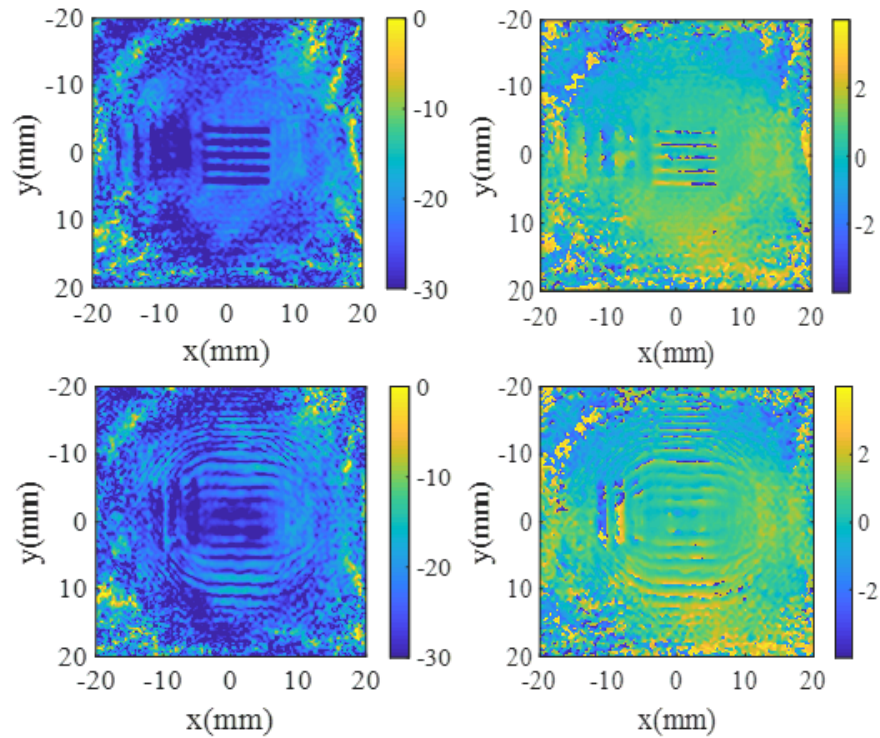


Figure 5.15: The sharpness distribution along the axial direction.

improved people's visual function and provided a powerful tool for people to study and understand the micro world. This section will analyze the resolution of the terahertz microscopic imaging system. The human eye is not sensitive to the terahertz waves, so the micro imaging system working in the terahertz band needs the detection originally working in the terahertz band to record the image and restore it for visualization. Due to the wavelength limitation, the resolution of the microscopic imaging system in THz band is not as good as that in the optical band. But due to the penetration and fingerprint property of the THz waves, microscopic imaging systems working at this range have wide application prospects in areas of biology, medicine, industry, etc . Fig. 5.16 displays a conventional microscopy imaging system. If one define that the minimum resolvable distance in the object space is  $\varepsilon$  and the corresponding angle in image space is  $\theta_0$ , the image height therefore is  $\varepsilon' = l'\theta_0$ . Associating this together with the optical invariant (the second formula in Eq. 5.25) in both object and image spaces, and the paraxial

approximation of sine function of the field of view in image space, one will get Eq. 5.25,

$$\begin{cases} \varepsilon' = l' \theta_0, \\ \varepsilon n \sin u = \varepsilon' n' \sin u', \\ \sin u' \approx u' = \frac{D/2}{l'}, \end{cases} \quad (5.25)$$

where  $D$  is the full aperture size,  $u$  is the field of view in object space,  $l'$  is the image distance,  $n$  and  $n'$  are the refractive index in the object space and image space, respectively, as shown in the left part of Fig. 5.16

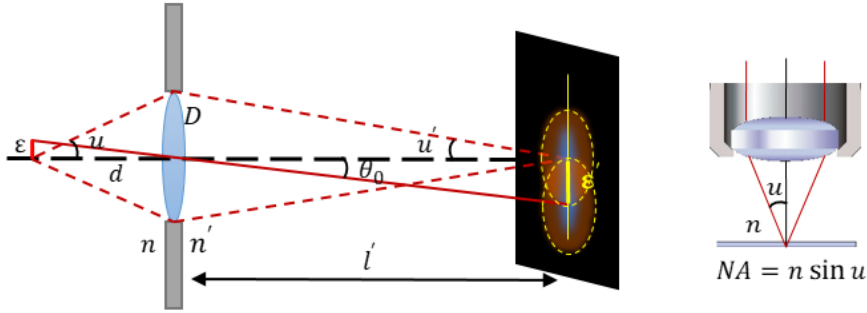


Figure 5.16: Microscopy imaging system.

Different from the microscopy in optical range, the illumination with continuous THz waves is coherent, thus the minimum resolvable angle  $\theta_0$  is defined by Eq. 5.13 as

$$\theta_0 = \gamma \frac{\lambda}{D} \quad (5.26)$$

Bringing Eq. 5.26 back to Eq. 5.25, the minimum resolvable distance in object space is

$$\varepsilon = \frac{\gamma}{2} \frac{\lambda}{n \sin(u)} = \frac{\gamma}{2} \frac{\lambda}{NA}, \quad (5.27)$$

where  $NA = n \sin(u)$  the numerical aperture in the object space as the right part in Fig. 5.16. For the worst case, it is  $0.77\lambda/NA$ . If the illumination is incoherent, the resolution is  $0.61\lambda/NA$ .

## 5.4 Comparison of the resolution of Fourier imaging system and conventional microscopic imaging system

### 5.4.1 Theoretical comparison

To compare the Fourier imaging and conventional microscopy imaging systems at THz frequencies, the expression of the resolution of both systems in Sections 5.2 and 5.3 needs to be rewritten in the same quantify rules from the most usual way as

$$\delta = \frac{\gamma\lambda\sqrt{D^2 + 4d^2}}{2nD}, \quad (5.28)$$

where  $D$  is the effective aperture of the imaging system and  $d$  is the object distance which is equal to the distance between the object and the aperture of the imaging system. Substituting  $nD/\sqrt{D^2 + 4d^2}$  by NA, Eq. 5.28 is the same as Eq. 5.27. Furthermore, using the paraxial approximation when  $d \gg D$ , and substitute  $n$  by 1, Eq. 5.28 will be transferred to  $\delta = \gamma\lambda d/D$ , which is the same as Eq. 5.13. From Eq. 5.28 it can be found that if one wants to improve the imaging resolution, one way is to increase the refractive index in the object space as the existed oil immersion microscopy. Another way is decreasing the object distance  $d$ . However, for microscopic imaging,  $d$  cannot be infinitely reduced. Since the refractive index can be changed for both systems, the following analysis will only focus on the discussion of reducing  $d$  and considering  $n$  with the value of 1 for all the discussion.

In THz band, where human eyes are not sensitive to the radiations, the image must be recorded by sensors working in this range. Therefore, for microscopic imaging the real image is necessary. According to the principle of optical imaging, to make an object into a real image, the object distance must be greater than the total focal length of the system. In other words,  $d \geq f$ , where  $f$  is the total focal length of the imaging system. Thus,

the best resolution of the microscopic imaging system is

$$\delta_{Mic} = \frac{\gamma\lambda\sqrt{D^2 + 4f^2}}{2D}. \quad (5.29)$$

While for Fourier imaging system, the image is reconstructed by back propagating the complex field recorded in the Fourier plane to the original object place, no matter where the object (even paraxial approximation is invalid). Thus the best resolution of Fourier imaging system (when the object distance approaches 0) with the same aperture, enough detection area for highest space frequency and total focal length is

$$\delta_{Fourier} = 0.5\gamma\lambda. \quad (5.30)$$

Comparing Eq. 5.29 and 5.30, one will find

$$\delta_{Fourier} < \delta_{Mic}, \quad (5.31)$$

which means the resolution can be reached by Fourier imaging system is better than that using the microscopic imaging system with the image target placed in the virtual image area ( $d < f$ ). In practice, if the object is too close to the imaging system, a phase fix factor needs to be included in the image reconstruction step since the field distribution in the Fourier plane is derived based on the paraxial approximation.

### 5.4.2 Experimental results comparison

By using the same focusing lens in the imaging system, the Fourier data and the microscopic plane-to-plane data of the Siemens star are recorded with 600-GHz illumination and 300-GHz LO. For both cases, the object distances are the same as 10 cm. To validate the resolution in a larger range, the Siemens star is set in the center and off the center of the beam path respectively for both imaging methods. Fig. 5.17 and 5.18 are Fourier imaging and microscopic imaging results, respectively. In both figures, the left and right columns are intensity and phase images, the top and bottom rows are the Siemens star in

the center and off the center images, respectively. Comparing the images, one will find

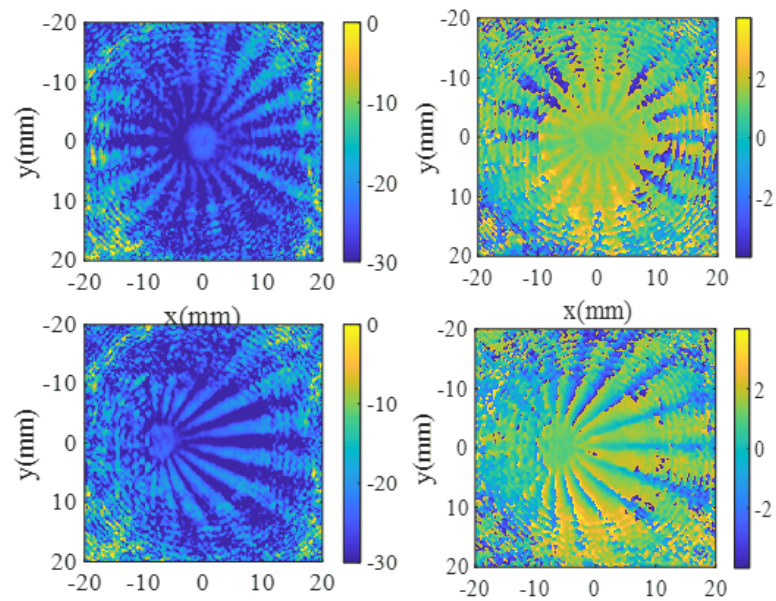


Figure 5.17: Reconstructed images of Siemens star at 600 GHz by using Fourier imaging method.

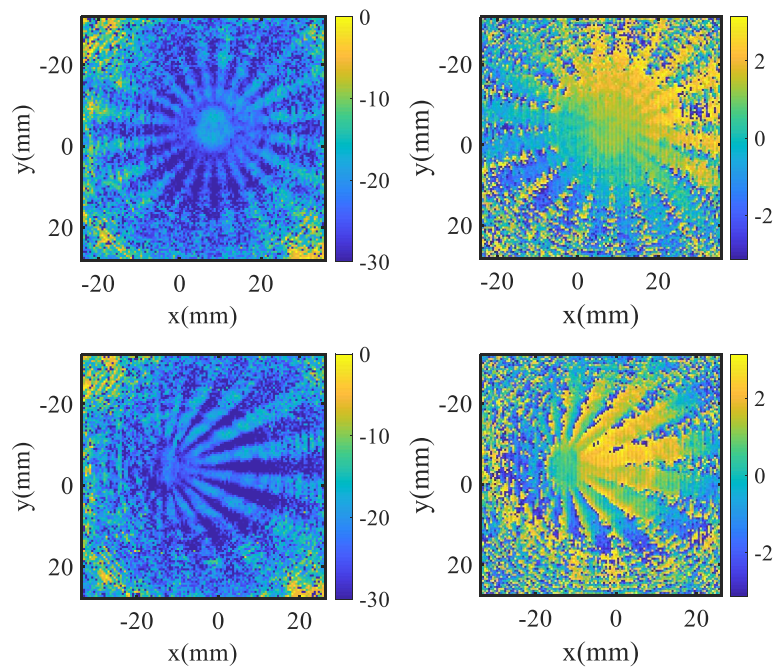


Figure 5.18: Images recorded by microscopy imaging system.

the dynamic range of Fourier imaging is comparable with that of microscopic imaging.

The sharpness of Fourier imaging is better than microscopic imaging since the background reduction in reconstruction in Fourier imaging includes the aberration reduction. The field of view (effective imaging area) of Fourier imaging is larger than the microscopic imaging (here the imaging result of the conventional plane-to-plane system needs to be shrank by 1.5 times to be compared with the Fourier images. The reason is that for plane-to-plane imaging with 6 cm focal length, the object distance of 10 cm generates an image distance of 15 cm; the image is hence to be enlarged 1.5 times.) Furthermore, the Fourier imaging method can shorten the object distance to values smaller than 6 cm, while the plane-to-plane imaging with pure power detection can not, thus the Fourier imaging is expected to improve the resolution better than microscopic imaging systems.

## 5.5 Conclusion

The lateral and depth resolution of the Fourier imaging system is demonstrated theoretically and experimentally. The lateral resolution is determined by the imaging object distance, the aperture of the focusing lens, the focal length of the focusing lens and the data recording range in the Fourier plane. Among all the parameters, the aperture of the focusing lens and the data recording range in the Fourier plane are in parallel, which is the crucial factor depending on the recording area is large enough or not. The larger the aperture/recording area and the shorter the object distance of the system are applied, the better lateral resolution will be reached. Of course the wavelength of the illuminating radiation is more important. Similar to the lateral resolution, the depth resolution also depends on the imaging object distance, the aperture of the focusing lens, the focal length of the focusing lens, and the data recording range in the Fourier plane. It is 4NA times of the lateral resolution.

The resolution of the microscopy imaging system is illustrated, and compared with Fourier imaging system under the same hardware conditions. The comparison shows that the Fourier imaging system is superior to microscopic imaging in sharpness, resolution, and field of view and it is comparable with microscopic imaging in its dynamic range.



## 6 Conclusion and Outlook

There have been many approaches in the realisation of THz imaging for various applications using different sources, detectors and techniques with advantages and disadvantages for each method [64, 99–106]. This work presents the Fourier imaging method at THz range. The THz Fourier imaging is realized by using fundamental and subharmonic heterodyne detection to record the Fourier spectrum and reconstruct the image by numerical calculations.

### 6.1 Conclusion

In summary, this work demonstrates the concept, simulation, accomplishment and the resolution of THz Fourier imaging. The simulations which are based on the wave propagation integral, are performed to study an electric field illuminating of an input object and its propagation to the focus plane. Numerical studies also help to predict properties, features and potential outcomes of an experimental measurements. Simulations figured out the idea of the paring between the objects and the characteristic intensity and phase patterns. Numerical calculations also help to predict the impact of noisy intensity and phase on the back-calculation. Different objects result in different Fourier spectra with the highlighted spacial frequencies of the object features.

Two electrical multiplier chain THz sources are used in a heterodyne configuration to enable phase-sensitive detection of a TeraFET detector for the first time. Simple input objects like a metal grid, a USAF chart and a Siemens-star test chart are recognizable and the predicted depth sensitivity is demonstrated. Corresponding measurements with a grid, a Siemens-star and a USAF chart objects were performed achieving the predicted

lateral resolution and depth sensitivity for numerical focusing. The retrieved input of the object is in a high correlation with the numeric prediction (see section 2.3.1), making it easy to distinguish between the objects. Multiple objects in the beam path prove to be challenging for the presented set-up in the current research. Nevertheless, heterodyne detection enables one to capture a 3D scene by numerical focusing on different depths by taking one set of data.

The Fourier imaging system is proved at 300 GHz and 600 GHz. Fundamental heterodyne detection is adopted at 300 GHz, while at 600 GHz, the fundamental heterodyne detection loses its appeal attributed to the higher cost and lower power. To solve the problem, the sub-harmonic detection is employed to achieve Fourier imaging at 600 GHz. The efforts to enhance the coupling efficiency of the LO is realized by integrating the wax/PTFE substrate lens, which improved the coupling efficiency of LO by approximately 10 dB and dynamic range by 20 dB. This makes the sub-harmonic detection feasible for the Fourier imaging setup.

The resolution of the Fourier imaging system is slightly better than that of the microscopy imaging system with the same optical elements and system arrangement. Under this condition, the Fourier imaging system performed by the sub-harmonic heterodyne detection nearly reached the resolution limitation with the value equal to the wavelength of  $500 \mu\text{m}$ .

## 6.2 Outlook

The lateral resolution is currently restricted by the scanning range/aperture of the system. To increase the resolution of the retrieved input, future experiments have to increase the range in  $k$  space. This can either be achieved by increasing the travel of the translation stages based on higher sensitivity of the detector or by lowering the focus length. As mentioned before, coherent reflections change the phase in the Fourier plane and therefore have a high impact on the quality of the reconstruction, especially with two substrate lenses on both sides of the detector. Isolating elements with low insertion loss have to be used carefully in order to shorten the coherent length but not destroy the phase

behaviour of the Fourier spectrum. This will contribute to the reduction of standing waves in succeeding experiments. To make use of the measurement's resolution in the Fourier plane, the field of view has to be broadened in the Fourier setup and filter the THz beam so that the object is illuminated with a homogeneous intensity distribution instead of a Gaussian one. Using the current setup, there is no estimation on how precise the phase curvature was measured and therefore how depth-sensitive the measurements are. In conclusion, this study realized the potential of THz sources for applications in imaging and spectroscopy.



# List of Figures

1.1	Typical output power of various THz sources as a function of frequency . . . . .	3
2.1	Sketch of Fourier imaging . . . . .	6
2.2	Schematic of Hugens-Fresnel . . . . .	7
2.3	Schematic of Hugens description of spherical and plane wave propagationsl . . . . .	8
2.4	Schematic of the spherical diffraction . . . . .	8
2.5	Schematic of the diffraction . . . . .	10
2.6	Model of Fresnel diffraction . . . . .	11
2.7	Model of thin lens . . . . .	13
2.8	Plane wave illumination diffraction device . . . . .	15
2.9	Fourier transform beam path with object in front of lens . . . . .	18
2.10	Phase simulation of Fourier imaging . . . . .	20
2.11	Generic Fourier imaging approach. . . . .	21
2.12	Imaging field of view comparison . . . . .	23
2.13	Typical 4-f imaging system . . . . .	24
2.14	Photo of USAF chart test target . . . . .	27
2.15	Simulation of Fourier spectrum of three different parts of the USAF chart . . . . .	29
2.16	The reconstructions of each image targets in Fig. 2.15 . . . . .	30
2.17	Simulation of Fourier spectrum of two different parts of the USAF chart target . . . . .	31
2.18	The reconstructions of each image targets in Fig. 2.17 . . . . .	31
2.19	Photo of Siemens star test target . . . . .	32
2.20	Simulation of Fourier spectrum of Siemens star at 300 GHz . . . . .	33

2.21	The reconstructed imaging results of the Siemens star at 300 GHz . . . . .	33
2.22	Simulation of Fourier spectrum of Siemens star at 600 GHz . . . . .	34
2.23	The reconstructed imaging results of the Siemens star at 600 GHz . . . . .	34
2.24	Photo of 2D grid test target . . . . .	35
2.25	Simulation of Fourier spectrum of 2D metal grid at 300 GHz . . . . .	36
2.26	The reconstructed imaging results of the 2D grid at 300 GHz . . . . .	36
2.27	Simulation of Fourier spectrum of the 2D grid at 300 GHz . . . . .	37
2.28	The reconstructed imaging results of the 2D grid at 600 GHz . . . . .	37
2.29	The simulation of the USAF resolution chart for different pixel pitch and recording range . . . . .	38
3.1	Schematic of the Fourier imaging system at 300 GHz . . . . .	44
3.2	Imaging result of the metal grid at 300 GHz . . . . .	47
3.3	Imaging result of the USAF chart at 300 GHz . . . . .	48
3.4	Photo of the Siemens star . . . . .	49
3.5	Imaging results of the Siemens star . . . . .	50
3.6	One dimensional resolution data of the Siemens star . . . . .	51
3.7	Imaging results of the washer and screw . . . . .	53
4.1	Response of direct and sub-harmonic detection . . . . .	58
4.2	I-V response of the detector response with $\pm 0.01$ V. . . . .	59
4.3	Detector response with 12-mm diameter Si lens . . . . .	60
4.4	Detector response at 300 GHz ( $600\text{-}\mu W$ output power) with 8-mm diameter wax/PTFE lens and at 600 GHz ( $56\text{-}\mu W$ output power) with 4-mm diameter Si lens . . . . .	61
4.5	Sub-harmonic response of the detector with 4-mm diameter Si lens . . . . .	63
4.6	Schematic of Fourier imaging system based on sub-harmonic detection . . . . .	66
4.7	Photo of the wax material . . . . .	67
4.8	Transmission THz pulse with and without paraffin wax material . . . . .	68
4.9	The Fourier transform spectrum of the reference pulse and the test pulses of the samples . . . . .	68

4.10	The transmission rate and the phase delay of paraffin wax at each frequency	69
4.11	Refractive index of the paraffin wax at THz range . . . . .	70
4.12	Absorption and extinct coefficient of paraffin wax with frequency . . . . .	70
4.13	Permittivity of the paraffin wax at THz range . . . . .	71
4.14	Schematic of the integration of the wax/PTFE lens on the detector . . . . .	72
4.15	Schematic of the light refraction in wax/PTFE lens . . . . .	73
4.16	Schematic of the LO injection non- and through paraffin wax onto the detector . . . . .	74
4.17	Sub-harmonic response of the detector with 4-mm diameter Si lens . . . . .	75
4.18	Sub-harmonic response of the detector with 4-mm diameter Si lens . . . . .	76
4.19	Fourier spectrum of the Siemens star under sub-harmonic detection at 600 GHz . . . . .	78
4.20	The reconstructed imaging results of the data in Fig. 4.19 . . . . .	79
4.21	One dimensional resolution data of the Siemens star images . . . . .	80
4.22	Imaging results of USAF resolution chart at 600 GHz . . . . .	80
5.1	The intensity distribution of the middle place for two points with 0 phase difference . . . . .	84
5.2	The resolution coefficient $\gamma$ change with the phase difference . . . . .	85
5.3	The imaging results of the USAF chart with Group -1 and 0 at 600 GHz . . . . .	86
5.4	The one dimensional data extracted from intensity stripes of Group 0 No.1 . . . . .	87
5.5	The one dimensional data extracted from phase stripes of Group 0 No.1 . . . . .	87
5.6	The generated Fourier spectrum of the imaged USAF chart located at different positions from 6 cm to 9 cm . . . . .	88
5.7	The reconstructed images of the USAF chart located from 6 cm to 9 cm . . . . .	88
5.8	Fourier transform light path with object in front of lens. . . . .	89
5.9	Reconstruction intensity distribution of the point objects along the axial . . . . .	92
5.10	The reconstructed images of the 6 cm object distance data . . . . .	93
5.11	The sharpness distribution along the axial direction . . . . .	93
5.12	The photos of two objects to be imaged . . . . .	94

5.13	The sharpness distribution along the axial direction . . . . .	94
5.14	The sharpness distribution along the axial direction . . . . .	95
5.15	The sharpness distribution along the axial direction . . . . .	96
5.16	Microscopy imaging system . . . . .	97
5.17	Reconstructed images of Siemens star at 600 GHz by using Fourier imaging method . . . . .	100
5.18	Images recorded by microscopy imaging system . . . . .	100
A.1	The complex Fourier spectrum of two samples at 300 GHz . . . . .	113
A.2	The complex Fourier spectrum of USAF chart at 300 GHz . . . . .	114
A.3	The complex Fourier spectrum of Siemens star at 300 GHz . . . . .	115
A.4	The complex Fourier spectrum of USAF chart recorded by sub-harmonic detection at 600 GHz . . . . .	116
A.5	The complex Fourier spectrum of Siemens star in and off center at 600 GHz	116
A.6	The complex Fourier spectrum of different USAF chart parts at 600 GHz	117
A.7	The output power of the 300 GHz radiation . . . . .	118
A.8	The output power of the 300 GHz radiation . . . . .	118
B.1	Fourier transform light path with object in front of lens. . . . .	120
B.2	Fourier transform light path with object in front of lens. . . . .	121
B.3	Fourier transform light path with object in front of lens. . . . .	122
B.4	Fourier transform light path with object in front of lens. . . . .	124
B.5	Fourier transform light path with object in front of lens. . . . .	125
B.6	Fourier transform light path with object in front of lens. . . . .	126
B.7	Fourier transform light path with object in front of lens. . . . .	127
B.8	The reconstructed images of the USAF chart by using object distance from 2 cm to 10 cm . . . . .	128
B.9	The sharpness change of the reconstructed images along with the object distance variation . . . . .	129

# Appendices



# A Complementary Figures

The appendices include some additional materials that not suitable in the continuous text but still interesting enough for the reader's consideration.

## A.1 Fourier spectrum

Section 3.2.1 addresses the reconstructed images of the Fourier imaging at 300 GHz. Here the original recorded Fourier spectrum of the imaging results will be displayed. Fig. A.1 depicts the Fourier spectrum of the samples in Fig. 3.7. The input of the reconstruction process is complex data.

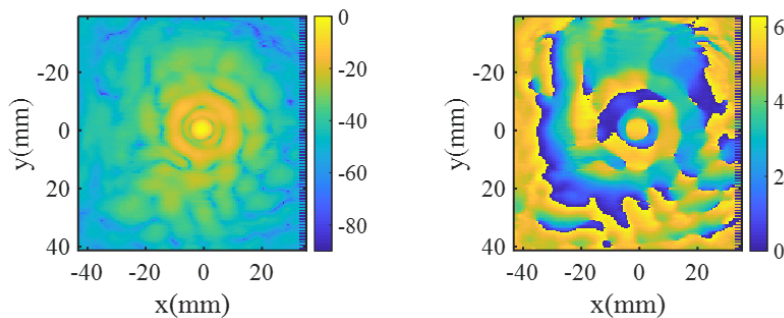


Figure A.1: The Fourier spectrum of the washer and screw in Fig. 3.7. The left and right figures are intensity and phase spectrum, respectively. The corresponding units of the color bars are dB and rad.

Fig. A.2 shows the complex Fourier spectrum of Fig.3.3, rows from top to bottom correspond to the reconstructed images in Fig. (b) to (d).

Fig. A.3 are the complex Fourier spectrum of Siemens star at different object distances in Fig. 3.5.

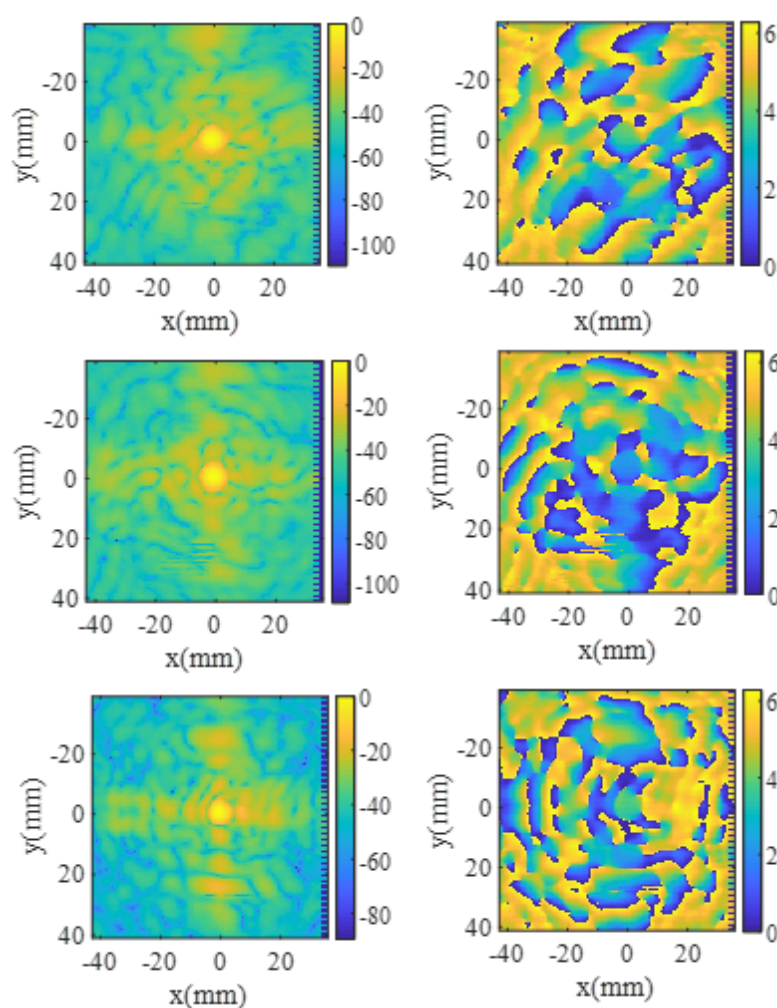


Figure A.2: The complex Fourier spectrum of assorted USAF board parts in Fig.3.3, rows from top to bottom correspond to sub figure (b) to (d), left and right columns are intensity and phase, respectively. The corresponding units of the color bars are dB and rad.

Section 4.4 and 5.1.2 illustrate the Fourier imaging results at 600 GHz. In the following text, the Fourier spectrum recorded by sub-harmonic detection based on 600 GHz radiation will be presented. Fig. A.4 demonstrates the Fourier spectrum of the images in Fig.4.22. Fig. A.5 illustrates the Fourier spectrum of the results in Fig.5.17. Fig. A.6 describes the Fourier spectrum of the reconstructed targets in Fig.5.3. The correspondences between the figures are described in the captions.

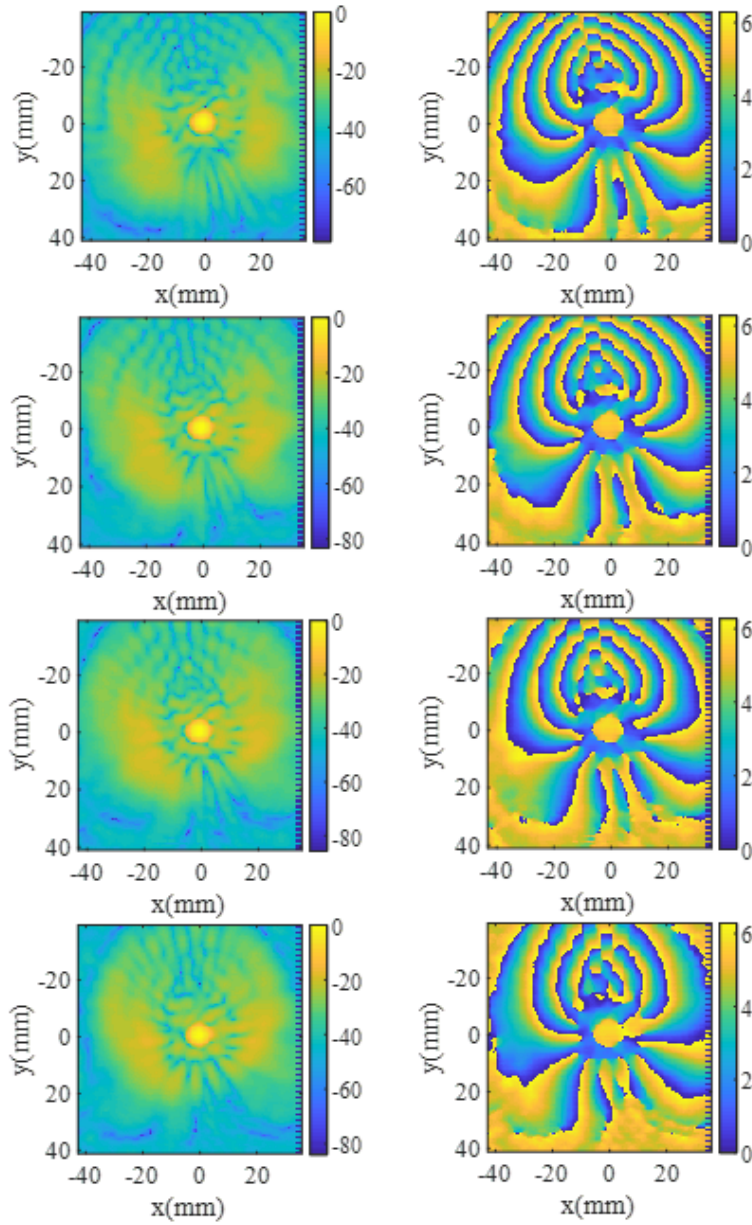


Figure A.3: The complex Fourier spectrum of Siemens star at different object distances in Fig. 3.5. The rows from top to bottom display the spectrum of object distances from 9 cm to 12 cm with 1 cm interval, the left and right columns are intensity and phase spectrum, respectively. The corresponding units of the color bars are dB and rad.

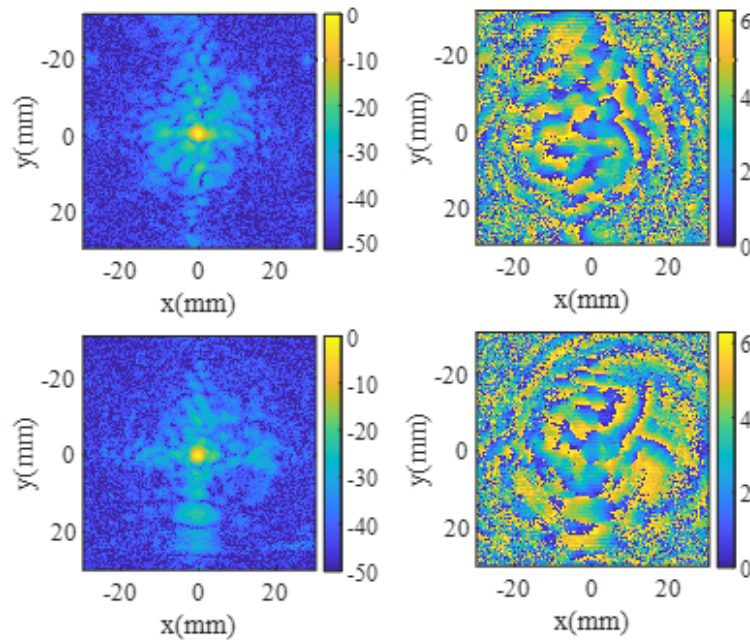


Figure A.4: The Fourier spectrum of Fig. 4.22. Top and bottom rows present the Fourier spectrum of the part with number -2 and -1, respectively, the left and right columns are intensity and phase spectrum, respectively. The corresponding units of the color bars are dB and rad.

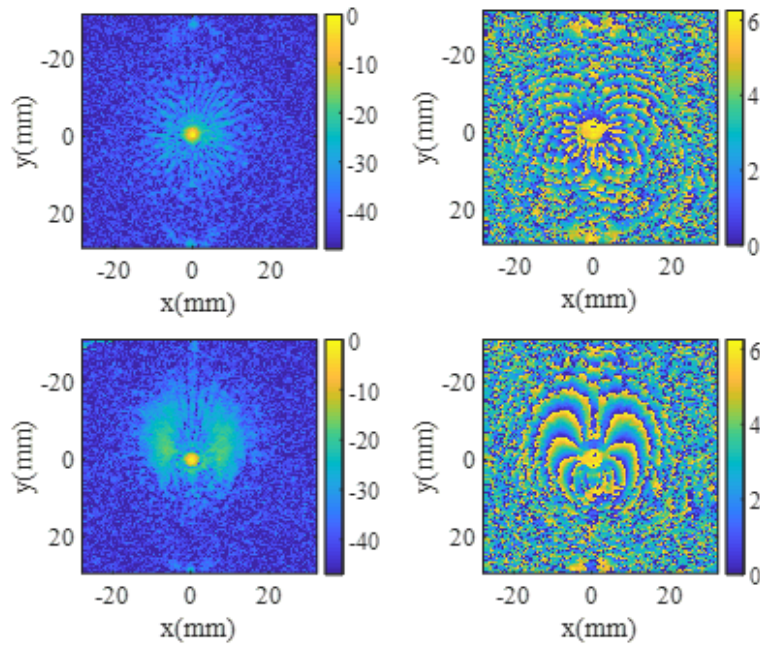


Figure A.5: The Fourier spectrum of Fig. 5.17. The top and bottom rows show the Fourier spectrum of the in and off the center, respectively, the left and right columns are intensity and phase spectrum, respectively. The corresponding units of the color bars are dB and rad.

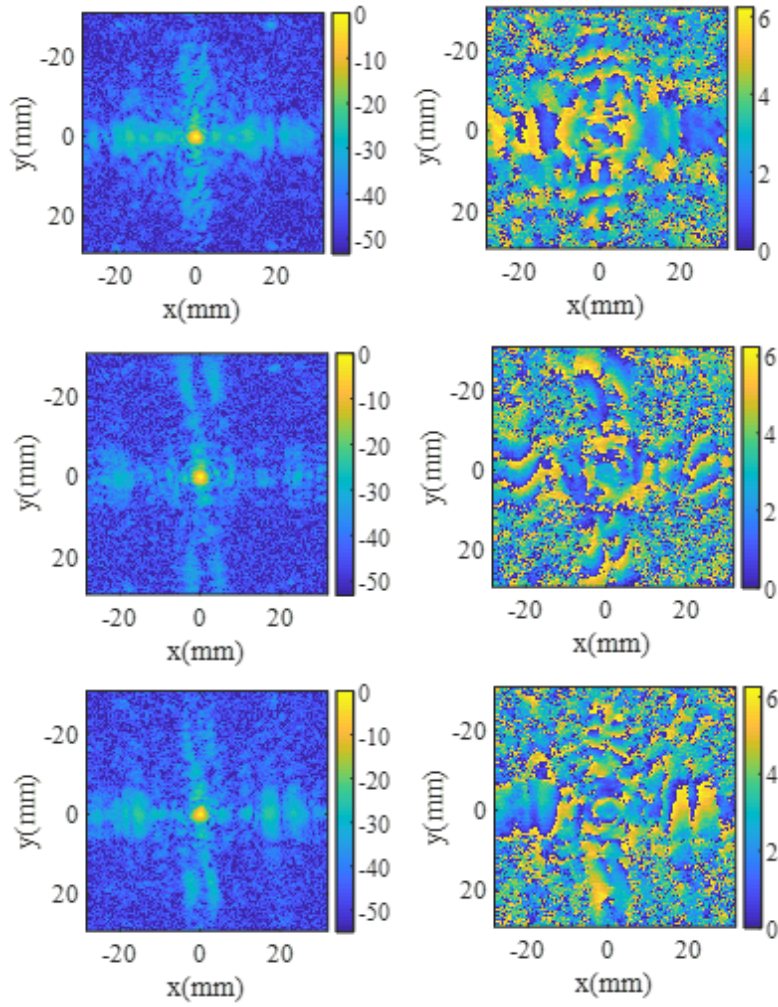


Figure A.6: The Fourier spectrum of Fig. 5.3. The rows from top to bottom present the Fourier spectrum of the upper right corner, bottom left corner and bottom right corner sub figures in Fig. 5.3, respectively, the left and right columns are intensity and phase spectrum, respectively. The corresponding units of the color bars are dB and rad.

## A.2 Power of 300 GHz and 600 GHz radiation

As an interesting test to demonstrate the dynamic range, the power of the illuminating radiation of 300 GHz and 600 GHz is measured by Topathkeating. Fig.A.7 is the output power of the RPG multiplier chain at 234-360 GHz, from which one can find the power at 300 GHz is approximate 1 m W. Fig.A.8 is the output power of the RPG multiplier chain at 500-720 GHz, where the power of 56  $\mu$ W will be found.

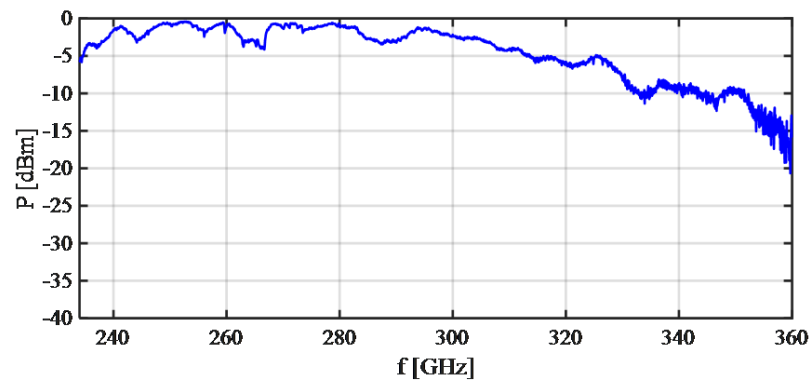


Figure A.7: The output power of the RPG multiplier chain at 234-360 GHz.

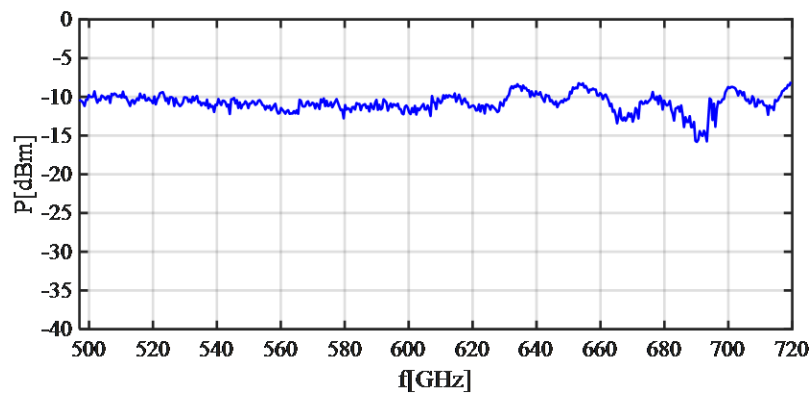


Figure A.8: The output power of the RPG multiplier chain at 500-720 GHz.

# B Imaging resolution simulation

## B.1 Lateral resolution simulation

To provide a comparison standard for the lateral resolution imaging results, the simulation of a USAF chart with Group -1, No. 1,2 and 3 parts (see the panel highlighted by the purple dashed circle in Fig. 2.14) at 600 GHz will be presented. The imaged target is located at the object distance of 6 cm to 10 cm with an interval of 1 cm for focal length of 6 cm to 10 cm with the same interval. The generated Fourier spectra for each case are displayed in Fig. B.1. The spectra for the focal length from 6 cm to 10 cm are displayed in the descending order. The figures in the first column are the intensity spectra for different focal lengths. The focus spot size is directly proportional to the focal length. Since the object distance shift has nearly no influence on the intensity distribution of the Fourier spectrum, only one intensity spectrum is presented for each focal length. The figures in the second to the last column are the phase spectra for the object distances from 6 cm to 10 cm. It can be summarized from the results of phase distribution that the larger object distance will squeeze the effective phase distribution area smaller, which will leads to a resolution degeneration.

Fig. B.2 is the reconstructed intensity images from the Fourier-spectrum matrix in Fig. B.1. The images show that the closer the object is from the focusing lens, the better contrast and resolution of the images will be obtained, which is consistent with the derivation of Eq. 5.13. Furthermore, the focal length will not affect the contrast and the resolution since the Fourier data recording area is large enough to include all the diffraction patterns. Fig. B.3 illustrates the reconstructed phase images from the Fourier-spectrum matrix in Fig. B.1. The changing trend of contrast and resolution of

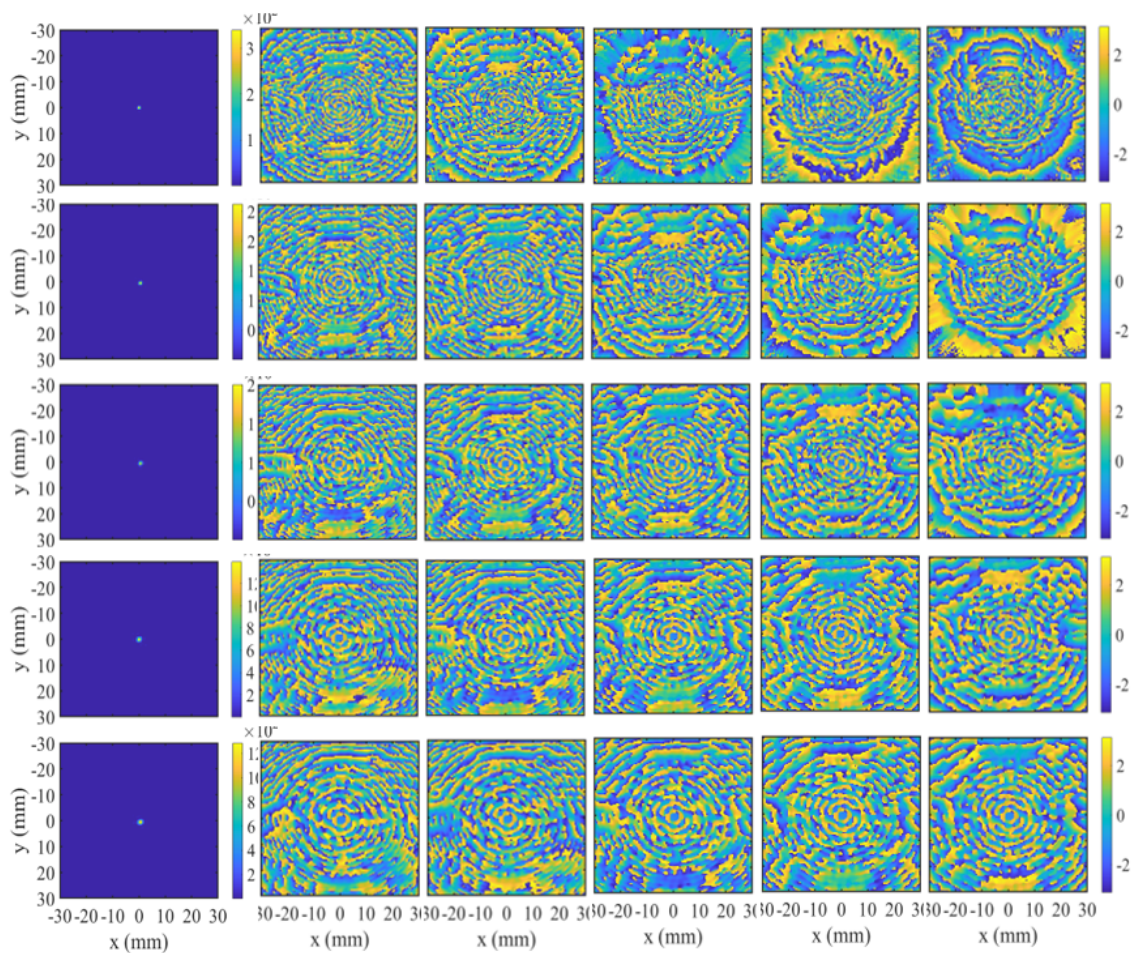


Figure B.1: Fourier spectrum simulations under different focal lengths and object distances at 600 GHz. From top to bottom rows are the Fourier spectrum generated with the focal length from 6 cm to 10 cm having 1 cm has interval. The first column is the intensity Fourier spectrum. From the second to the last column are the phase Fourier spectrum under the object distances from 6 cm to 10 cm with 1 cm interval.

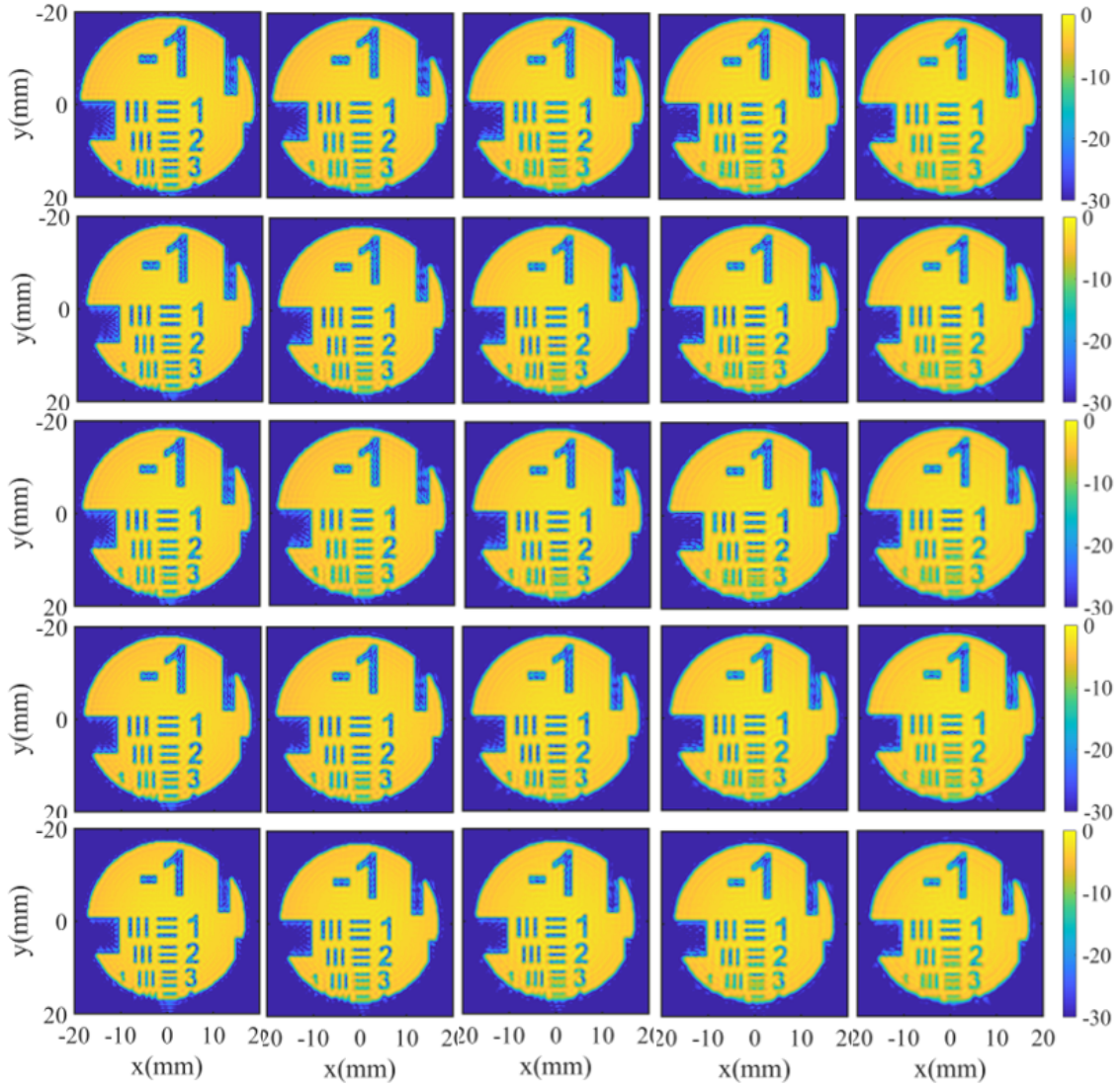


Figure B.2: The reconstructed intensity images based on the Fourier spectrum matrix in Fig. B.1. The spectrum for the focal length from 6 cm to 10 cm is displayed in the descending order.

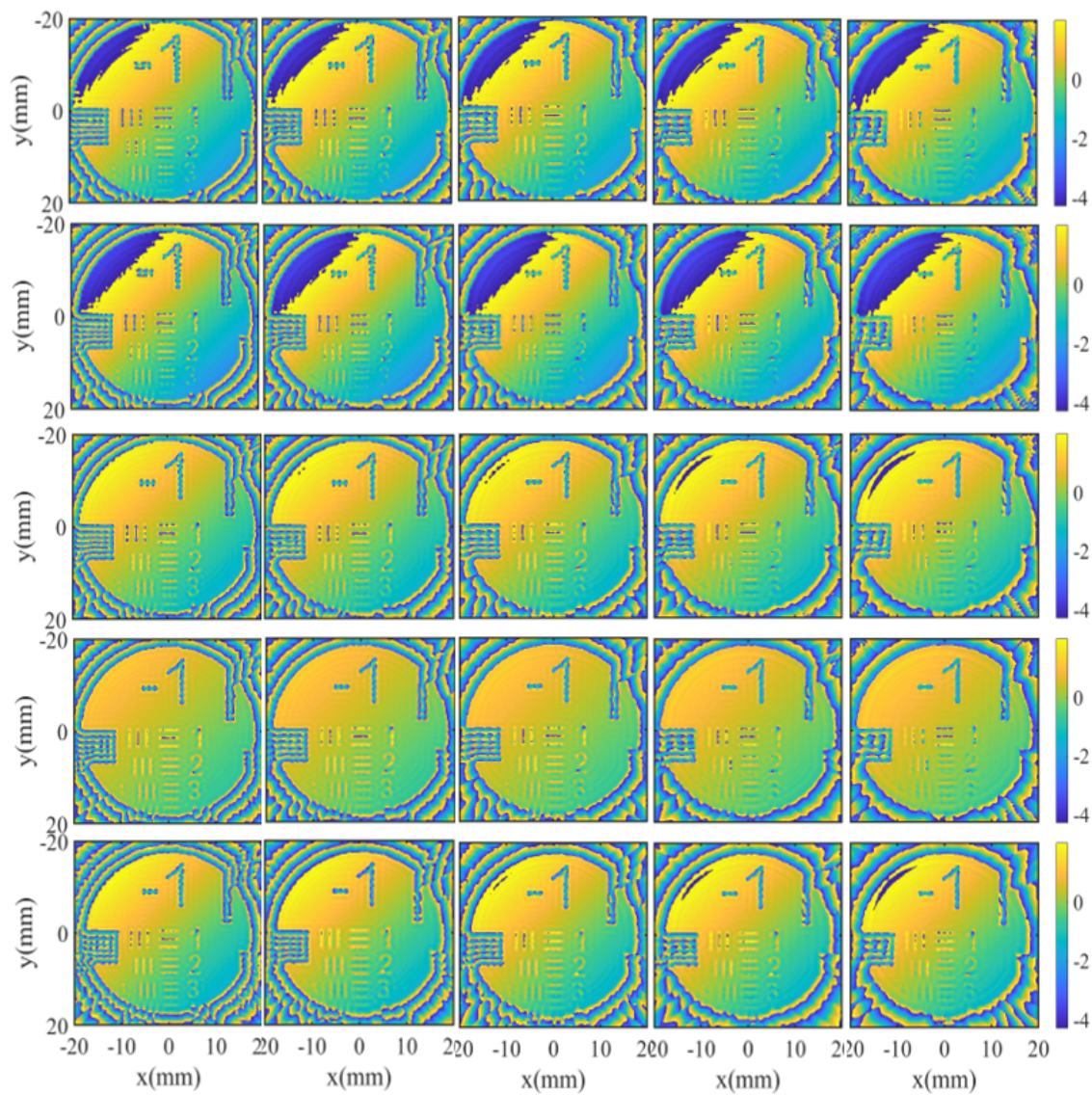


Figure B.3: The reconstructed phase images based on the Fourier spectrum matrix in Fig. B.1, from top to bottom rows and left to right columns correspond to 6 cm to 10 cm focal length and 6 cm to 10 cm object distances, respectively.

the phase images with the object distance is the same as the intensity images. What's more the phase is more sensitive and shows a better contrast and resolution than the intensity images. The background in the whole image area of the phase images is not unity but shows a tilted plane. This is because the illuminating Gaussian beam is not exactly located in the central position, which in turn transfers to a phase factor behaving as a tilted plane after the inverse Fourier transform.

To compare the contrast and resolution of the images more intuitively, the one dimensional data of the stripes in each elements of Group -1 on the USAF chart are extracted by going through the stripes. Fig. B.4 displays the extracted data cutting through the stripes in vertical directions of Number 1 to 3 elements in Fig. B.3. Rows from top to bottom correspond to 6 cm to 10 cm focal length, left to right column correspond to elements Number 1 to 3 (Number 1, 2 and 3 has the stripe width of 1 mm, 0.89mm, and 0.79 mm). Fig. B.5 shows the extracted data of the stripes in lateral directions of elements Number 1 to 3 in Fig. B.3. From top to bottom, rows correspond to 6-cm to 10-cm focal length, left to right column correspond to elements Number 1 to 3, blue, red, yellow, purple and green color present 6-cm to 10-cm object distance for each focal length system. All of the sub-figures show that a shorter object distance will generate a better resolution. The Figs B.7, B.6, B.5 and B.4 tell us that the resolution and contrast in the lateral direction (expressed by the data cutting the vertical arranged stripes) is better than that in the vertical direction (expressed by the data cutting the lateral arranged stripes). This can be attribute to the polarization of the illuminating radiation. The resolution in the lateral direction can reach 0.79 mm for all of the object distances. While in the vertical direction, the resolution of the 10-cm object distance can just reach 0.89 mm.

Fig. B.6 and Fig. B.7 exhibit the one dimensional data extracted from the phase images. They are achieved by expanding the data on the line going through the the stripes of the elements Number 1 to 3 in Fig. B.3 in vertical and lateral directions, respectively. The resolution varies with the same tend as the intensity data that shorter object distance generates better resolution. While with the same object distance, the contrast of each group is better than the intensity images, the phase data show a better resolution than 0.79 mm both in the vertical and lateral direction, which is better than

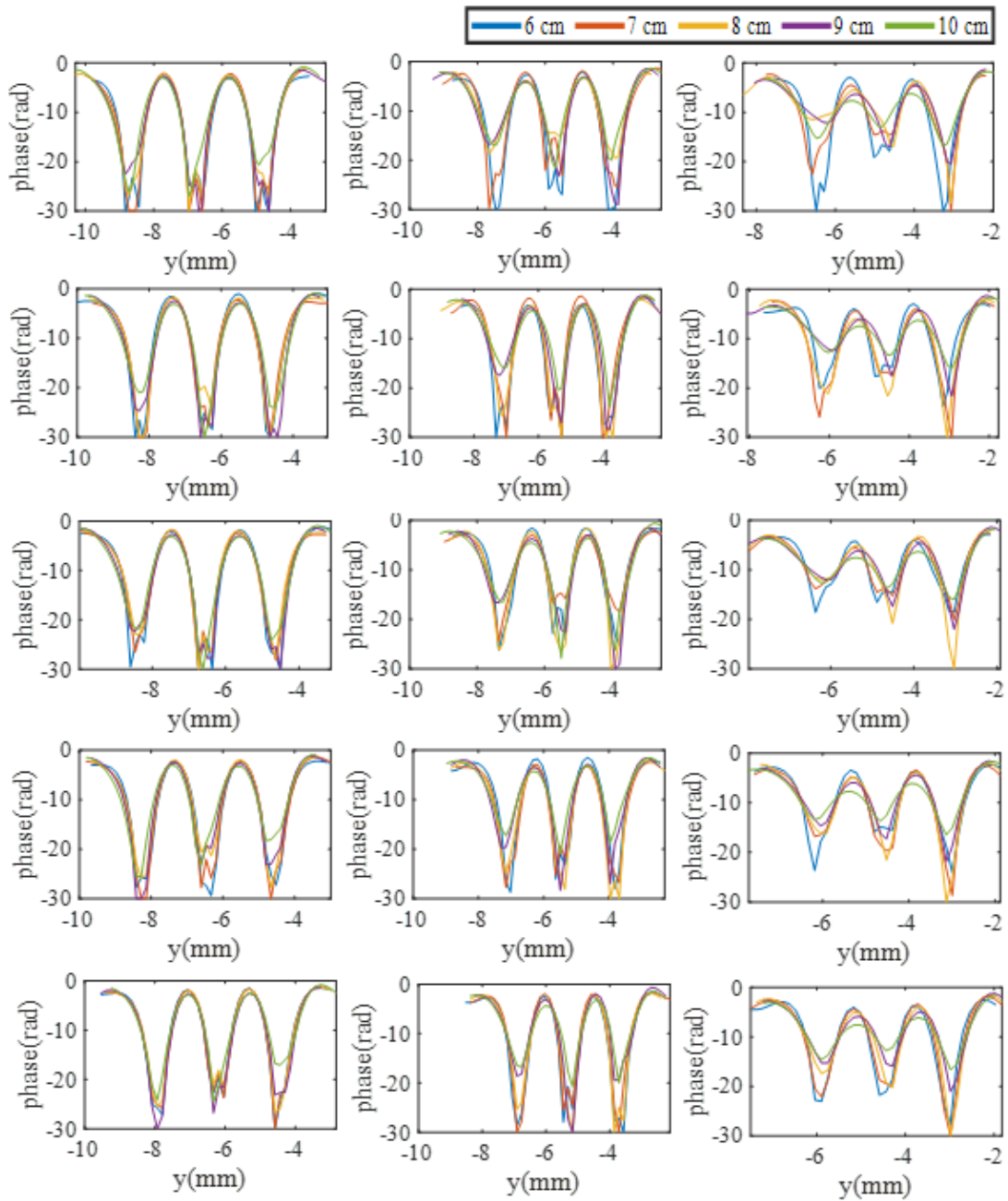


Figure B.4: One dimension data cutting through the stripes in vertical directions of Number 1 to 3 elements in Fig. B.2. Rows in declining order correspond to 6 cm to 10 cm focal length with 1-cm step, left to right column correspond to group number 1 to 3.

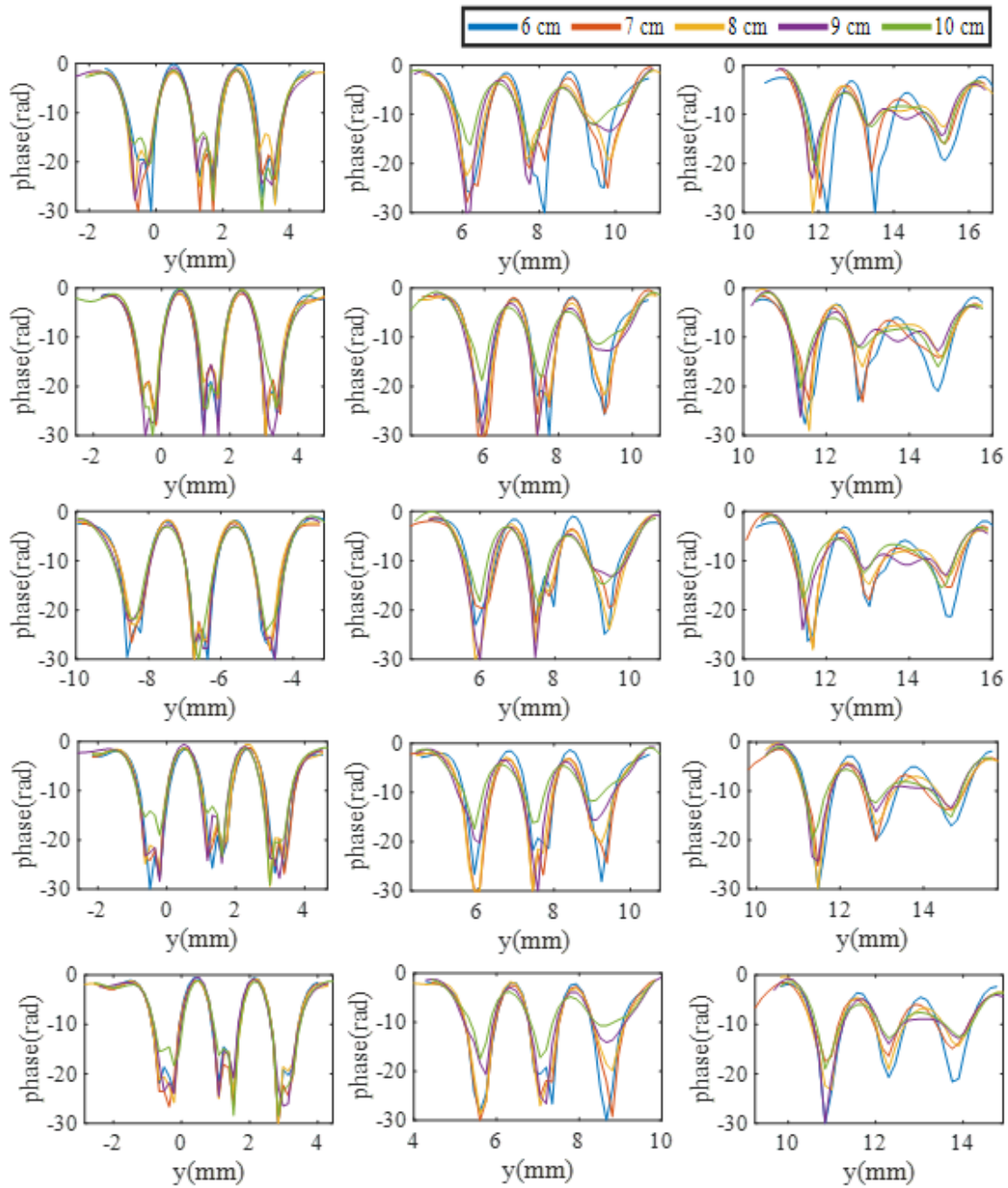


Figure B.5: One dimension data cutting through the stripes in lateral directions of Number 1 to 3 elements in Fig. B.2. Rows from top to bottom correspond to 6 cm to 10 cm focal length with 1-cm interval, left to right column correspond to group number 1 to 3.

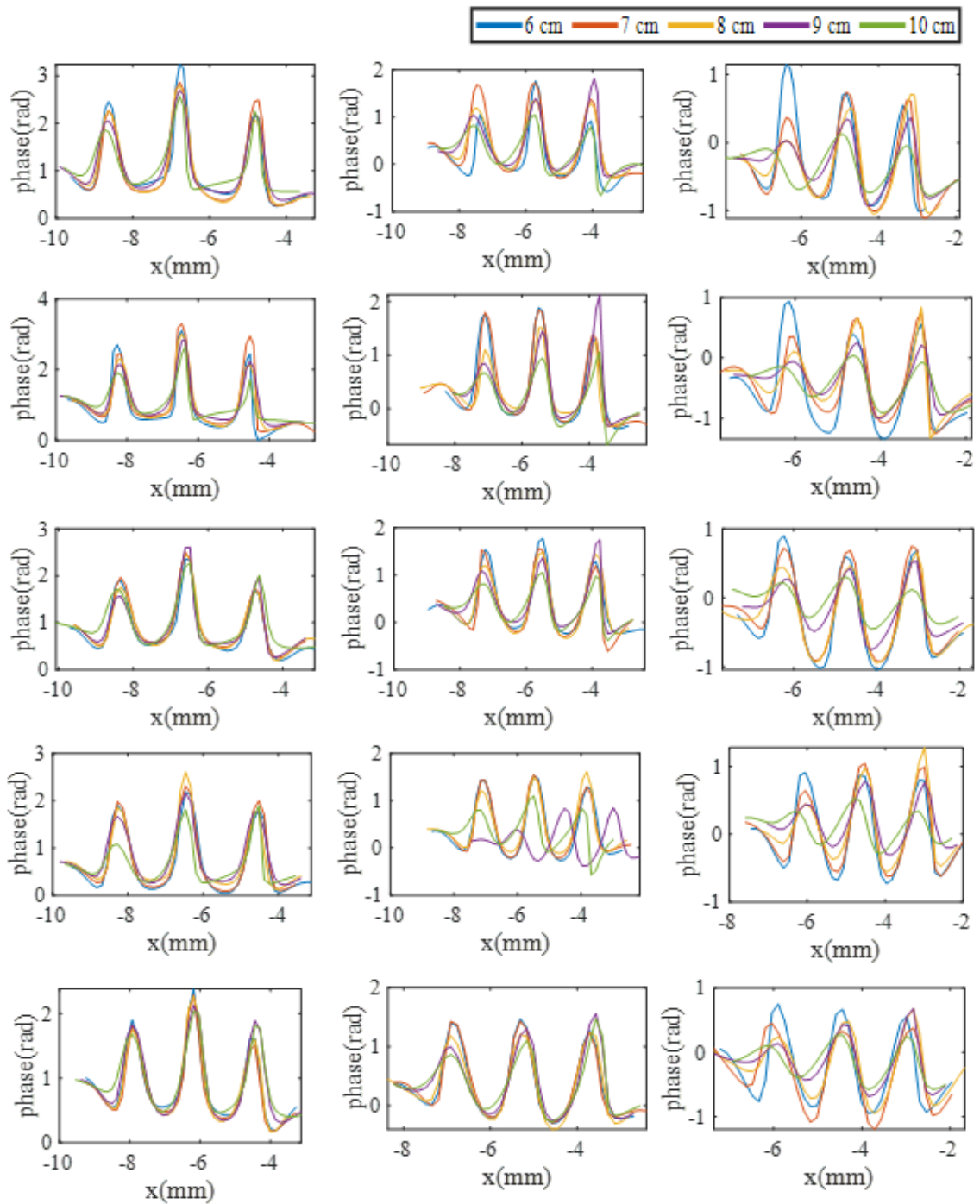


Figure B.6: One dimension data cutting through the stripes in vertical directions of Number 1 to 3 elements in Fig. B.3. The spectrum for the focal length from 6 cm to 10 cm is displayed in the descending order.

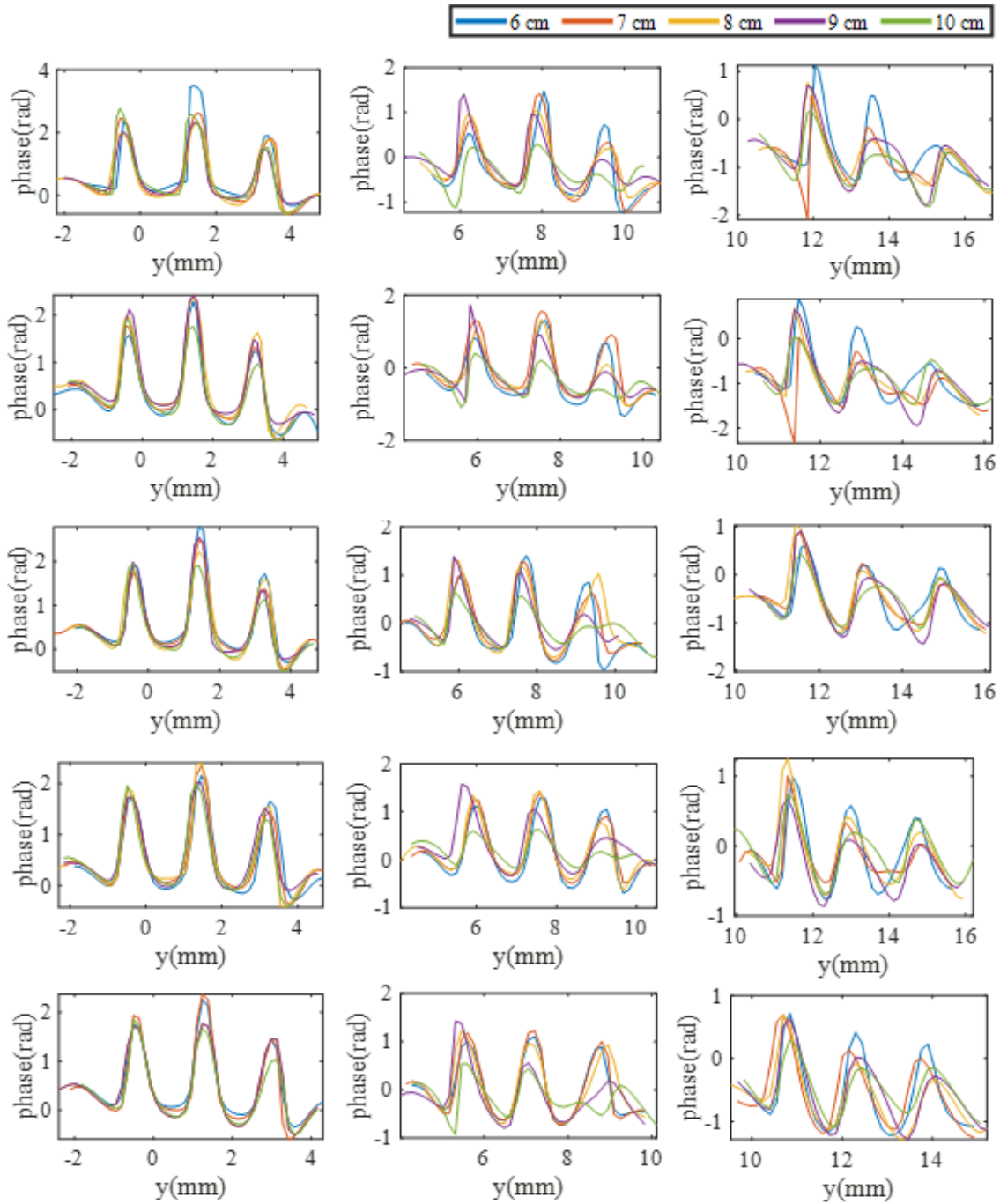


Figure B.7: One dimension data cutting through the stripes in lateral directions of Number 1 to 3 elements in Fig. B.3. The spectrum for the focal length from 6 cm to 10 cm is displayed in the descending order.

that in intensity images.

## B.2 Depth resolution simulation

The USAF chart is also adopted as the imaging target to validate the depth resolution simulation. Here the sharpness of imaging results of specific object distance with different focal lengths under focus and defocus reconstruction distances is used to define the focusing effect and further present the depth resolution capability. The reconstructed images are clarified in Fig. B.8. The sharpness calculation is derived based on the shape from the focus method. For the 6-cm object distance, the sharpness of imaging results using the focal length from 6 cm to 10 cm with 1-cm interval under the reconstructed distance from 2 cm to 10 cm are shown as Fig. B.9. With the FWHM (Full Width - Half Maximum) of the main peak, the depth resolution can be roughly deduced as the definition for lateral resolution.

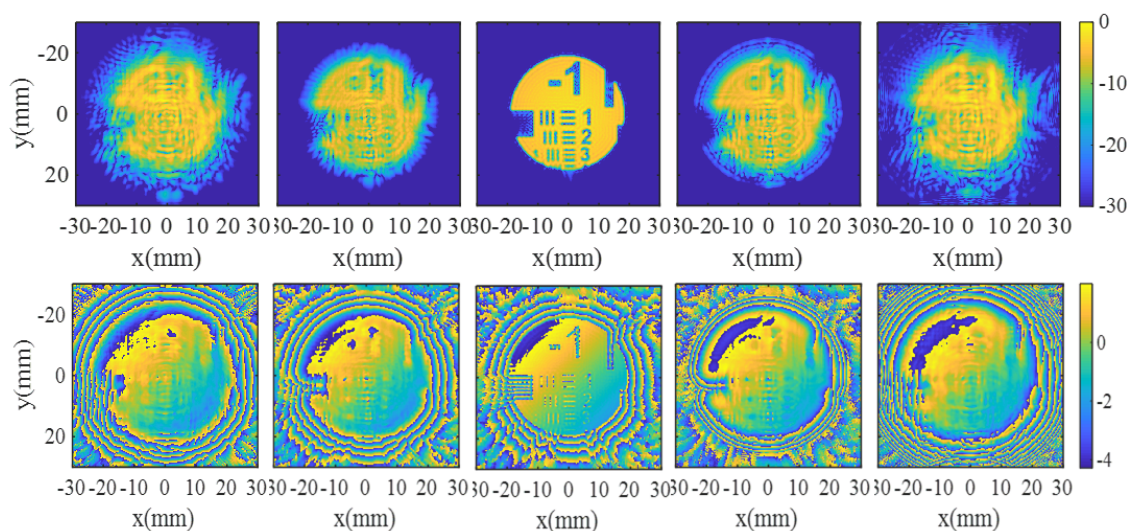


Figure B.8: The reconstructed images of USAF chart by using object distance from 2 cm to 10 cm with an interval of 2 cm, the top and bottom rows are intensity and phase, respectively.

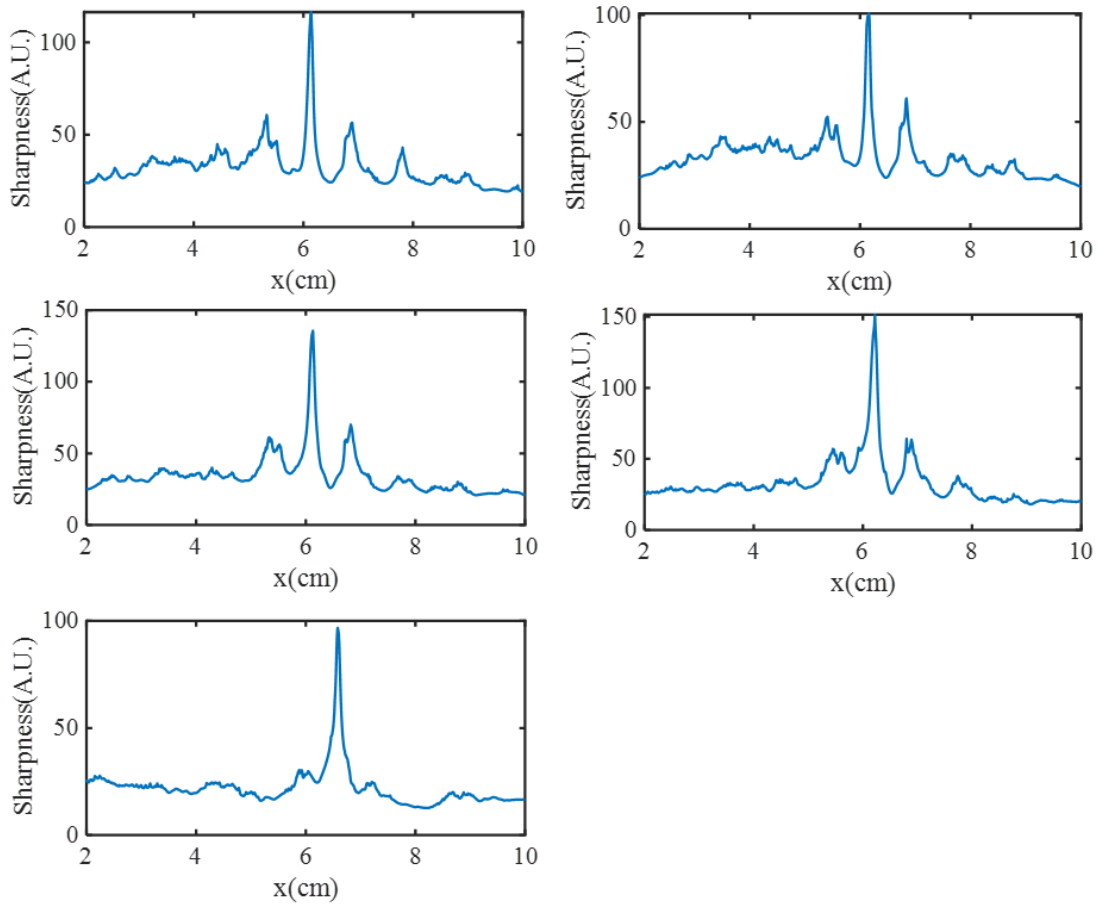


Figure B.9: The sharpness change of the reconstructed images along with the object distance variation. The sub-figures from left to right and up to down correspond to the focal length from 6 cm to 10 cm successively.



# Bibliography

- [1] H. Zhong, A. Redo, Y. Chen, and X. -. Zhang, “Standoff distance detection of explosive materials with THz waves,” in *2005 Joint 30th International Conference on Infrared and Millimeter Waves and 13th International Conference on Terahertz Electronics*, vol. 1, 2005, 42–43 vol. 1. DOI: 10.1109/ICIMW.2005.1572397.
- [2] Z. D. Taylor, R. S. Singh, D. B. Bennett, P. Tewari, C. P. Kealey, N. Bajwa, M. O. Culjat, A. Stojadinovic, H. Lee, J. Hubschman, E. R. Brown, and W. S. Grundfest, “THz Medical Imaging: in vivo Hydration Sensing,” *IEEE Transactions on Terahertz Science and Technology*, vol. 1, no. 1, pp. 201–219, 2011. DOI: 10.1109/TTHZ.2011.2159551.
- [3] B. Hils, M. Thomson, T. Löffler, W. Spiegel, C. Weg, H. Roskos, P. Maagt, D. Doyle, and R. Geckeler, “Terahertz profilometry at 600 GHz with 0.5  $\mu\text{m}$  depth resolution,” *Optics express*, vol. 16, pp. 11 289–93, Jul. 2008. DOI: 10.1364/OE.16.011289.
- [4] H.-B. Liu, G. Plopper, S. Earley, Y. Chen, B. Ferguson, and X.-C. Zhang, “Sensing minute changes in biological cell monolayers with THz differential time-domain spectroscopy,” *Biosensors and Bioelectronics*, vol. 22, no. 6, pp. 1075–1080, 2007. DOI: 10.1016/j.bios.2006.02.021.
- [5] K. Siebert, T. Löffler, H. Quast, M. Thomson, T. Bauer, R. Leonhardt, S. Czasch, and H. Roskos, “All-optoelectronic continuous wave THz imaging for biomedical applications,” *Physics in medicine and biology*, vol. 47, pp. 3743–8, Dec. 2002. DOI: 10.1088/0031-9155/47/21/310.

- [6] T. Idehara, T. Saito, I. Ogawa, S. Mitsudo, and Y. Tatematsu, “High power THz technologies using high frequency gyrotrons,” in *2012 37th International Conference on Infrared, Millimeter, and Terahertz Waves*, 2012, pp. 1–2. DOI: 10.1109/IRMMW-THz.2012.6380408.
- [7] P. Tan, J. Huang, K. Liu, Y. Xiong, and M. Fan, “Terahertz radiation sources based on free electron lasers and their applications,” *Science China Information Sciences*, vol. 55, no. 1, pp. 1–15, 2012. DOI: 10.1007/s11432-011-4515-1.
- [8] X. Xu, Y. Wei, F. Shen, H. Yin, J. Xu, Y. Gong, and W. Wang, “A watt-class 1-THz backward-wave oscillator based on sine waveguide,” *Physics of Plasmas*, vol. 19, no. 1, p. 013 113, 2012. DOI: 10.1063/1.3677889.
- [9] M. Asada, S. Suzuki, and N. Kishimoto, “Resonant Tunneling Diodes for Sub-Terahertz and Terahertz Oscillators,” *Japanese Journal of Applied Physics*, vol. 47, p. 4375, May 2008. DOI: 10.1143/JJAP.47.4375.
- [10] M. Feiginov, “THz resonant-tunnelling diodes,” Apr. 2020, p. 20. DOI: 10.1117/12.2559674.
- [11] W. R. Huang, A. Fallahi, X. Wu, H. Cankaya, A.-L. Calendron, K. Ravi, D. Zhang, E. A. Nanni, K.-H. Hong, and F. X. Kärtner, “Terahertz-driven, all-optical electron gun,” *Optica*, vol. 3, no. 11, pp. 1209–1212, Nov. 2016. DOI: 10.1364/OPTICA.3.001209. [Online]. Available: <http://www.osapublishing.org/optica/abstract.cfm?URI=optica-3-11-1209>.
- [12] C. F. Dalle, “Differentiated Doping Profile for Vertical Terahertz GaN Transferred-Electron Devices,” *IEEE Transactions on Electron Devices*, vol. 62, no. 3, pp. 802–807, 2015. DOI: 10.1109/TED.2015.2392158.
- [13] H. Eisele and R. Kamoua, “Submillimeter-wave InP Gunn devices,” *IEEE Transactions on Microwave Theory and Techniques*, vol. 52, no. 10, pp. 2371–2378, 2004. DOI: 10.1109/TMTT.2004.835974.

- 
- [14] L. Wandinger, “mm-wave InP Gunn devices - Status and trends,” *Microwave Journal*, vol. 24, p. 71, Mar. 1981.
- [15] L. -. Schmidt, S. Biber, G. Rehm, and K. Huber, “THz measurement technologies and applications,” in *14th International Conference on Microwaves, Radar and Wireless Communications. MIKON - 2002. Conference Proceedings (IEEE Cat.No.02EX562)*, vol. 2, 2002, 581–587 vol.2. DOI: 10.1109/MIKON.2002.1017914.
- [16] L. A. Samoska, T. C. Gaier, A. Peralta, S. Weinreb, J. Bruston, I. Mehdi, Y. Chen, H. H. Liao, M. Nishimoto, R. Lai, H. Wang, and Y. C. Leong, “MMIC power amplifiers as local oscillator drivers for FIRST,” in *UV, Optical, and IR Space Telescopes and Instruments*, J. B. Breckinridge and P. Jakobsen, Eds., International Society for Optics and Photonics, vol. 4013, SPIE, 2000, pp. 275–284. DOI: 10.1117/12.393983.
- [17] H. Eisele, “355 GHz oscillator with GaAs TUNNETT diode,” *Electronics Letters*, vol. 41, pp. 329–331, Apr. 2005. DOI: 10.1049/el:20058165.
- [18] M. Tonouchi, “Cutting-edge terahertz technology,” *Nature Photonics*, vol. 1, 97 EP, Feb. 2007. DOI: 10.1038/nphoton.2007.3.
- [19] R. R. A. Pavel Shumyatsky, “Terahertz sources,” *Journal of Biomedical Optics*, vol. 16, pp. 16–10, 2011. DOI: 10.1117/1.3554742.
- [20] S. S. Dhillon, M. S. Vitiello, E. H. Linfield, A. G. Davies, M. C. Hoffmann, and et al., “The 2017 terahertz science and technology roadmap,” *Journal of Physics D: Applied Physics*, vol. 50, no. 4, p. 043 001, 2017.
- [21] H.-B. Liu, G. Plopper, S. Earley, Y. Chen, B. Ferguson, and X.-C. Zhang, “Sensing minute changes in biological cell monolayers with THz differential time-domain spectroscopy,” *Biosensors & bioelectronics*, vol. 22, pp. 1075–80, Feb. 2007. DOI: 10.1016/j.bios.2006.02.021.

- [22] Z. Jiang and X.-C. Zhang, “2D measurement and spatio-temporal coupling of few-cycle THz pulses,” *Opt. Express*, vol. 5, no. 11, pp. 243–248, Nov. 1999. DOI: 10.1364/OE.5.000243.
- [23] N. Sunaguchi and T. Yuasa, “Imaging with terahertz waves,” *Optics Express*, vol. 17, pp. 9558–9570, May 2009.
- [24] I.-M. Lee, N. Kim, E. Lee, S.-P. Han, K. Moon, and k. H. Park, “Frequency modulation based continuous-wave terahertz homodyne system,” *Optics Express*, vol. 23, p. 846, Jan. 2015. DOI: 10.1364/OE.23.000846.
- [25] K. Kim, H.-J. Song, K. Ajito, M. Yaita, and N. Kukutsu, “Continuous-Wave THz Homodyne Spectroscopy and Imaging System With Electro-Optical Phase Modulation for High Dynamic Range,” *IEEE Transactions on Terahertz Science and Technology*, vol. 3, pp. 158–164, Mar. 2013. DOI: 10.1109/TTHZ.2012.2228896.
- [26] T. Loeffler, T. May, A. Alcin, B. Hils, C. Weg, and H. Roskos, “Continuous-wave terahertz imaging with a hybrid system,” *Applied Physics Letters - APPL PHYS LETT*, vol. 90, Feb. 2007. DOI: 10.1063/1.2711183.
- [27] Y. Wang, Z. Zhao, Z. Chen, l. Zhang, K. Kang, and J. Deng, “Continuous-wave terahertz phase imaging using a far-infrared laser interferometer,” *Applied optics*, vol. 50, pp. 6452–60, Dec. 2011. DOI: 10.1364/AO.50.006452.
- [28] M. Bessou, B. Chassagne, J.-P. Caumes, C. Pradere, P. Maire, M. Tondusson, and E. Abraham, “Three-dimensional terahertz computed tomography of human bones,” *Applied optics*, vol. 51, pp. 6738–44, Oct. 2012. DOI: 10.1364/AO.51.006738.
- [29] B. Ferguson, S. Wang, D. Gray, D. Abbott, and X.-C. Zhang, “T-ray computed tomography,” *Optics Letters*, vol. 27, pp. 1312–1314, Aug. 2002. DOI: 10.1364/OL.27.001312.

- 
- [30] N. Rothbart, H. Richter, M. Wienold, L. Schrottke, H. T. Grahn, and H. Hübers, “Fast 2-D and 3-D Terahertz Imaging With a Quantum-Cascade Laser and a Scanning Mirror,” *IEEE Transactions on Terahertz Science and Technology*, vol. 3, no. 5, pp. 617–624, 2013. DOI: 10.1109/TTHZ.2013.2273226.
- [31] E. Abraham, A. Younus, C. Aguerre, P. Desbarats, and P. Mounaix, “Refraction losses in terahertz computed tomography,” *Optics Communications*, vol. 283, pp. 2050–2055, May 2010. DOI: 10.1016/j.optcom.2010.01.013.
- [32] B. Recur, A. Younus, S. Salort, P. Mounaix, B. Chassagne, P. Desbarats, J.-P. Caumes, and E. Abraham, “Investigation on reconstruction methods applied to 3D terahertz computed tomography,” *Optics express*, vol. 19, pp. 5105–17, Mar. 2011. DOI: 10.1364/OE.19.005105.
- [33] J. Goodman, *Introduction to Fourier Optics*, 4th ed. W. H. Freeman, 2017.
- [34] H. Guerboukha, K. Nallappan, and M. Skorobogatiy, “Exploiting k-space/frequency duality toward real-time terahertz imaging,” *Optica*, vol. 5, pp. 109–116, Jan. 2018.
- [35] Z. Zhang, X. Ma, and J. Zhong, “Single-pixel imaging by means of Fourier spectrum acquisition,” *Nature communications*, vol. 6, p. 6225, Feb. 2015. DOI: 10.1038/ncomms7225.
- [36] K. Goda, G. Popescu, K. K. Tsia, and D. Psaltis, “Computational optical imaging goes viral,” *APL Photonics*, vol. 5, no. 3, p. 030401, 2020. DOI: 10.1063/5.0004471.
- [37] Nov. 2020. [Online]. Available: <https://en.wikipedia.org/wiki/Diffraction>.
- [38] C. Huygens, *Treatise On Light*. Macmillan and Company., Limited, 1912.
- [39] Nov. 2020. [Online]. Available: <https://en.wikipedia.org/wiki/Huygens>.
- [40] E. W. Max Born, *Principles of Optics: Electromagnetic Theory of Propagation, Interference and Diffraction of Light*. Cambridge University Press., 1999, p. 986, ISBN: 9780521642224.

- [41] —, *Principles of Optics*, 60th Anniversary. Cambridge University Press, Jan. 2020, ISBN: 978-1-108-47743-7.
- [42] Nov. 2020. [Online]. Available: [https://en.wikipedia.org/wiki/Fresnel\\_diffraction](https://en.wikipedia.org/wiki/Fresnel_diffraction).
- [43] —, *Principles of Optics: Electromagnetic Theory of Propagation, Interference and Diffraction of Light*. Cambridge University Press., 1999, p. 142, ISBN: 9780521642224.
- [44] W. Sun, X. Wang, and Y. Zhang, “Continuous wave terahertz phase imaging with three-step phase-shifting,” *Optik*, vol. 124, pp. 5533–5536, Nov. 2013. DOI: 10.1016/j.ijleo.2013.03.150.
- [45] Y. Wang, Z. Zhao, Z. Chen, I. Zhang, K. Kang, and J. Deng, “Continuous-wave terahertz phase imaging using a far-infrared laser interferometer,” *Applied optics*, vol. 50, pp. 6452–60, Dec. 2011. DOI: 10.1364/AO.50.006452.
- [46] A. Enayati, A. Tamminen, J. Ala-Laurinaho, A. Raisanen, G. Vandenbosch, and W. De Raedt, “THz holographic imaging: A spatial-domain technique for phase retrieval and image reconstruction,” Jun. 2012, pp. 1–3, ISBN: 978-1-4673-1085-7. DOI: 10.1109/MWSYM.2012.6258284.
- [47] H. Yuan, D. Voß, A. Lisauskas, D. Mundy, and H. G. Roskos, “3D Fourier imaging based on 2D heterodyne detection at THz frequencies,” *APL Photonics*, vol. 4, no. 10, p. 106 108, 2019. DOI: 10.1063/1.5116553.
- [48] M. Wan, H. Yuan, D. Čibiraitė, D. Cassidy, A. Lisauskas, J. J. Healy, H. G. Roskos, V. Krozer, and J. T. Sheridan, “Terahertz quantitative metrology using 300 GHz in-line digital holography,” in *Holography: Advances and Modern Trends VI*, A. Fimia, M. Hrabovský, and J. T. Sheridan, Eds., International Society for Optics and Photonics, vol. 11030, SPIE, 2019, pp. 155–161. DOI: 10.1117/12.2520787.

- [49] L. Rong, T. Latychevskaia, C. Chen, D. Wang, Z. Yu, X. Zhou, L. Zeyu, H. Huang, Y. Wang, and Z. Zhou, “Terahertz in-line digital holography of human hepatocellular carcinoma tissue,” *Scientific Reports*, vol. 5, p. 8445, Feb. 2015. DOI: 10.1038/srep08445.
- [50] L. Valzania, P. Zolliker, and E. Hack, “Topography of hidden objects using THz digital holography with multi-beam interferences,” *Optics Express*, vol. 25, p. 11 038, May 2017. DOI: 10.1364/OE.25.011038.
- [51] M. Locatelli, M. Ravaro, S. Bartalini, L. Consolino, M. Vitiello, R. Cicchi, F. Pavone, and P. Natale, “Real-time terahertz digital holography with a quantum cascade laser,” *Scientific Reports*, vol. 5, p. 13 566, Aug. 2015. DOI: 10.1038/srep13566.
- [52] P. Zolliker and E. Hack, “THz holography in reflection using a high resolution microbolometer array,” *Opt. Express*, vol. 23, no. 9, pp. 10 957–10 967, May 2015. DOI: 10.1364/OE.23.010957.
- [53] K. Xue, Q. Li, Y.-D. Li, and Q. Wang, “Continuous-wave terahertz in-line digital holography,” *Optics letters*, vol. 37, pp. 3228–30, Aug. 2012. DOI: 10.1364/OL.37.003228.
- [54] R. K. Amineh, M. Ravan, A. Khalatpour, and N. K. Nikolova, “Three-Dimensional Near-Field Microwave Holography Using Reflected and Transmitted Signals,” *IEEE Transactions on Antennas and Propagation*, vol. 59, no. 12, pp. 4777–4789, 2011. DOI: 10.1109/TAP.2011.2165496.
- [55] K. Wu, Q. Cheng, Y. Shi, H. Wang, and G. P. Wang, “Hiding scattering layers for noninvasive imaging of hidden objects,” *Scientific Reports*, vol. 5, no. 1, pp. 2045–2322, 2015. DOI: 10.1038/srep08375.
- [56] M. Wenwen, D. Shi, H. Jian, Y. Kee, Y. Wang, and F. Chengyu, “Sparse Fourier single-pixel imaging,” *Optics Express*, vol. 27, p. 31 490, Oct. 2019. DOI: 10.1364/OE.27.031490.

- [57] E. J. Candes and M. B. Wakin, “An Introduction To Compressive Sampling,” *IEEE Signal Processing Magazine*, vol. 25, no. 2, pp. 21–30, 2008. DOI: 10.1109/MSP.2007.914731.
- [58] Nov. 2020. [Online]. Available: [https://en.wikipedia.org/wiki/Sparse\\_Fourier\\_transform](https://en.wikipedia.org/wiki/Sparse_Fourier_transform).
- [59] L. Shi, H. Hassanieh, A. Davis, D. Katabi, and F. Durand, “Light Field Reconstruction Using Sparsity in the Continuous Fourier Domain,” *ACM Transactions on Graphics*, vol. 34, pp. 1–13, Dec. 2014. DOI: 10.1145/2682631.
- [60] X. Zhang, H. Kang, Y. Zuo, Z. Lou, Y. Wang, and Y. Qian, “Near-Field Radio Holography of Slant-Axis Terahertz Antennas,” *IEEE Transactions on Terahertz Science and Technology*, vol. 10, Dec. 2019. DOI: 10.1109/TTHZ.2019.2958066.
- [61] G. Junkin, “Phase shifting holography for THz near-field/far-field prediction,” *Progress In Electromagnetics Research*, vol. 44, pp. 15–21, Jan. 2014. DOI: 10.2528/PIERL13093006.
- [62] Z. Ou, J. Wu, H. Geng, X. Deng, and X. Zheng, “Confocal terahertz SAR imaging of hidden objects through rough-surface scattering,” *Opt. Express*, vol. 28, no. 8, pp. 12 405–12 415, Apr. 2020. DOI: 10.1364/OE.388392.
- [63] G. Tricoles and N. H. Farhat, “Microwave Holography: Applications and Techniques,” *Proc. IEEE*, vol. 65, no. 1, pp. 108–121, 1977. DOI: 10.1109/PROC.1977.10435.
- [64] G. C. Trichopoulos, H. L. Mosbacker, D. Burdette, and K. Sertel, “A Broad-band Focal Plane Array Camera for Real-time THz Imaging Applications,” *IEEE Transactions on Antennas and Propagation*, vol. 61, no. 4, pp. 1733–1740, Apr. 2013. DOI: 10.1109/TAP.2013.2242829.
- [65] N. Oda, “Uncooled bolometer-type terahertz focal plane array and camera for real-time imaging,” *C. R. Physique*, vol. 5, pp. 496–509, 2010.

- 
- [66] R. Al Hadi, H. Sherry, J. Grzyb, Y. Zhao, W. Förster, H. M. Keller, A. Cathelin, A. Kaiser, and U. R. Pfeiffer, “A 1 k-pixel video camera for 0.7–1.1 terahertz imaging applications in 65-nm CMOS,” *IEEE J. Solid-State Circuits*, vol. 47, pp. 2999–3012, 2012.
- [67] V. Muravev, G. Tsydynzhapov, A. Fortunatov, and I. Kukushkin, “High-speed THz semiconductor imaging camera,” *Proc. of the 38th Intern. Conf. on Infrared, Millimeter, and Terahertz Waves (IRMMW-THz)*, vol. 61, pp. 1733–1740, 2013.
- [68] F. Simoens, J. Meilhan, and J. A. Nicolas, “Terahertz real-time imaging uncooled arrays based on antenna-coupled bolometers or FET developed at CEA-Leti,” *J. Infrared Millim. Terahertz Waves*, vol. 36, pp. 961–985, 2015.
- [69] J. Zdanevičius, M. Bauer, S. Boppel, V. Palenskis, A. Lisauskas, V. Krozer, and H. G. Roskos, “Camera for high-speed THz imaging,” *J. Infrared Millim. Terahertz Waves*, vol. 36, pp. 986–997, 2015.
- [70] H. Yuan, M. Wan, A. Lisauskas, J. T. Sheridan, and H. G. Roskos, “300-GHz in-line holography with high dynamic range,” in *Holography: Advances and Modern Trends VI*, A. Fimia, M. Hrabovský, and J. T. Sheridan, Eds., International Society for Optics and Photonics, vol. 11030, SPIE, 2019, pp. 162–168. DOI: 10.1117/12.2520954.
- [71] Nov. 2020. [Online]. Available: [https://military.wikia.org/wiki/1951\\_USAF\\_resolution\\_test\\_chart](https://military.wikia.org/wiki/1951_USAF_resolution_test_chart).
- [72] C. Cooper, *Physics*. Chicago : Fitzroy Dearborn, 2001, p. 25, ISBN: 9781579583583.
- [73] R. F. Graf, *Modern Dictionary of Electronics*, 7th ed. USA: Newnes, 1999, p. 344, ISBN: 978-0-7506-9866-5.
- [74] U. S. B. of Naval Personnel, *Basic Electronics*. USA: Courier Dover, 1973, p. 338, ISBN: 978-0-486-21076-6.
- [75] P. Horowitz and W. Hill, *The Art of Electronics*, 2nd ed. London: Cambridge University Press., 1989, p. 885, ISBN: 978-0-521-37095-0.

- [76] P. Strange Allen; Strange, *The Contemporary Violin: Extended Performance Techniques*. Scarecrow Press, 2003, p. 216, ISBN: 978-0-520-22409-4.
- [77] D. Glaab, S. Boppel, A. Lisauskas, U. Pfeiffer, E. Öjefors, and H. G. Roskos, “Terahertz heterodyne detection with silicon field-effect transistors,” *Appl. Phys. Lett.*, vol. 96, p. 042106, 2010.
- [78] S. Boppel, A. Lisauskas, A. Max, V. Krozer, and H. G. Roskos, “CMOS detector arrays in a virtual 10-kilopixel camera for coherent terahertz real-time imaging,” *Opt. Lett.*, vol. 37, pp. 536–538, 2012.
- [79] A. Lisauskas, M. Bauer, S. Boppel, M. Mundt, B. Khamaisi, E. Socher, R. Venckevičius, L. Minkevicius, I. Kašalynas, D. Seliuta, G. Valušis, V. Krozer, and H. G. Roskos, “Exploration of Terahertz Imaging with Silicon MOSFETs,” *J. Infrared Millim. Terahertz Waves*, vol. 35, pp. 63–80, 2014.
- [80] J. Grzyb and U. Pfeiffer, “THz Direct Detector and Heterodyne Receiver Arrays in Silicon Nanoscale Technologies,” *J. Infrared Millim. Terahertz Waves*, vol. 36, pp. 998–1032, 2015.
- [81] H. Yuan, M. Wan, A. Lisauskas, J. T. Sheridan, and H. G. Roskos, “300-GHz holography with heterodyne detection,” in *Digital Holography and Three-Dimensional Imaging 2019*, Optical Society of America, 2019, Th3A.21. DOI: 10.1364/DH.2019.Th3A.21.
- [82] H. X. Deng, M. C. Gao X. C. and Ma, P. C. Yao, Q. T. Guan, and J. Zhong X. and Zhang, “Fourier single-pixel imaging using fewer illumination patterns,” *Appl. Phys. Lett.*, vol. 114, p. 221906, 2019.
- [83] Y. J. Shang, W. F. Wang X. K. and Sun, P. Han, J. S. Ye, S. F. Feng, and Y. Zhang, “Terahertz image reconstruction based on compressed sensing and inverse Fresnel diffraction,” *Opt. Express*, vol. 27, pp. 14725–14735, 2019.
- [84] X. Y. Hu, H. Zhang, Q. Zhao, P. P. Yu, Y. M. Li, and L. Gong, “Single-pixel phase imaging by Fourier spectrum sampling,” *Appl. Phys. Lett.*, vol. 114, p. 051102, 2019.

- 
- [85] A. Lisauskas, U. Pfeiffer, E. Öjefors, P. Haring Bolívar, D. Glaab, and H. G. Roskos, “Rational design of high-responsivity detectors of THz radiation based on distributed self-mixing in silicon CMOS transistors,” *J. Appl. Phys.*, vol. 105, p. 114511, 2009.
- [86] K. Ikamas, D. Čibiraitė, A. Lisauskas, M. Bauer, V. Krozer, and H. G. Roskos, “Broadband terahertz power detectors based on 90-nm silicon CMOS transistors with flat responsivity up to 2.2 THz,” *IEEE Electron Dev. Lett.*, vol. 39, pp. 1413–1416, 2018.
- [87] M. T. Reiten and R. A. Cheville, “Effect of spherical aberration and surface waves on propagation of lens-coupled terahertz pulses,” *Opt. Lett.*, vol. 30, pp. 673–675, 2005.
- [88] R. N. Han, C. Jiang, A. Mostajeran, M. Emadi, H. Aghasi, H. Sherry, A. Cathelin, and E. Afshari, “A 320 GHz phase-locked transmitter with 3.3 mW radiated power and 22.5 dBm EIRP for heterodyne THz imaging systems,” in *2015 IEEE International Solid-State Circuits Conference - (ISSCC) Digest of Technical Papers*, San Francisco, CA, USA: IEEE, Feb. 2015, pp. 15–17. (visited on 05/07/2019).
- [89] M. R. A. Bacha, A. Oukebdane, and A. H. Belbachir, “Implementation of the zero-padding interpolation technique to improve angular resolution of X-ray tomographic acquisition system,” *Pattern Recogn. Image Anal.*, vol. 26, pp. 817–823, 2016.
- [90] A. Lisauskas, S. Boppel, M. Mundt, V. Krozer, and H. G. Roskos, “Subharmonic Mixing With Field-Effect Transistors: Theory and Experiment at 639 GHz High Above  $f_T$ ,” *IEEE Sensors Journal*, vol. 13, no. 1, pp. 124–132, 2013. DOI: 10.1109/JSEN.2012.2223668.
- [91] C. Jiang, A. Mostajeran, R. Han, M. Emadi, H. Sherry, A. Cathelin, and E. Afshari, “A Fully Integrated 320 GHz Coherent Imaging Transceiver in 130 nm SiGe BiCMOS,” *IEEE Journal of Solid-State Circuits*, vol. 51, no. 11, pp. 2596–2609, 2016. DOI: 10.1109/JSSC.2016.2599533.

- [92] K. Ikamas, I. Nevinskas, A. Krotkus, and A. Lisauskas, “Silicon Field Effect Transistor as the Nonlinear Detector for Terahertz Autocorellators,” *Sensors*, vol. 18, no. 11, 2018, ISSN: 1424-8220. DOI: 10.3390/s18113735. [Online]. Available: <https://www.mdpi.com/1424-8220/18/11/3735>.
- [93] M. Naftaly, R. E. Miles, and P. J. Greenslade, “THz transmission in polymer materials — a data library,” in *2007 Joint 32nd International Conference on Infrared and Millimeter Waves and the 15th International Conference on Terahertz Electronics*, 2007, pp. 819–820. DOI: 10.1109/ICIMW.2007.4516747.
- [94] M. Asada, “Theoretical analysis of subharmonic injection locking in resonant-tunneling-diode terahertz oscillators,” *Japanese Journal of Applied Physics*, vol. 59, no. 1, p. 018001, Dec. 2019. DOI: 10.7567/1347-4065/ab600b. [Online]. Available: <https://doi.org/10.7567%2F1347-4065%2Fab600b>.
- [95] K. J. Button, *Infrared and Millimeter Waves*. Academic Press, INC, 1983. [Online]. Available: <https://books.google.de/books?hl=en&lr=&id=delnT8ewgT4C&oi=fnd&pg=PA1&dq=integrated+circuit+antennas&ots=4rkEya4-pS&sig=7LaDqfshNEFovf7Nd32nfdyra5U#v=onepage&q=integrated%20circuit%20antennas&f=false>.
- [96] A. Neice, “Chapter 3 - Methods and Limitations of Subwavelength Imaging,” in, ser. *Advances in Imaging and Electron Physics*, P. W. Hawkes, Ed., vol. 163, Elsevier, 2010, pp. 117–140. DOI: [https://doi.org/10.1016/S1076-5670\(10\)63003-0](https://doi.org/10.1016/S1076-5670(10)63003-0). [Online]. Available: <https://www.sciencedirect.com/science/article/pii/S1076567010630030>.
- [97] J.-B. Perraud, J.-P. Guillet, M. Hamdi, O. Redon, J. Meilhan, F. Simoens, and P. Mounaix, “Shape from Focus Applied to Real-Time Terahertz Imaging,” Sep. 2018, pp. 1–2. DOI: 10.1109/IRMMW-THz.2018.8510100.
- [98] D. Wang, B. Li, L. Rong, F. Tan, J. J. Healy, J. Zhao, and Y. Wang, “Multi-layered full-field phase imaging using continuous-wave terahertz ptychography,” *Opt. Lett.*, vol. 45, no. 6, pp. 1391–1394, Mar. 2020. DOI: 10.1364/OL.

384589. [Online]. Available: <http://ol.osa.org/abstract.cfm?URI=ol-45-6-1391>.
- [99] H. Zhong, A. Redo, Y. Chen, and X. -. Zhang, "Standoff distance detection of explosive materials with THz waves," in *2005 Joint 30th International Conference on Infrared and Millimeter Waves and 13th International Conference on Terahertz Electronics*, vol. 1, Sep. 2005, 42–43 vol. 1. DOI: 10.1109/ICIMW.2005.1572397.
- [100] Z. D. Taylor, R. S. Singh, D. B. Bennett, P. Tewari, C. P. Kealey, N. Bajwa, M. O. Culjat, A. Stojadinovic, H. Lee, J. Hubschman, E. R. Brown, and W. S. Grundfest, "THz Medical Imaging: in vivo Hydration Sensing," *IEEE Transactions on Terahertz Science and Technology*, vol. 1, no. 1, pp. 201–219, Sep. 2011. DOI: 10.1109/TTHZ.2011.2159551.
- [101] H. Song and T. Nagatsuma, "Present and Future of Terahertz Communications," *IEEE Transactions on Terahertz Science and Technology*, vol. 1, no. 1, pp. 256–263, Sep. 2011. DOI: 10.1109/TTHZ.2011.2159552.
- [102] K. Tanaka, H. Hirori, and M. Nagai, "THz Nonlinear Spectroscopy of Solids," *IEEE Transactions on Terahertz Science and Technology*, vol. 1, no. 1, pp. 301–312, Sep. 2011. DOI: 10.1109/TTHZ.2011.2159535.
- [103] H.-B. Liu, G. Plopper, S. Earley, Y. Chen, B. Ferguson, and X.-C. Zhang, "Sensing minute changes in biological cell monolayers with THz differential time-domain spectroscopy," *Biosensors and Bioelectronics*, vol. 22, no. 6, pp. 1075–1080, 2007. DOI: 10.1016/j.bios.2006.02.021.
- [104] K. J. Siebert, T. Löffler, H. Quast, M. Thomson, T. Bauer, R. Leonhardt, S. Czasch, and H. G. Roskos, "All-optoelectronic continuous wave THz imaging for biomedical applications," *Phys. Med. Biol.*, vol. 47, pp. 3743–3748, 2002.
- [105] D. Saeedkia, *Handbook of terahertz technology for imaging, sensing and communications*. Elsevier, Jan. 2013, ISBN: 9780857092359.

- [106] H. Guerboukha, K. Nallappan, and M. Skorobogatiy, “Exploiting k-space/frequency duality toward real-time terahertz imaging,” *Optica*, vol. 5, no. 2, pp. 109–116, Feb. 2018. DOI: 10.1364/OPTICA.5.000109.